

**THE STRUCTURAL, FERROELECTRIC, DIELECTRIC, AND
ELECTROMECHANICAL PROPERTIES OF PIEZOELECTRIC
AND ELECTROSTRICTIVE MATERIALS**

**LES PROPRIÉTÉS STRUCTURELLES, FERROÉLECTRIQUES,
DIÉLECTRIQUES ET ÉLECTROMÉCANIQUES DES
MATÉRIAUX PIÉZOÉLECTRITIQUES ET ÉLECTROSTRICTIFS**

A Thesis Submitted

to the Division of Graduate Studies of the Royal Military College of Canada

by

Maxime Bernier-Brideau, B.Sc., rmc

In Partial Fulfillment of the Requirements for the Degree of

Master of Science

April 2014

© This thesis may be used within the Department of National Defence
but copyright for open publication remains the property of the author.

**ROYAL MILITARY COLLEGE OF CANADA
COLLÈGE MILITAIRE ROYAL DU CANADA**

DIVISION OF GRADUATE STUDIES AND RESEARCH
DIVISION DES ÉTUDES SUPÉRIEURES ET DE LA RECHERCHE

This is to certify that the thesis prepared by / Ceci certifie que la thèse rédigée par

MAXIME BERNIER-BRIDEAU

entitled / intitulée

**THE STRUCTURAL, FERROELECTRIC, DIELECTRIC, AND
ELECTROMECHANICAL PROPERTIES OF PIEZOELECTRIC AND
ELECTROSTRICTIVE MATERIALS**

complies with the Royal Military College of Canada regulations and that it meets the accepted standards of the Graduate School with respect to quality, and, in the case of a doctoral thesis, originality, / satisfait aux règlements du Collège militaire royal du Canada et qu'elle respecte les normes acceptées par la Faculté des études supérieures quant à la qualité et, dans le cas d'une thèse de doctorat, l'originalité,

for the degree of / pour le diplôme de

MASTER OF SCIENCE

Signed by the final examining committee: /

Signé par les membres du comité examinateur de la soutenance de thèse

_____, Chair / Président

_____, External Examiner / Examineur externe

_____, Main Supervisor / Directeur de thèse principal

Approved by the Head of Department : /

Approuvé par le Directeur du Département : _____ Date: _____

To the Librarian: This thesis is not to be regarded as classified. /
Au Bibliothécaire : Cette thèse n'est pas considérée comme à publication restreinte.

Main Supervisor / Directeur de thèse principal

ACKNOWLEDGEMENTS

First and foremost, I would like to thank my thesis supervisor, Dr. Ribal Georges Sabat, for his guidance, support, and extreme patience throughout the completion of this thesis. I started working on this thesis in May 2010, and was only able to complete it four years later, in 2014, due to military training and other projects that have kept me busy. Thank you so much for your patience and your kind attitude throughout those four years. Your calmness and peace of mind is something I will always look up to.

I would also like to thank the head of the department of Physics, Dr. Michael Stacey, who has always supported me with all the academic, military, and other personal projects I was involved with. Your support far exceeded your duties as head of the department, and I am forever grateful for all those times you helped me and gave me your full trust and confidence.

I am also extremely grateful to the entire department of physics: Luc, Jean-Marc, Ron, Mark, Aralt, Thomas², Joe, Konstantin, Laureline, Kristine, Gregg, Richard, John, Paul, Don, Jennifer, Shawn, Pete, Bryce, Brian, Orest, Steve, Dave, and Manon! I have so many good memories with all of you; it always brings a smile to my face to think of you.

Finally, I would like to thank my friends and my family for their support during those four years. Most of you still have no idea what piezoelectricity is, but you were always there to remind me why this thesis was important. Oscar, Michèle, Françoise, Sandrine, Nicolas, Anne et Marie-France, merci infiniment pour votre amour inconditionnel. Brent, Dan, Alex, Élise, Marie, Caro, Jean-René et Antoine, je suis incroyablement chanceux d'avoir pu partager votre compagnie durant toutes ces belles années et j'espère pouvoir passer bien d'autres bons moments en votre compagnie.

ABSTRACT

Bernier-Brideau, M.O., M.Sc, Royal Military College of Canada, April 2014,
The structural, ferroelectric, dielectric, and electromechanical properties of piezoelectric and electrostrictive materials, Supervisor: Dr. R.G. Sabat.

Piezoelectric materials are used in an increasing number of applications and submitted to a wide range of temperatures, frequencies, pressures, and voltages. Such diverse environmental conditions result in a non-linear piezoelectric response that is difficult to characterize, and the presence of impurities, dopants, and defects add to the complexity of predicting how a material will perform once it is manufactured, especially given the sensitivity of the manufacturing process. Also, recent environmental regulations require new lead-free piezoelectric materials to be developed and studied.

The object of this thesis is to further the knowledge with respect to the structural, ferroelectric, dielectric, and electromechanical properties of piezoelectric and electrostrictive materials in order to facilitate the development of new piezoelectric materials and help optimize current applications. Scanning electron microscope pictures of EC-65, EC-69, and EC-76 were taken, and X-ray diffraction patterns of PLZT 9.5 were obtained at room temperature. Polarization curves were obtained for EC-65, PLZT 9.5, BM-941, BM-600, BM-150, and PMN-PT for electric fields ranging from 0 to $\pm 1000 \text{ kV m}^{-1}$ and temperatures ranging from -40°C to 120°C . Impedance analysis was used to determine the relative permittivity and the dielectric loss tangent of EC-69, PLZT 9.0, PLZT 9.5, and BM-941 for electric fields ranging from 0 to $\pm 2000 \text{ kV m}^{-1}$ and temperatures ranging from -40°C to 140°C with frequencies ranging from 1 kHz to 5000 kHz. Finally, the AC strain amplitude of PLZT 9.0 and BM-941 were obtained for AC electric fields ranging from 0 to $\pm 1000 \text{ kV m}^{-1}$ and a DC bias ranging from 0 to $\pm 1500 \text{ kV m}^{-1}$. Overall, the measurements obtained build

upon the current knowledge of piezoelectric materials, support results obtained by other researchers, and present new results that can be used to develop new materials and optimize current applications.

RÉSUMÉ

Bernier-Brideau, M.O., M.Sc, Collège militaire royal du Canada, avril 2014,
Les propriétés structurales, ferroélectriques, diélectriques et électromécaniques des matériaux piézoélectriques et électrostrictifs, Superviseur: Dr. R.G. Sabat.

Les matériaux piézoélectriques sont utilisés dans un nombre croissant d'applications les soumettant à un large éventail de températures, de fréquences, de pressions et de voltages. Ces conditions environnementales instables engendrent une réponse piézoélectrique non-linéaire qui est difficile à caractériser. De plus, la présence d'impuretés, de dopants et d'imperfections rendent le processus de production et de fabrication précaire et instable. Puis, de nouvelles lois environnementales exigent une diminution de l'utilisation du plomb dans l'industrie de l'électronique et exigent que de nouveaux matériaux piézoélectriques sans plomb soient développés.

L'objectif de cette thèse est d'améliorer les connaissances des propriétés structurales, ferroélectriques, diélectriques et électromécaniques des matériaux piézoélectriques et électrostrictifs afin de faciliter le développement de nouveaux matériaux piézoélectriques et d'optimiser les applications actuelles. Des images de EC-65, EC-69 et EC-76 ont été prises par microscopie électronique à balayage et des réseaux de diffraction à rayons X de PLZT 9.5 ont été capturés. Des courbes de polarisation ont été obtenues pour EC-65, PLZT 9.5, BM-941, BM-600, BM-150 et PMN-PT pour des champs électriques variant de 0 à ± 1000 kV m^{-1} et des températures variant de -40°C à 120°C . L'analyse de l'impédance a été utilisée pour déterminer la permittivité relative et la tangente de perte diélectrique de EC-69, PLZT 9.0, PLZT 9.5 et BM-941 pour des champs électriques variant de 0 à ± 2000 kV m^{-1} et des températures variant de -40°C à 140°C pour des fréquences variant de 1 kHz à 5000 kHz. Finalement, l'amplitude de la déformation de PLZT 9.0 et BM-941 a été obtenue pour des

champs électriques AC variant de 0 à $\pm 1000 \text{ kVm}^{-1}$ avec des champs électriques DC variant de 0 à $\pm 1500 \text{ kVm}^{-1}$. Dans l'ensemble, les mesures obtenues ajoutent aux connaissances actuelles sur les matériaux piézoélectriques, soutiennent des résultats obtenus par d'autres chercheurs et présentent également de nouveaux résultats qui pourront être utilisés dans le développement de nouveaux matériaux piézoélectriques et pour l'optimisation des applications actuelles.

TABLE OF CONTENTS

ACKNOWLEDGEMENTS	iii
ABSTRACT	iv
RÉSUMÉ	vi
LIST OF TABLES	xi
LIST OF FIGURES.....	xii
LIST OF SYMBOLS AND ABBREVIATIONS	xvi
CHAPTER 1 : INTRODUCTION	1
1.1 Piezoelectricity and Pyroelectricity	1
1.2 Early History	2
1.3 Modern History: from Natural Crystals to Piezoelectric Polymers.....	4
1.3.1 Natural Crystals	4
1.3.2 Piezoelectric Ceramics	5
1.3.3 Relaxor Piezoelectric Ceramics	6
1.3.4 Piezoelectric Polymers.....	7
1.3.5 Lead-free Materials.....	9
1.4 Piezoelectricity in Action	10
1.5 Goal of Research.....	13
1.6 Thesis Structure	15
CHAPTER 2 : STRUCTURAL PROPERTIES OF PIEZOELECTRIC MATERIALS	17
2.1 Crystal structure.....	17
2.2 Crystal Symmetry.....	18
2.3 Symmetry Change as a Function of Temperature.....	24
2.4 Linear Piezoelectric Equations.....	26
2.5 Domains	28
2.6 Polarization	31
2.7 Doping	32
2.8 Grain Structure of Ceramics.....	33

2.9	Phase Diagrams	37
2.10	X-ray Diffraction.....	42
2.10.1	Theory.....	42
2.10.2	Results and Discussion.....	44
CHAPTER 3 : FERROELECTRIC PROPERTIES OF PIEZOELECTRIC MATERIALS.		
.....		48
3.1	Theory.....	48
3.2	Experimental procedure.....	51
3.3	Results and Discussion.....	55
3.3.1	EC-65	55
3.3.2	PLZT 9.5	57
3.3.3	BM-941	59
3.3.4	BM-600	61
3.3.5	PMN-PT.....	62
3.3.6	BM-150	64
CHAPTER 4 : DIELECTRIC PROPERTIES OF PIEZOELECTRIC MATERIALS		66
4.1	Theory.....	66
4.2	Experimental Procedure	69
4.3	Results and Discussion.....	70
4.3.1	EC-69	70
4.3.2	PLZT 9.0 and PLZT 9.5.....	73
4.3.3	BM-941	76
CHAPTER 5 : ELECTROMECHANICAL PROPERTIES OF PIEZOELECTRIC MATERIALS		79
5.1	Theory.....	79
5.2	Experimental setup	81
5.3	Results and Discussion.....	85
5.3.1	PLZT 9.0	85
5.3.2	BM-941	90

CHAPTER 6 : CONCLUSION	94
6.1 Conclusion.....	94
RERERENCES.....	98
CURRICULUM VITAE.....	106

LIST OF TABLES

Table 1.1. Materials analyzed in this research.	14
Table 2.1. Crystal systems and crystal point groups with their associated symmetries.	20
Table 2.2. Physical properties of EC-65, EC-69, and EC-76 published by EDO Ceramic. ..	37
Table 2.3. Interlattice spacing as a function of Miller indices and unit cell parameters.	43

LIST OF FIGURES

Figure 1.1. Examples of natural piezoelectric materials.	2
Figure 1.2. Simplification of the direct piezoelectric effect.	3
Figure 1.3. Illustration of an active piezoelectric sonar.	5
Figure 1.4. Manufacturing piezoelectric PVDF.	8
Figure 1.5. Piezoelectric fibers integrated into the Head Intelligence tennis racquet.	11
Figure 1.6. Patents for piezoelectric bicycle frame and golf club.	12
Figure 2.1. Atomic representation of a single crystal, a polycrystal, and an amorphous solid.	18
Figure 2.2. Illustration of the Oh symmetry point group.	21
Figure 2.3. Illustration of the O symmetry point group.	22
Figure 2.4. Illustration of the Td symmetry point group.	23
Figure 2.5. Illustration of the C2v symmetry point group.	23
Figure 2.6. Atomic structure of BaTiO ₃ at 30°C (below T _c).	24
Figure 2.7. Atomic structure of BaTiO ₃ at 200°C (above T _c).	25
Figure 2.8. SEM picture of BaTiO ₃ showing individual domains.	28
Figure 2.9. Schematic representation of domains.	29
Figure 2.10 180° domain wall motion and non-180° domain wall motion.	30
Figure 2.11. Poling of a piezoelectric ceramic.	31
Figure 2.12. SEM picture of EC-65 at magnification 6500×.	34
Figure 2.13. SEM picture of EC-65 at magnification 12000×.	34
Figure 2.14. SEM picture of EC-69 at magnification 6500×.	35
Figure 2.15. SEM picture of EC-69 at magnification 12000×.	35

Figure 2.16. SEM picture of EC-76 at magnification 6500×.	36
Figure 2.17. SEM picture of EC-76 at magnification 12000×.	36
Figure 2.18. PZT phase diagram by Jaffe	38
Figure 2.19. New PZT phase diagram by Pandey & Ragini	40
Figure 2.20. Haertling's phase diagram for PLZT.....	41
Figure 2.21. X-ray diffraction peaks for PLZT 9.5 at room temperature.	45
Figure 2.22. Scitag Lattice Refinement Program for PLZT 9.5.....	47
Figure 3.1. The relationship between piezoelectric, pyroelectric, and ferroelectric materials.	48
Figure 3.2. The hysteresis loops of a simple dielectric, a paraelectric, and a ferroelectric material.	49
Figure 3.3. A typical hysteresis loop for a ferroelectric material.	50
Figure 3.4. Experimental setup used to obtain the polarization curves.....	52
Figure 3.5. Polarization curves of EC-65 as a function of frequency.	54
Figure 3.6. Polarization curves of EC-65 from 20°C to 120°C.....	56
Figure 3.7. Polarization curves of PLZT 9.5 from 20°C to -40°C.....	58
Figure 3.8. Polarization curves of BM-941 from 30°C to 90°C.....	60
Figure 3.9. The polarization curve of BM-600 at 20°C.	62
Figure 3.10. The polarization curve of PMN-PT at 20°C.....	63
Figure 3.11. The polarization curve of BM-150 at 20°C.....	65
Figure 4.1. Equivalent circuit diagram for a piezoelectric ceramic.....	67
Figure 4.2. The experimental setup used to find the relative permittivity and the dielectric loss tangent as a function of temperature.	70
Figure 4.3. The relative permittivity of EC-69 as a function of temperature at various probing frequencies.	72

Figure 4.4. The dielectric loss tangent of EC-69 as a function of temperature at various probing frequencies.	72
Figure 4.5. The relative permittivity of PLZT 9.0 as a function of temperature at various probing frequencies.	74
Figure 4.6. The dielectric loss tangent of PLZT 9.0 as a function of temperature at various probing frequencies.	74
Figure 4.7. The relative permittivity of PLZT 9.5 as a function of temperature at various probing frequencies.	75
Figure 4.8 The dielectric loss tangent of PLZT 9.5 as a function of temperature at various probing frequencies.	75
Figure 4.9. The relative permittivity of PLZT 9.0 compared to PLZT 9.5 as a function of temperature at 100 kHz.....	76
Figure 4.10. The relative permittivity of BM-941 as a function of temperature at various probing frequencies.	77
Figure 4.11. The dielectric loss tangent of BM-941 as a function of temperature at various probing frequencies.	78
Figure 5.1. A typical Fourier transform of the displacement magnitude obtained by VIBSOFT 4.5 at 110 Hz for PLZT 9.0 at $278 \text{ kV}_{\text{AC}}\text{m}^{-1}$ and $500 \text{ kV}_{\text{DC}}\text{m}^{-1}$	81
Figure 5.2. Experimental setup used to obtain the AC strain amplitude as a function of the AC and DC electric fields.	82
Figure 5.3. A schematic representation of the Polytec assembly [90].	84
Figure 5.4. Mechanical resonance peaks for the second harmonic of the PLZT 9.0 sample and fixture at $300 \text{ kV}_{\text{AC}}\text{m}^{-1}$ and $0 \text{ kV}_{\text{DC}}\text{m}^{-1}$	86
Figure 5.5. The AC strain amplitude of PLZT 9.0 as a function of the AC electric field amplitude, with no DC bias for different frequencies at the 1 st and 2 nd harmonic frequencies.	87
Figure 5.6. The AC strain amplitude of PLZT 9.0 as a function of the DC bias electric field, with a $278 \text{ kV}_{\text{m}^{-1}}$ peak-to-peak AC electric field for different frequencies at the 1 st and 2 nd harmonic frequencies.	88
Figure 5.7. The AC strain amplitude of PLZT 9.0 at 150 Hz at the first harmonic frequency as a function of the DC bias electric field at various AC fields. The DC field cycled	

from 0 kVm^{-1} to 1000 kVm^{-1} , down to 0 kVm^{-1} , then -1000 kVm^{-1} , and then back up to 0 kVm^{-1} 90

Figure 5.8. Mechanical resonance peaks for the first harmonic of the BM-941 sample and structure at 500 $\text{kV}_{\text{AC}}\text{m}^{-1}$ and 0 $\text{kV}_{\text{DC}}\text{m}^{-1}$ 91

Figure 5.9. The AC strain amplitude of BM-941 as a function of the AC electric field amplitude, with no DC bias for different frequencies at the first harmonic frequency.. 92

Figure 5.10. The AC strain amplitude of BM-941 at the first harmonic frequency for various frequencies as a function of the DC bias electric field at 700 $\text{kV}_{\text{AC}}\text{m}^{-1}$ 93

LIST OF SYMBOLS AND ABBREVIATIONS

BaTiO ₃	Barium Titanate
PbZrO ₃	Lead Zirconate
PbZrTiO ₃	Lead Zirconate Titanate
PZT	Lead Zirconate Titanate
PLZT	Lead Lanthanum Zirconate Titanate
PZN-PT	Lead Zinc Niobate / Lead Titanate
PMN	Lead Magnesium Niobate
PMN-PT	Lead Magnesium Niobate / Lead Titanate
PNN	Lead Nickel Niobate
PN	Lead Metaniobate
PVDF	Polyvinylidene Fluoride
Pb	Lead
Zr	Zirconium
La	Lanthanum
Ti	Titanium
HeNe	Helium Neon
RoHS	Restriction of Hazardous Substances
SEM	Scanning Electron Microscope
XRD	X-Ray Diffraction
PRAP	Piezoelectric Resonance Analysis Program
VIBSOFT	Vibration Analysis Software Program
LDV	Laser Doppler Vibrometer
COS	Center of Symmetry
DAQ	Data Acquisition

USB	Universal Serial Bus
GPIO	General Purpose Interface Bus
T_c	Curie Temperature
Q	Mechanical factor
G	Gibbs Function
D_m	Electric Displacement
S_{ij}	Strain
T_{ij}	Stress
E	Electric Field
ϵ_r	Relative Permittivity
ϵ_0	Permittivity of Free Space
d_{33}	Piezoelectric Coefficient
s	Elastic Compliance
K_{33}^T	Relative Dielectric Permittivity
k_{33}	Coupling Factor
I_{tot}	Total Light Intensity
P	Polarization
$\langle p \rangle$	Average Electric Dipole Moment
V	Volume
Q	Charge
A	Area
Δl	Path Length Difference
v	Velocity
f_d	Doppler Frequency Shift
f_b	Bragg Frequency Shift

λ	Wavelength
d	Spacing
AC	Alternating Current
DC	Direct Current
RC	Resistor Capacitor
C	Capacitance
L	Inductance
R	Resistance
X	Reactance
Y	Admittance
G	Conductance
B	Suspectance
$\tan\delta$	Loss tangent

CHAPTER 1 : INTRODUCTION

1.1 Piezoelectricity and Pyroelectricity

Piezoelectricity [pee-eh-zo-eh-lek-tris-ət-ē] is an electrical and mechanical phenomenon, and it comes from the Greek root “piezin” which means “to press”, and “electricity” which comes from “elektron”, the Greek word for amber, an ancient source of electric charge [1]. This natural phenomenon has been observed for centuries and was sometimes seen when two pieces of quartz were struck together, resulting in a small spark. Quartz is a natural piezoelectric material, so applying pressure on the quartz crystals generated sparks and electricity.

Another phenomenon closely related to piezoelectricity is pyroelectricity [pahy-roh-eh-lek-tris-ət-ē]. “Pyro” comes from the Greek word for fire. In this case, electricity, or more precisely polarization, is produced when some materials are heated or cooled. This phenomenon was also observed long ago when tourmaline was heated and pieces of straw and ash were attracted to the crystal [2]. For many centuries, piezoelectricity and pyroelectricity remained a scientific curiosity. It took a long time before the full potential of piezoelectric materials was realized, and many prominent scientists studied this phenomenon at some point in history: Louis Lemery, Charles Coulomb, Carl Linnaeus, Franz Aepinus, René Just Haüy, Antoine César Becquerel, David Brewster, Lord Kelvin, Pierre and Jacques Curie, Gabriel Lippmann, Woldemar Voigt, Paul Langevin, and many more. Nowadays, piezoelectric materials are part of everyday life. They are found in watches, computers, cars,

radios, printers, medical equipment, and even in the most advanced telecommunication satellites.

1.2 Early History

Pyroelectricity was first described, although not named as such, by Louis Lemery, in 1717, who first related the phenomenon to electric charges [3]. The first scientist to coin the term “pyroelectricity” was Sir David Brewster, in 1824, who also discovered the effect in other crystals such as topaz, cane sugar, and Rochelle salt. Figure 1.1 presents a few examples of natural piezoelectric materials.

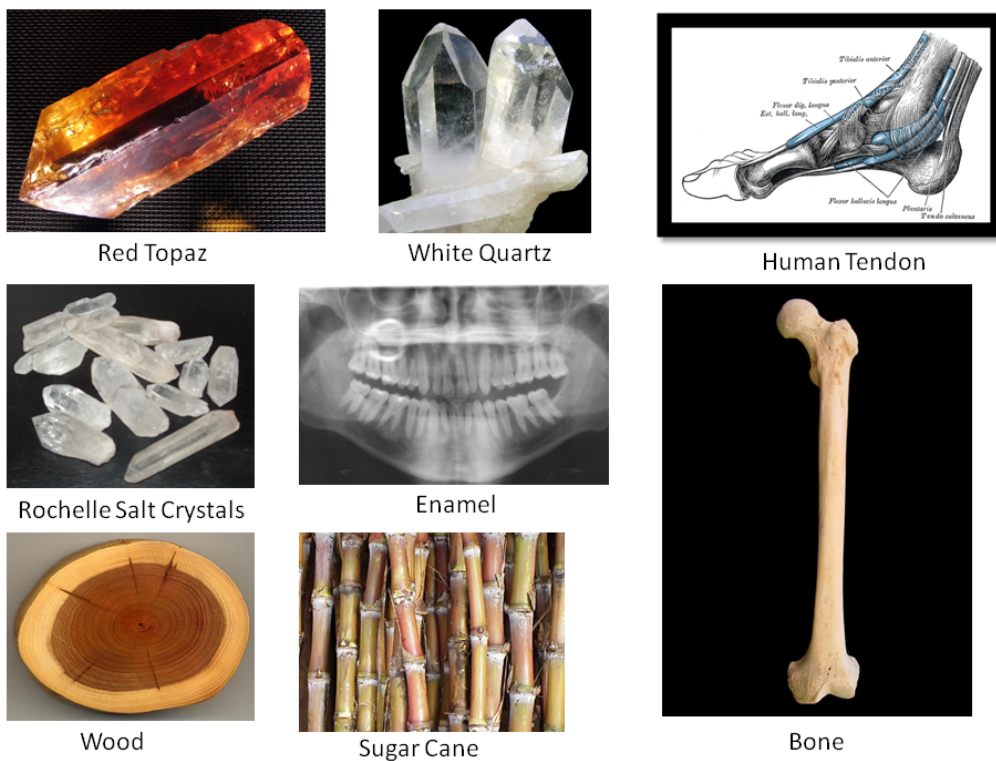


Figure 1.1. Examples of natural piezoelectric materials. [4]

Haüy and Becquerel attempted, unsuccessfully, to find a relationship between mechanical stress and electric polarization, as Coulomb had previously suggested [5]. In 1878, William Thomson, also known as Lord Kelvin, helped to develop a theory for the processes behind pyroelectricity and postulated that a state of permanent polarization was responsible for the phenomenon. Then, in 1880, Pierre Curie and his brother, Jacques Curie, made the first demonstration of the direct piezoelectric effect, as illustrated in Figure 1.2 [6]. In the direct piezoelectric effect, when an expansive force is applied to a non-centrosymmetric crystal, larger dipoles in the atoms are created, resulting in a positive polarization. Similarly, when a compressive force is applied, the dipoles become smaller, resulting in a negative polarization. Conversely, according to the converse piezoelectric effect, a net deformation of the material occurs when an electric field is applied to a piezoelectric material.

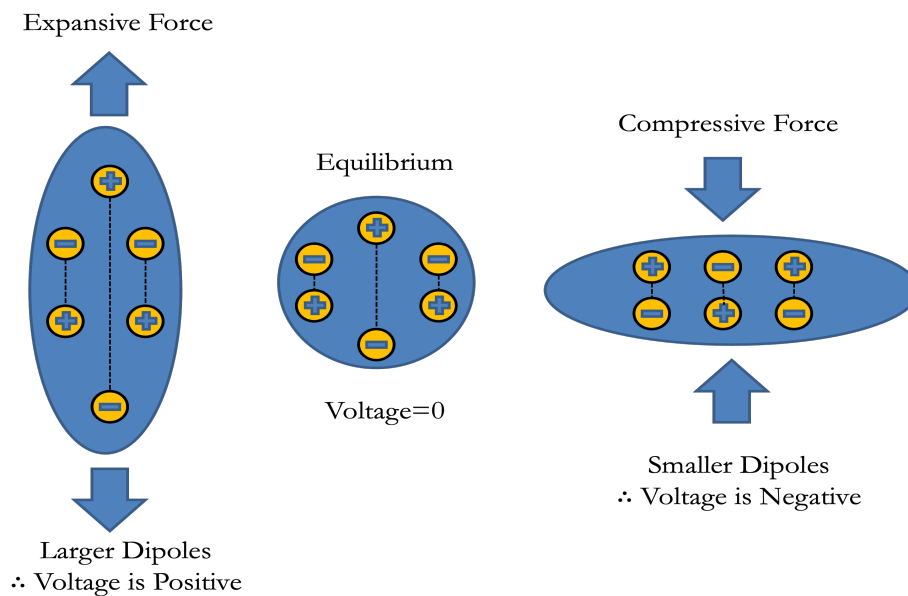


Figure 1.2. Simplification of the direct piezoelectric effect.

In 1881, Lippmann postulated the existence of the converse piezoelectric effect, according to the fundamental thermodynamic principles he had developed [7]. In 1882, the

Curie brothers were able to confirm this effect experimentally. At that time, the relationship between pyroelectricity and piezoelectricity was still unclear. It took almost three decades before Woldemar Voigt published his treatise on crystal structure, *Lehrbuch der Kristallphysik*, [8] in 1910, which accurately described the 20 piezoelectric crystal groups, of which only 10 were pyroelectric due to their natural spontaneous polarization. Voigt was also the first scientist to rigorously describe the piezoelectric coefficients using tensor analysis.

1.3 Modern History: from Natural Crystals to Piezoelectric Polymers

1.3.1 Natural Crystals

Until 1910, the piezoelectric effect had been of scientific interest only and it did not have any useful applications. However, with the onset of World War I, the necessity to detect enemy submarines led Paul Langevin to develop ultrasonic technology and sonar using piezoelectric materials [9] [10]. Early sonar technology had been developed in 1912 after the sinking of the Titanic, but it wasn't until Langevin integrated piezoelectric crystals that sonar technology became effective. Most sonars make use of the converse piezoelectric effect to generate an ultrasonic wave which can hit a target and is then reflected back onto the sonar. The sonar utilizes the direct piezoelectric effect to transform the reflected wave back into an electrical signal, which can be analyzed to determine the position and velocity of the target, as demonstrated in Figure 1.3 [11]. Thus, sonar became the first practical application of the piezoelectric effect.

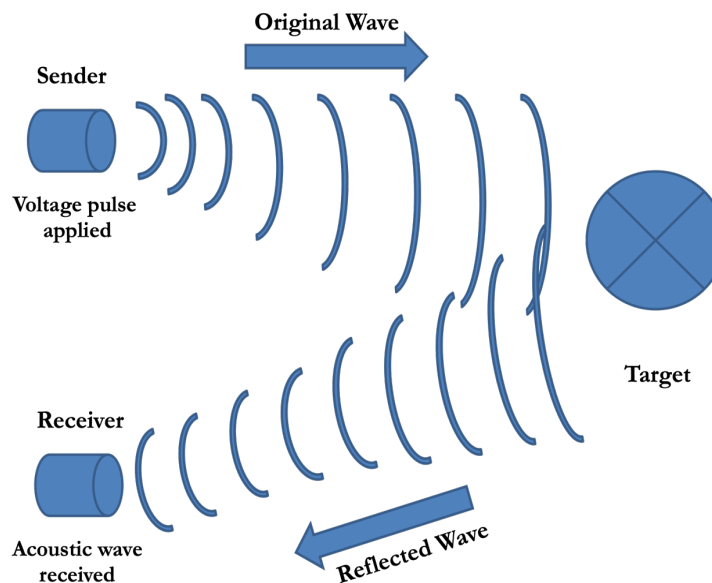


Figure 1.3. Illustration of an active piezoelectric sonar. An acoustic wave is generated when a voltage pulse is applied to the piezoelectric material. The wave hits the target and is reflected back onto the receiver. The receiver transforms the received acoustic wave into an electrical signal, which can then be analyzed. Note that the sender can be the same as the receiver.

From that moment onwards, a multitude of new applications were developed from natural occurring crystals: ultrasonic transducers, microphones, pick-ups, accelerometers, electronic phonographs, signal filters, frequency stabilizers, actuators, flaw detection in solids, viscosity measurements in fluids and gases, etc. A good discussion on early applications of piezoelectric materials can be found in Cross [12]. In fact, most of the classic piezoelectric applications that are used today were designed and produced during the period following World War I. Unfortunately, the only materials available at that time were natural occurring crystals, which limited performance and commercial exploitation [13].

1.3.2 Piezoelectric Ceramics

Before the end of World War II, the most common piezoelectric materials were quartz, Rochelle salt, and ammonium dihydrogen phosphate [14]. The limited supply of

natural piezoelectric crystals during the War caused independent research groups to search for artificial piezoelectric materials in the form of ceramics. In 1945, independent publications from researchers in the USSR and the United States of America exposed a new type of ferroelectric material consisting of barium titanate (BaTiO_3) in a polycrystalline ceramic form [12]. It was produced by mixing a specific ratio of barium and titanium oxide, mixed with an appropriate binder, and then pressed and sintered at very high temperatures.

Subsequently, in 1951, Shirane *et al.* [15] from the Tokyo Institute of Technology reported weak piezoelectric characteristics in lead-zirconate (PbZrO_3), but it was Jaffe *et al.* [16] [17], in 1954, who first reported strong piezoelectric effects in lead-zirconate-titanate (PbZrTiO_3) solid solutions. This led to the development of a wide variety of polycrystalline lead-zirconate-titanate ceramics that are generally referred to as PZT. These have major advantages over barium titanate ceramics, including high piezoelectric coefficients, and as a result began to dominate the piezoelectric commercial market [18].

1.3.3 Relaxor Piezoelectric Ceramics

Studies on relaxor ferroelectrics originated soon after the discovery of the first polycrystalline piezoelectric ceramics, BaTiO_3 . In the 1950s, Russian scientist G. Smolensky [19] was the first to report relaxor behavior in perovskite structure electroceramics. Originally classified as ferroelectrics with diffuse phase transitions, it was gradually understood that the strong dielectric response being highly dispersive did not correspond to a classical ferroelectric phase transition. Researchers from the Penn State University who were actively working on this type of materials suggested the name “relaxor ferroelectrics” which has now become the typical designation [20].

Early relaxor ferroelectrics were generally produced as single crystals, as they could more easily be grown artificially for fabricating large arrays with a high electromechanical coupling factor. The electromechanical coupling factor is important because it represents the effectiveness of a piezoelectric material to convert electrical energy to mechanical energy, and vice versa [21]. In 1981, Kuwata *et al.* [22] [23] reported that single crystals of the solid solution of lead-zinc-niobate/lead-titanate, abbreviated PZN-PT, possessed an electromechanical coupling factor greater than 0.9, whereas the highest value for PZT ceramics was around 0.7.

Since then, interest in piezoelectric relaxors has grown rapidly and many other relaxor-based ferroelectrics have been developed, not only single crystals, but also ceramics. Lead-magnesium-niobate (PMN), lead-magnesium-niobate/lead-titanate (PMN-PT), lead-nickel-niobate (PNN), and lead-lanthanum-zirconate-titanate (PLZT) are currently among the most studied relaxor materials [24].

1.3.4 Piezoelectric Polymers

Two other important aspects in the development of piezoelectric materials also occurred during the later part of the 20th century: the discovery that certain types of polymer possess useful piezoelectric properties, and the development of thin film piezoelectric polymers capable of operating at frequencies beyond 100 MHz. Piezoelectric effects had been observed in polymers prior to the 1950s in materials such as carnauba wax, tendon, and wood [25]. However, the dielectric coefficients observed were so low that little research had been conducted. Nevertheless, in the early 1950s, shear piezoelectricity was investigated in polymers of biological origin such as cellulose and collagen, and in synthetic polymers such as polyamides and polylactic acids, and higher dielectric coefficients were discovered [26].

In 1969, Kawai reported that a plastic polymer, polyvinylidene fluoride (PVDF), exhibited ferroelectric and piezoelectric properties several times greater than quartz. PVDF is a special plastic material in the fluoropolymer family which is generally used in applications requiring the highest purity, strength, and resistance to solvents, acids, bases, and heat [27]. PVDF must be stretched and poled under high voltage in order to become piezoelectric, because the $C_2H_2F_2$ molecules have a natural random orientation. Figure 1.4 illustrates this process.

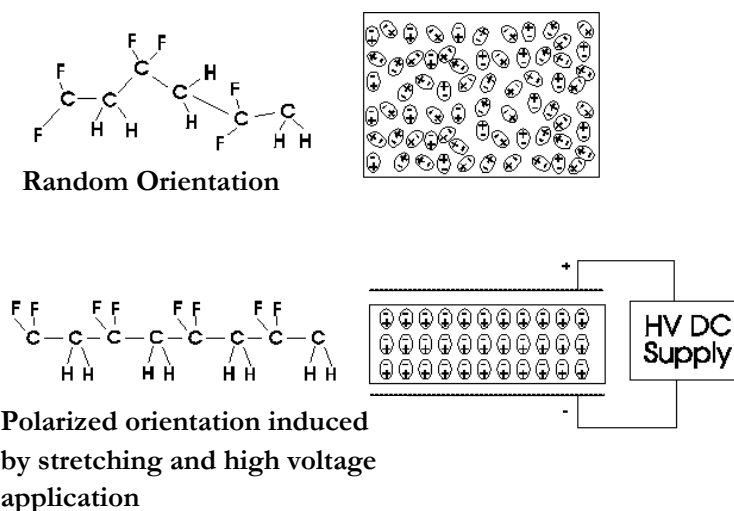


Figure 1.4. Manufacturing piezoelectric PVDF. [28]

Sheets of different thickness can be produced economically, enabling broadband transducers that are effective in the 10-100 MHz range to be manufactured. Their price, efficiency, and ability to conform to a variety of shapes have resulted in a very wide range of applications in consumer products. In addition, PVDF has enabled effective transducers to be fabricated for hydrophones, high-frequencies imaging, and ultrasound biomicroscopy. For the purpose of generating and detecting ultrasound at very high frequencies, well beyond

that considered possible with piezoelectric ceramics, considerable effort was devoted to developing thin PVDF films effective beyond 100 MHz, and research is still ongoing [29].

Since the discovery of piezoelectricity in PVDF, piezoelectric and ferroelectric properties were also investigated in many other polymers. Microphones using a stretched film of polymethyl glutamate were reported in 1970 [25]. Ultrasonic transducers using elongated and poled films of copolymers of PVDF were produced in 1972. Headphones and tweeters using vinylidene fluoride were marketed in 1975. Since then, hydrophones and various electromechanical devices utilizing PVDF and its copolymers have been developed. The most recent studies involve micro-deposition of films of aromatic and aliphatic polyureas, copolymers of vinylidene fluoride and trifluoroethylene, and copolymers of vinylcyanide and vinylacetate [26].

1.3.5 Lead-free Materials

More recently, demand has been growing for materials that are benign to the environment and human health. Many government regulations, such as the Restriction of Hazardous Substances (RoHS) directives in Europe, have been enacted in response to this demand [30]. The 2002 European RoHS directive restricts hazardous substances used in electrical and electronic equipment, including lead. However, due to the lack of comparable alternatives, piezoelectric materials containing lead, such as PZT, were given a “temporary exemption” from this RoHS regulation [31] [32].

Subsequently, three major families of lead-free piezoceramic materials have been actively researched: perovskite (NaNbO_3 , KNaNbO_3 , $\text{Ba}_2\text{AlNbO}_6$), tungsten-bronze (SBN, PBN, BLTN, BNTN, BSTN), and bismuth-layer (BiFeO_3 , NBT, KBT) structure [33] [34]. To this day, none of these lead-free piezoelectric materials is fully ready to replace PZT-

based materials. Moreover, the properties of lead-free piezoceramics under different conditions of pressure, frequency, and temperature are not well understood compared to PZT ceramics, and they generally suffer from unsteady manufacturing processes. Thus, the RoHS exemption status for PZT electronics was re-evaluated in July 2011 [35], and further exemption status was granted for the moment.

1.4 Piezoelectricity in Action

Technical applications of piezoelectric materials include: sonar, ultrasonic transducers, microphones, pick-ups, accelerometers, electronic phonographs, scanning tunneling microscopes, signal filters, frequency stabilizers, precision actuators, flaw detection in solids, viscosity measurements, hydrophones, high-frequencies imaging, ultrasound biomicroscopy, etc. However, many other day-to-day items make use of the piezoelectric effect: cigarette lighters, propane barbeques, ink-jet printers, noise-cancelling earphones, singing birthday cards, and car fuel injectors. Furthermore, a recent trend has been observed in the world of sports: integrating piezoelectric materials in sports equipment. Piezoelectric materials have made their way into the world of tennis, squash, golf, pool, ski, snowboard, and golf.

Tennis manufacturer Head was trying to design racquets that were more powerful, but also more comfortable [36]. Previously, racquets had been designed to be relatively stiff so that they returned maximum energy to the ball when it is hit, but this meant that the racquet transmitted shock vibration to the player's arm. In an attempt to reduce vibration, piezoelectric fibers were embedded around the racquet throat and a computer chip was embedded inside the handle. The frame deflects slightly when the ball is hit, so that the piezoelectric fibers bend and generate a charge, which is collected by the patterned electrode

surrounding the fibers, as seen in Figure 1.5. The charge and associated current is carried to an embedded silicon chip via a flexible circuit containing inductors, capacitors, and resistors, which boosts the current and sends it back to the fibers out of phase in an attempt to reduce the vibration by destructive interference.

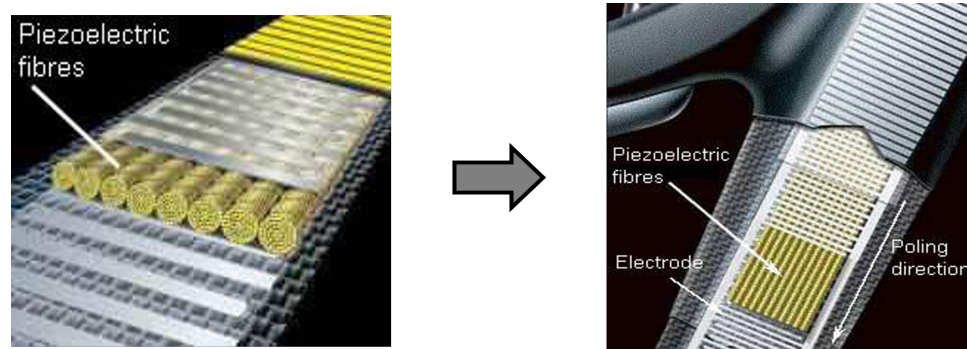


Figure 1.5. Piezoelectric fibers integrated into the Head Intelligence tennis racquet. [36]

The current generated is only a couple of hundred micro amps, but it generates up to 800 volts in 2 to 3 milliseconds. The manufacturer claims a 50% reduction in vibration compared with conventional rackets, and the International Tennis Federation has approved them for tournament play. According to Advanced Cerametrics Inc., the fibers used in several of Head's tennis rackets add up to 15% more power to a ball hit [37]. The Intelligence, Protector, and LiquidMetal lines of rackets using these piezoelectric ceramic fibers were the largest selling rackets in the world in the 2009/2010 season, and they have been clinically proven to eliminate tennis elbow.

Aside from tennis, piezoelectric materials are used in many other sports. In the summer of 2006, smart pool cues made by Hamson Industries with these fibers won the largest prize ever in a pool tournament. In addition, the use of piezoelectric elements for passive electronic damping has also been proven to work effectively with the K2 downhill

ski. The K2 ski designers used a resistor and capacitor (RC) shunt circuit to dissipate the vibration energy absorbed by piezoelectric materials imbedded into the skis. Ceramic fiber technology also provides up to 6% more functional edge, helping athletes at the 2010 Winter Olympics win two gold medals and one silver medal [37]. Also, Active Control eXperts Inc. developed the Copperhead ACX baseball bat with shunted piezoceramic materials that convert the mechanical vibration energy into electrical energy. This method of damping significantly reduces the sting during impact and gives the bat a larger sweet spot [38]. Finally, more recently, detailed patents have been submitted for a bicycle frame and golf club in 2010 [39] [40], as depicted in Figure 1.6.

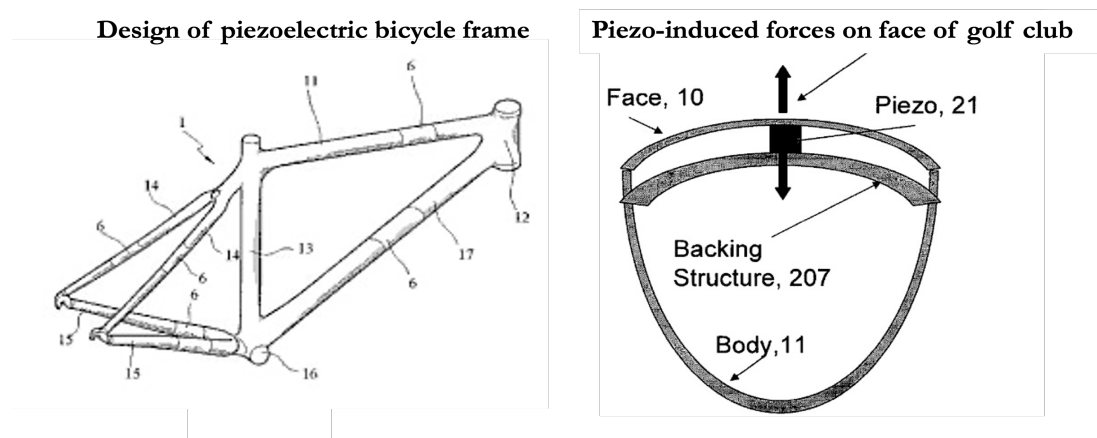


Figure 1.6. Patents for piezoelectric bicycle frame and golf club. On the left side is an illustration from the patent “Vibration suppressed bicycle structure” deposited by Shan Li *et al.* [39], and on the right side is an illustration from the patent “Active Control of Golf Club Impact” by Nesbitt Hagood *et al.* in 2010 [40].

1.5 Goal of Research

The goal of this thesis is to improve the understanding of piezoelectric materials in order to facilitate the development of new materials and help optimize current piezoelectric applications. Due to the wide range of applications of piezoelectric materials, they have to function over a broad range of frequencies, temperatures, pressures and voltages. Such diverse environmental conditions will result in a non-linear piezoelectric response, and the presence of impurities, dopants, and defects add to the complexity of predicting how a material will perform once it is manufactured. Moreover, the exact material composition, the molecular structure, the grain size, and the ageing process all critically affect the piezoelectric material properties. The manufacturing process is also extremely sensitive, and manufacturers all over the world struggle to mass produce piezoelectric materials. Furthermore, recent environmental concerns require new lead-free piezoelectric materials to be developed and studied. The theory behind piezoelectricity is complex, and there is still a wide gap between the existing theory and experimental results.

Specifically, the object of this thesis is to further the knowledge with respect to:

- Material composition: Different materials are analyzed and compared, including PZT, PLZT, PMN-PT, and PN (see Table 1.1);
- Frequency dependence: Hysteresis, dielectric, and strain measurements are obtained at different frequencies over a range of 1Hz to 5000kHz;
- Temperature dependence: Hysteresis and dielectric measurements are obtained over a range of -150 to 200°C;
- Electric field dependence: Hysteresis and strain measurements are obtained for different electric fields ranging from 0 to 2 MVm⁻¹;

- DC Voltage: A DC bias of -1.0 MVm^{-1} to 1.0 MVm^{-1} was introduced for strain measurements;
- Grain size: SEM pictures were obtained for different compositions of PZT;
- Dopants: Soft and hard PZT are analyzed, as well as PLZT 9.0 and PLZT 9.5;
- Crystal structure: X-ray diffraction measurements of PLZT were obtained in order to verify its crystal structure at room temperature.

Overall, the measurements obtained build upon the current knowledge of piezoelectric materials, support results obtained by other researchers, but also present new information that can be used to help the manufacturing process and the applications of piezoelectric materials.

Table 1.1. Materials analyzed in this research.

Acronym	Name	Chemical Composition	Manufacturer
EC-65	Lead Zirconate Titanate (Soft)	$\text{Pb}(\text{ZrTi})\text{O}_3$	EDO Ceramic
EC-69	Lead Zirconate Titanate (Hard)	$\text{Pb}(\text{ZrTi})\text{O}_3$	EDO Ceramic
EC-76	Lead Zirconate Titanate (Soft)	$\text{Pb}(\text{ZrTi})\text{O}_3$	EDO Ceramic
PLZT 9.0	Lead Lanthanum Titanate Zirconate (9.0/65/35)	$\text{Pb}_{0.910}\text{La}_{0.090}(\text{Zr}_{0.65}\text{Ti}_{0.35})_{0.97750}\text{O}_3$	Motorola/ CTS Electronic Components
PLZT 9.5	Lead Lanthanum Titanate Zirconate (9.5/65/35)	$\text{Pb}_{0.905}\text{La}_{0.095}(\text{Zr}_{0.65}\text{Ti}_{0.35})_{0.97625}\text{O}_3$	Motorola/ CTS Electronic Components
BM-150	Unknown (Lead-free)	Unknown (Lead-free)	Sensor Technology Ltd.
BM-600	Lead Magnesium Niobate (modified)	$\text{Pb}(\text{Mg}_3\text{Nb}_2)\text{O}_3$	Sensor Technology Ltd.
BM-941	Lead Metaniobate (modified)	$\text{Pb}(\text{NbO}_3)_2$	Sensor Technology Ltd.
PMN-PT	Lead-Magnesium-Niobate/Lead-Titanate	$\text{Pb}(\text{Mg}_3\text{Nb}_2)\text{O}_3/\text{PbTiO}_3$	TRS Technologies

1.6 Thesis Structure

This thesis is divided into 6 chapters. Chapter 1 presents the history of piezoelectric materials, explains the different types of piezoelectric materials, from crystals to ceramics, polymers and lead-free ceramics, and finally many applications of piezoelectric materials are presented.

Chapter 2 covers the structural properties of piezoelectric materials. Crystal structure, crystal symmetry, symmetry changes as a function of temperature, linear piezoelectric equations, domains, polarization, doping, grain size, and phase diagrams are explained. X-ray diffraction was performed on PLZT 9.5 and the results are included in this chapter because they are closely related to crystal symmetry and phase diagrams.

Chapter 3 explores the ferroelectric properties of piezoelectric materials. The relationship between piezoelectricity and ferroelectricity is explained and polarization curves are explained. The experimental procedure is then outlined. Finally, polarization curves are presented and for EC-65, PLZT 9.5, BM-941, BM-600, PMN-PT, and BM-150.

Chapter 4 focuses on the dielectric properties of piezoelectric materials. The first section describes how impedance can be used to determine the relative permittivity and the dielectric loss tangent of piezoelectric materials. Then, the experimental procedure and the impedance analyzer are presented. Finally, the relative permittivity and the dielectric loss tangent of EC-69, PLZT 9.0, PLZT 9.5, and BM-941 are presented and analyzed.

Chapter 5 covers the electromechanical properties of piezoelectric and electrostrictive materials. The adiabatic Gibbs function is used to derive non-linear piezoelectric equations, and piezoelectric and electrostrictive coefficients are derived from these equations. The experimental procedure and the laser Doppler vibrometer are then

presented. Then, the AC strain amplitude of PLZT 9.0 and BM-941, with and without a DC bias, is presented.

Finally, Chapter 6 offers concluding remarks, observations, and ideas for future work.

CHAPTER 2 : STRUCTURAL PROPERTIES OF PIEZOELECTRIC MATERIALS

Chapter 2 begins with a discussion on the microscopic structure of piezoelectric materials, including crystal structure, crystal symmetry, and symmetry changes as a function of temperature. Then, the macroscopic structure of piezoelectric materials is examined, including domains, grain size, and polarization. Linear piezoelectric equations and phase diagrams are also explained. Finally, X-ray diffraction was performed on PLZT 9.5 and the results are included in this chapter because they are closely related to crystal symmetry and phase diagrams.

2.1 Crystal structure

All solids can be classified into three categories: single crystals, polycrystals, and amorphous solids. The fundamental difference between these three categories is the length scale over which there is periodicity between the atoms. Ideal single crystals have infinite periodicity, polycrystals have finite periodicity, and amorphous solids have no apparent periodicity, as depicted in Figure 2.1. Examples of single crystals include quartz, diamond, and table salt; polycrystals include most metals, ceramics, ice, and rocks; and amorphous solids include glass, gels, and thin films. All of the materials analyzed in this thesis are polycrystals.

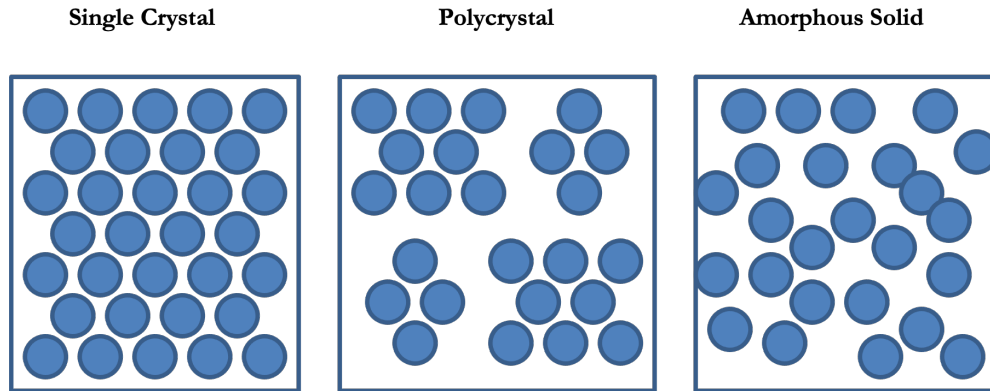


Figure 2.1. Atomic representation of a single crystal, a polycrystal, and an amorphous solid. Classification is defined by periodicity.

The piezoelectric theory for perfect single crystals is relatively straightforward, and linear piezoelectric equations have been derived to describe the phenomenon [41]. Unfortunately, single crystals are hard to grow, and they often contain impurities and defects that affect their piezoelectric properties. Furthermore, the majority of piezoelectric materials produced today are ceramics that fall under the polycrystal category, containing defects and impurities, but also domains, grains, and boundaries on a macroscopic scale.

2.2 Crystal Symmetry

All crystals grow with some periodicity while trying to minimize their total potential energy as per the laws of thermodynamics. Their constituting atoms are forced to adopt one of the seven elementary *crystal systems* (cubic, tetragonal, monoclinic, triclinic, orthorhombic, trigonal, and hexagonal). Each of these crystal systems can further be sub-divided into a total of 32 *point groups* based on symmetry. The point groups and their symmetry define piezoelectricity and pyroelectricity. Applying pressure on a point group with very high symmetry cannot generate electricity because all of the dipoles formed under the crystal deformation cancel out symmetrically, and no net polarization is observed. Table 2.1 shows the seven different crystal systems with the 32 symmetry point groups. Both the Schonflies

and the Hermann-Mauguin notations are given in Table 2.1, but only the Schonflies notation will be used throughout this thesis. The three different elements of symmetry in a crystal structure, namely the axes of symmetry, the planes of symmetry, and the center of symmetry (COS), are also given. Finally, the piezoelectric and pyroelectric properties are defined in the last two columns.

Table 2.1. Crystal systems and crystal point groups with their associated symmetries. Tabulated by the author using multiple sources [94] [95] [96].

Crystal System	Point Group	Schonflies notation	Hermann-Mauguin notation	Axes of Symmetry (Axes of Rotation)				Planes of Symmetry (Mirror planes)	Center of Symmetry	Piezoelectric	Pyroelectric
				2-Fold	3-Fold	4-Fold	6-Fold				
Cubic (Isometric)	Tetartoidal	T	23	3	4	-	-	-	-	yes	-
	Diploidal	Th	2/m $\bar{3}$	3	4	-	-	3	yes	-	-
	Hextetrahedral	Td	$\bar{4}$ 3m	3	4	-	-	6	-	yes	-
	Gyroidal	O	432	6	4	3	-	-	-	no*	-
	Hexoctahedral	Oh	4/m $\bar{3}$ 2/m	6	4	3	-	9	yes	-	-
Tetragonal	Disphenoidal	S4	$\bar{4}$	1	-	-	-	-	-	yes	-
	Pyramidal	C4	4	-	-	1	-	-	-	yes	yes
	Dipyramidal	C4h	4/m	-	-	1	-	1	yes	-	-
	Scalenohehdral	D2d	$\bar{4}$ 2m	3	-	-	-	2	-	yes	-
	Ditetragonal pyramidal	C4v	4mm	-	-	-	-	4	-	yes	yes
	Trapezohedral	D4	422	4	-	1	-	-	-	yes	-
	Ditetragonal-Dipyramidal	D4h	4/m 2/m 2/m	4	-	1	-	5	yes	-	-
Orthorhombic	Pyramidal	C2v	mm2	1	-	-	-	2	-	yes	yes
	Disphenoidal	D2	222	3	-	-	-	-	-	yes	-
	Dipyramidal	D2h	2/m 2/m 2/m	3	-	-	-	3	yes	-	-
Hexagonal	Trigonal Dipyramidal	C3h	$\bar{6}$	-	1	-	-	1	-	yes	-
	Pyramidal	C6	6	-	-	-	1	-	-	yes	yes
	Dipyramidal	C6h	6/m	-	-	-	1	1	yes	-	-
	Ditrigonal Dipyramidal	D3h	6m2	3	1	-	-	4	-	yes	-
	Dihexagonal Pyramidal	C6v	6mm	-	-	-	1	6	-	yes	yes
	Trapezohedral	D6	622	6	-	-	1	-	-	yes	-
	Dihexagonal Dipyramidal	D6h	6/m 2/m 2/m	6	-	-	1	7	yes	-	-
Trigonal	Pyramidal	C3	3	-	1	-	-	-	-	yes	yes
	Rhombohedral	C3i	$\bar{3}$	-	1	-	-	-	yes	-	-
	Ditrigonal Pyramidal	C3v	3m	-	1	-	-	3	-	yes	yes
	Trapezohedral	D3	32	3	1	-	-	-	-	yes	-
	Hexagonal Scalenohehdral	D3d	$\bar{3}$ 2/m	3	1	-	-	3	yes	-	-
Monoclinic	Domatic	Cs	m	-	-	-	-	1	-	yes	yes
	Sphenoidal	C2	2	1	-	-	-	-	-	yes	yes
	Prismatic	C2h	2/m	1	-	-	-	1	yes	-	-
Triclinic	Pedial	C1	1	-	-	-	-	-	-	yes	yes
	Pinacooidal	Ci	$\bar{1}$	-	-	-	-	-	yes	-	-

Table 2.1 shows that 20 of the 32 point groups are piezoelectric, and 10 of the 20 piezoelectric point groups are pyroelectric. The point groups O_h , T_d , O , and C_{2v} are pictured in Figure 2.2 to 2.5 and have been selected as examples to explain why piezoelectricity and pyroelectricity only occur in certain point groups.

O_h , shown in Figure 2.2, has a cubic crystal system and very high symmetry, with six 2-fold axes, four 3-fold axes, three 4-fold axes, nine planes of symmetry, and a COS. Applying pressure in any of the three crystallographic axes would still result in a symmetrical structure, and the dipoles created under pressure would cancel out symmetrically. It is therefore non-piezoelectric. Also, in its natural uncompressed state, O_h shows no net polarization and is thus non-pyroelectric.

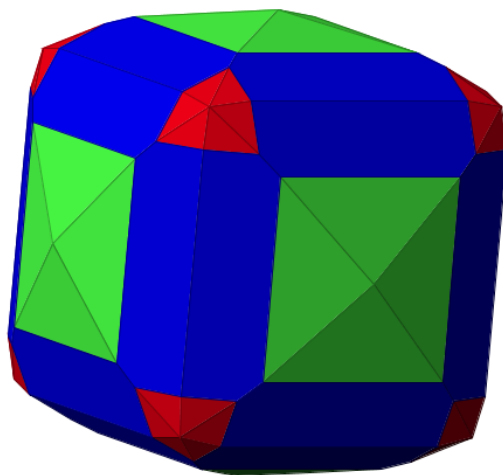


Figure 2.2. Illustration of the O_h symmetry point group.

O , shown in Figure 2.3, also has a cubic crystal system and very high symmetry with six 2-fold axes, four 3-fold axes, and three 4-fold axes of symmetry; however, it does not have a COS because not all equivalent atoms appear equidistant on all axis of symmetry. Even though it lacks a COS, it is non-piezoelectric due to its high symmetry that prevents a net polarization. Finally, in its natural uncompressed state, O shows no net polarization, thus it is non-pyroelectric.

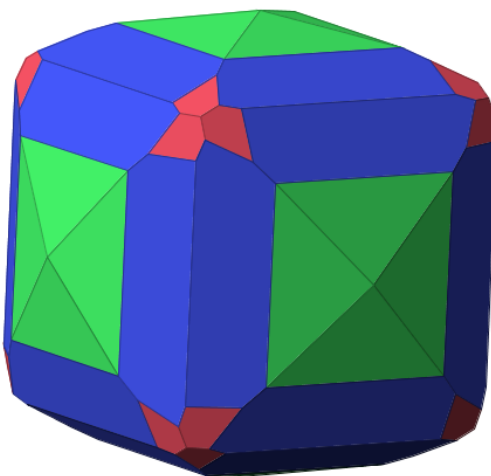


Figure 2.3. Illustration of the O symmetry point group.

T_d , shown in Figure 2.4, also has a cubic crystal system, but it has much lower symmetry than O_h or O with only three 2-fold axes and four 3-fold axes. As such, T_d is piezoelectric even though it is cubic. The symmetry is still too high to allow for pyroelectricity, so T_d is non-pyro-electric.

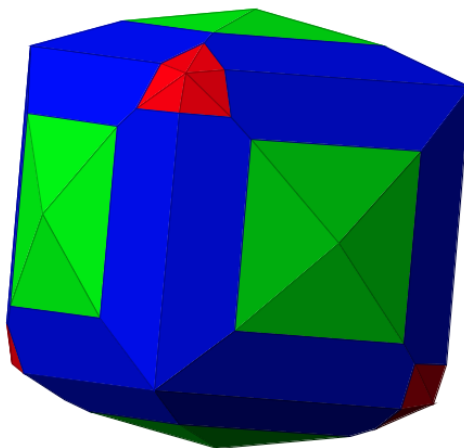


Figure 2.4. Illustration of the T_d symmetry point group.

Finally, C_{2v} , shown in Figure 2.5, has an orthorhombic crystal system and very low symmetry, with only one 2-fold axis of symmetry. It is therefore piezoelectric and pyroelectric. One can easily see that in its natural uncompressed state, the structure is partially asymmetric and a net polarization exists.

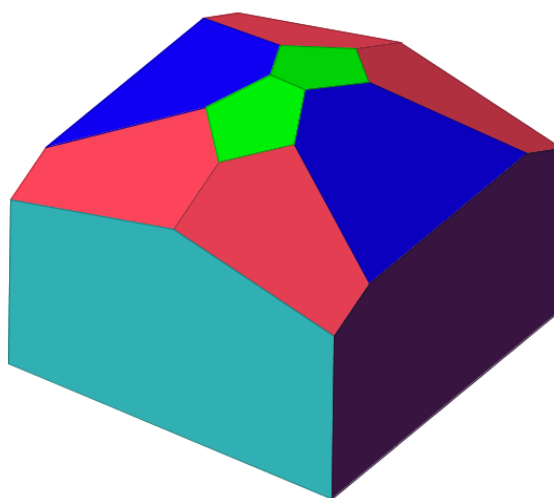


Figure 2.5. Illustration of the C_{2v} symmetry point group.

2.3 Symmetry Change as a Function of Temperature

For any given material, the symmetry point group and the crystal system can change as a function of temperature, amongst other factors. A material's thermal energy can force a restructuration of the atoms in the crystal structure in order to adopt a state of minimum energy. For example, a material can have symmetry point group $C1$ at room temperature, which is piezoelectric, but adopt point group Ci at higher temperatures, which is non-piezoelectric. The Curie temperature (T_c) is defined as the specific temperature at which the point group of a material becomes symmetrical or non-piezoelectric. Figures 2.6 and 2.7 represent the atomic structures of $BaTiO_3$ below T_c and above T_c respectively, obtained through X-ray diffraction [42]. T_c for $BaTiO_3$ is 130°C , so at 30°C it is piezoelectric, and at 200°C it is non-piezoelectric.

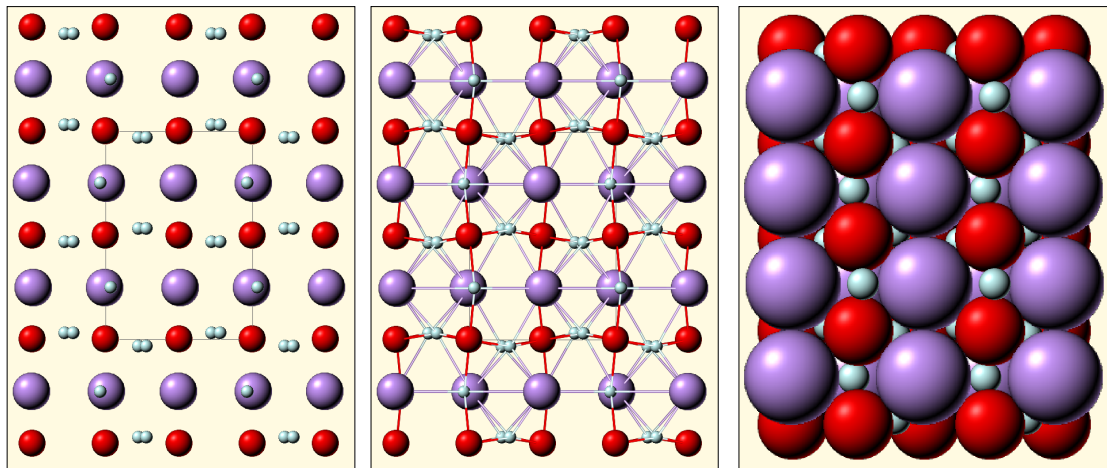


Figure 2.6. Atomic structure of $BaTiO_3$ at 30°C (below T_c). The large atoms are Ba ($r = 215$ pm), medium Ti ($r = 140$ pm), small O ($r = 60$ pm) [42].

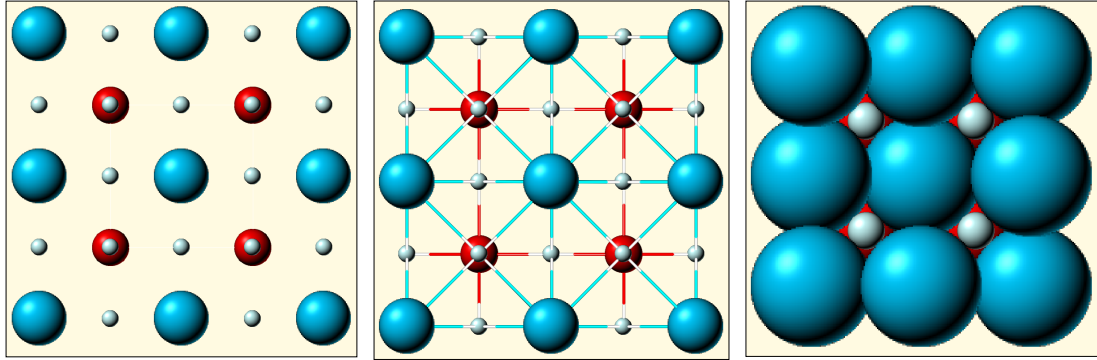


Figure 2.7. Atomic structure of BaTiO_3 at 200°C (above T_c). The large atoms are Ba ($r = 215$ pm), medium Ti ($r = 140$ pm), small O ($r = 60$ pm) [42].

Figure 2.6 reveals that BaTiO_3 at 30°C has a tetragonal structure with symmetry point group D_4 , which is piezoelectric in accordance with Table 2.1. It can be seen that the oxygen atoms are not distributed symmetrically in the crystal, so applying pressure on the crystal would generate a net dipole. However, when BaTiO_3 is heated up, the thermal energy enables the atoms to adopt a structure with higher symmetry. At 200°C , BaTiO_3 has a cubic structure with point group O_h , which is non-piezoelectric. Conversely, BaTiO_3 undergoes other phase transitions to lower symmetry point groups at lower temperatures. Around 5°C , BaTiO_3 becomes orthorhombic with point group C_{2v} and a spontaneous polarization develops along the $[101]$ direction with 12 possible dipole directions. Below -90°C , BaTiO_3 becomes rhombohedral with point group C_{3v} and the spontaneous polarization is along the $[111]$ directions with 8 possible polar directions [43].

2.4 Linear Piezoelectric Equations

Linear piezoelectric equations have been derived from the theory of thermodynamics. Starting with the Gibbs thermodynamics potential, Mason [41] proved that the electric displacement D_m and the strain S_i could be described by:

$$D_m = \varepsilon_{mk}^T E_k + d_{mi} T_i \quad (2.1)$$

$$S_i = d_{mi} E_m + s_{ij}^E T_j \quad (2.2)$$

where ε is the dielectric permittivity, E is the electric field, d is the piezoelectric coefficient, T is the stress, and s is the elastic compliance. The subscripts $i, j = 1 \dots 6$ and $k, m = 1 \dots 3$ indicate the direction, and the superscripts E and T refer to the parameter that is held constant. Many assumptions are made in order to obtain equations 2.1 and 2.2. First, the stress and the electric field must be relatively small, otherwise the thermodynamic equations become non-linear. Second, the effects of the magnetic field are ignored considering the non-magnetic nature of piezoelectric materials. Third, heating is neglected since vibrating piezoelectric ceramics generally release minimal heat at low electric field and low frequencies. Finally, if the stress is set to zero, which means that the sample is free to expand and is unclamped, equations 2.1 and 2.2 are no longer coupled, and the strain and the electric displacement can be determined as a function of the electric field exclusively.

Equations 2.1 and 2.2 can be written in the complete matrix form as follows:

$$\begin{bmatrix} S_1 \\ S_2 \\ S_3 \\ S_4 \\ S_5 \\ S_6 \\ D_1 \\ D_2 \\ D_3 \end{bmatrix} = \begin{bmatrix} s_{11}^E & s_{12}^E & s_{13}^E & s_{14}^E & s_{15}^E & s_{16}^E & d_{11} & d_{21} & d_{31} \\ s_{21}^E & s_{22}^E & s_{23}^E & s_{24}^E & s_{25}^E & s_{26}^E & d_{12} & d_{22} & d_{32} \\ s_{31}^E & s_{32}^E & s_{33}^E & s_{34}^E & s_{35}^E & s_{36}^E & d_{13} & d_{23} & d_{33} \\ s_{41}^E & s_{42}^E & s_{43}^E & s_{44}^E & s_{45}^E & s_{46}^E & d_{14} & d_{24} & d_{34} \\ s_{51}^E & s_{52}^E & s_{53}^E & s_{54}^E & s_{55}^E & s_{56}^E & d_{15} & d_{25} & d_{35} \\ s_{61}^E & s_{62}^E & s_{63}^E & s_{64}^E & s_{65}^E & s_{66}^E & d_{16} & d_{26} & d_{36} \\ d_{11} & d_{12} & d_{13} & d_{14} & d_{15} & d_{16} & \varepsilon_{11}^T & \varepsilon_{12}^T & \varepsilon_{13}^T \\ d_{21} & d_{22} & d_{23} & d_{24} & d_{25} & d_{26} & \varepsilon_{21}^T & \varepsilon_{22}^T & \varepsilon_{23}^T \\ d_{31} & d_{32} & d_{33} & d_{34} & d_{35} & d_{36} & \varepsilon_{31}^T & \varepsilon_{32}^T & \varepsilon_{33}^T \end{bmatrix} \begin{bmatrix} T_1 \\ T_2 \\ T_3 \\ T_4 \\ T_5 \\ T_6 \\ E_1 \\ E_2 \\ E_3 \end{bmatrix} \quad (2.3)$$

This matrix can be simplified as a result of symmetry. For example, the matrix for a material with symmetry group point $C6v$ [44] becomes:

$$\begin{bmatrix} S_1 \\ S_2 \\ S_3 \\ S_4 \\ S_5 \\ S_6 \\ D_1 \\ D_2 \\ D_3 \end{bmatrix} = \begin{bmatrix} s_{11}^E & s_{12}^E & s_{13}^E & 0 & 0 & 0 & 0 & 0 & d_{31} \\ s_{21}^E & s_{22}^E & s_{23}^E & 0 & 0 & 0 & 0 & 0 & d_{31} \\ s_{31}^E & s_{32}^E & s_{33}^E & 0 & 0 & 0 & 0 & 0 & d_{33} \\ 0 & 0 & 0 & s_{55}^E & 0 & 0 & 0 & d_{15} & 0 \\ 0 & 0 & 0 & 0 & s_{55}^E & 0 & d_{15} & 0 & 0 \\ 0 & 0 & 0 & 0 & 0 & 2(s_{11}^E - s_{12}^E) & 0 & 0 & 0 \\ 0 & 0 & 0 & 0 & d_{15} & 0 & \varepsilon_{11}^T & 0 & 0 \\ 0 & 0 & 0 & d_{15} & 0 & 0 & 0 & \varepsilon_{11}^T & 0 \\ d_{31} & d_{31} & d_{33} & 0 & 0 & 0 & 0 & 0 & \varepsilon_{33}^T \end{bmatrix} \begin{bmatrix} T_1 \\ T_2 \\ T_3 \\ T_4 \\ T_5 \\ T_6 \\ E_1 \\ E_2 \\ E_3 \end{bmatrix} \quad (2.4)$$

This matrix describes the relationships between the 10 coefficients characterizing piezoelectric ceramics and can theoretically predict the exact response of a material. Experimentally, however, most materials experience dispersion, non-linearity, and losses. The losses can be accounted for using the imaginary parts of the material coefficients.

2.5 Domains

A domain is defined as a macroscopic region where all of the dipoles are aligned in the same direction. The creation of domains in crystal growth is necessary in order to reduce the electrostatic energy of the system. Domains are relatively small regions, just a few lattice cells wide, but they can be observed with a scanning electron microscope (SEM) if a sample is prepared carefully. Figure 2.8 presents a SEM picture of a BaTiO_3 sample that has been grinded, polished, thinned, chemically etched and carbon coated.

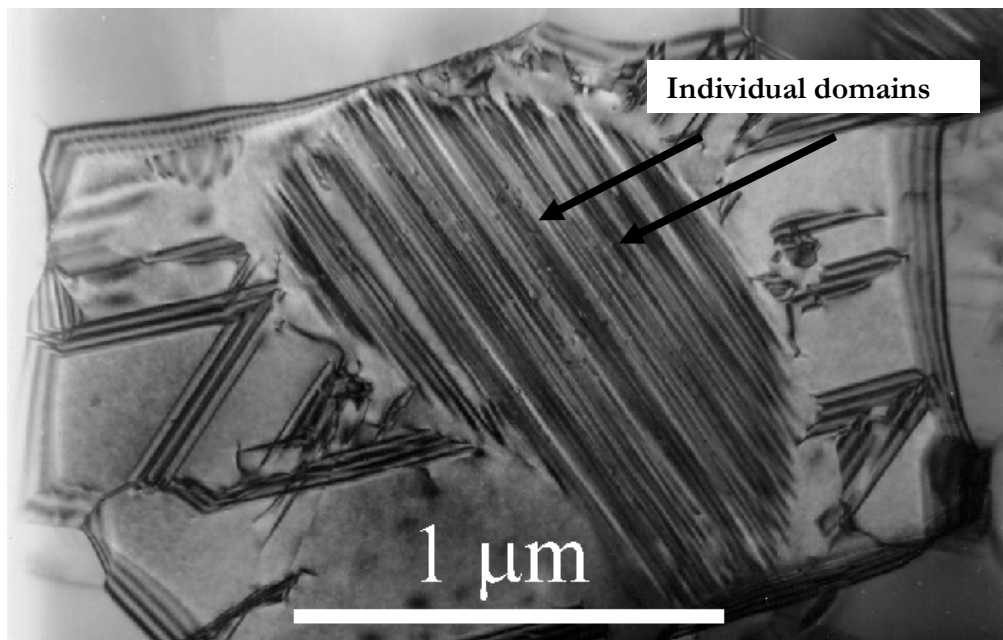


Figure 2.8. SEM picture of BaTiO_3 showing individual domains [45].

A schematic representation of domains is given in Figure 2.9.

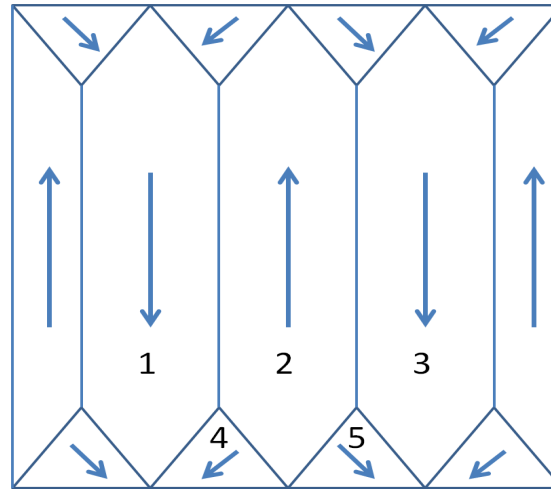


Figure 2.9. Schematic representation of domains.

Figure 2.8 and 2.9 show that domains are separated by domain walls, which are the boundaries where the dipole orientation suddenly changes. Depending on the *lattice system*, not to be confused with *crystal system*, domain walls meet at different angles. Figure 2.9 represents a rhombohedral lattice system with 180° , 109° , and 71° domain walls. For example, regions 1 and 2 have 180° domain walls, which mean that their dipoles point exactly in opposite directions. Regions 1 and 4 have 71° walls, and regions 2 and 4 have 109° walls.

Figure 2.10 a) and b) show regions 1, 2 and 4 in greater detail. Figure 2.10 a) illustrates that the 180° domain wall between regions 1 and 2 allows the domains to grow freely under the application of an electric field, directly contributing to the piezoelectric effect. However, Figure 2.10 b) reveals that a non- 180° domain wall motion creates interference in the growth of domains, and applying an electric field in one direction might force movement in another domain. This non-direct contribution to piezoelectricity is called

“extrinsic” contribution, as opposed to the “intrinsic” contribution that comes from the direct elongation of the dipoles presented in Figure 2.10 a). Studies have demonstrated that the extrinsic effect contributes to 60%-70% of the piezoelectric effect in PZT ceramics [46] [47], and it is not accounted for by the linear piezoelectric equations presented previously.

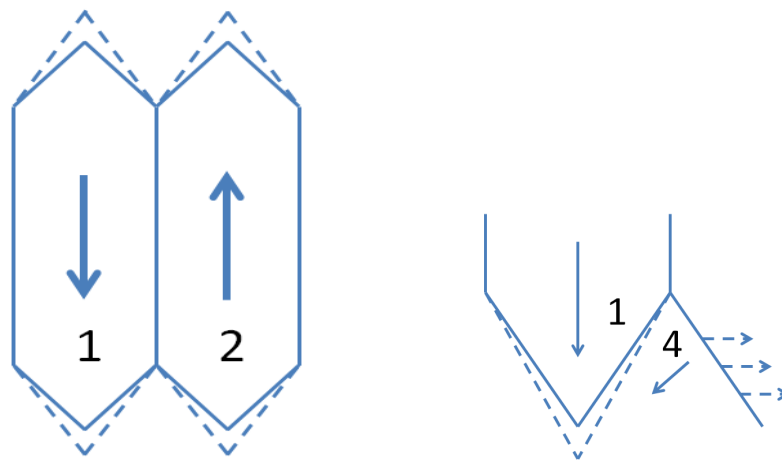


Figure 2.10. a) 180° domain wall motion. b) Non- 180° domain wall motion

Domains are not always pictured as in Figure 2.9. They can have different shapes, sizes, orientations, and random alignments. This macroscopic randomness makes the linear piezoelectric equations even less adequate to describe the behavior of piezoelectric materials, and experimental measurements become an essential part of the manufacturing process. Models have been developed in an effort to predict the contribution of domain wall motion to piezoelectricity, but such models are still incomplete and more research needs to be completed in this field [48] [49] [50].

2.6 Polarization

Piezoelectric materials experience two different types of polarization: atomic polarization and domain polarization. Atomic polarization occurs very quickly, whereas domain polarization occurs over a longer time period. Atomic polarization accounts for the intrinsic piezoelectric effect, and it is caused by the relative displacement of specific atoms in the crystal structure when subjected to a stress or an electric field. Domain polarization, on the other hand, occurs at the macroscopic level and only occurs when sufficient energy is provided to permit a domain reorientation.

A piezoelectric ceramic must undergo “poling”, as illustrated in Figure 2.11, in order to exhibit piezoelectricity, because applying stress on an unpoled ceramic would not create a net dipole moment. In the absence of an electric field, the domains in an unpoled piezoelectric material are aligned in random directions. However, if a material is heated and placed under a high electric field, all the domain dipoles align. When the material returns to room temperature, it maintains domain orientation and can subsequently exhibit piezoelectricity.

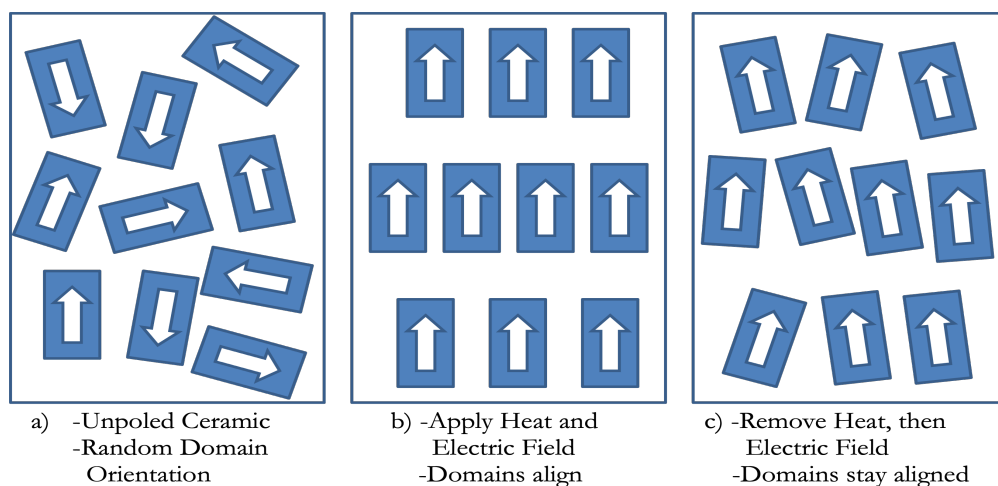


Figure 2.11. Poling of a piezoelectric ceramic.

2.7 Doping

In order to meet specific application requirements, piezoelectric ceramics can be modified by doping them with ions that have a valence different than the ions in the crystal [51]. Certain PZT ceramics can be doped with ions to form "hard" and "soft" PZT's. Hard PZT's are doped with acceptor ions such as K^+ , Na^+ to replace the Pb^{2+} ions, and Fe^{3+} , Al^{3+} , Mn^{3+} to replace the Zr^{4+} or Ti^{4+} ions, creating oxygen vacancies in the lattice in order to maintain electroneutrality [52]. Hard PZT's usually have lower permittivities, smaller electrical losses and lower piezoelectric coefficients. They are more difficult to pole and unpole, making them ideal for applications in extreme environments. On the other hand, soft PZT's are doped with donor ions such as La^{3+} to replace the Pb^{2+} ions and Nb^{5+} , Sb^{5+} to replace Zr^{4+} or Ti^{4+} ions, leading to the creation of Pb^{2+} vacancies in the lattice, once again in order to maintain electroneutrality. The soft PZT's have a higher permittivity, larger losses, higher piezoelectric coefficient and are easier to pole and unpole. They can be used for applications requiring high piezoelectric coefficients.

In soft doping, a lattice with Pb vacancies can transfer atoms more easily [53]; thus, domain motions are encouraged and piezoelectric properties are enhanced. Describing the physical mechanisms in hard doping are more complex, because the ions are sometimes replaced by larger ions and sometimes by smaller ions. However, it has been proven experimentally [53] that hard doping dramatically increases space charges, which causes an internal electric field inside the grains of PZT that inhibit domain motion.

2.8 Grain Structure of Ceramics

Domains are generally only a few lattice cells wide and are difficult to observe under SEM, but grains are larger structures that can easily be observed under SEM. The grain structure of three different piezoelectric ceramics: EC-65, EC-69, and EC-76 were obtained using a Philips XL-30 Scanning Electron Microscope and are shown in Figures 2.12 to 2.17. Prior to capturing these images, the samples were wet-polished with aluminum oxide and coated with gold.

A qualitative evaluation of Figures 2.12 to 2.17 reveals that EC-65 has medium grain size and medium porosity, EC-69 has the smallest grain size and is the most porous, and EC-76 has the largest grain size and is the least porous. EC-69, having the smallest grain size and highest porosity, has the smallest relative dielectric permittivity, coupling factor, and piezoelectric coefficient. EC-76, with large grains and low porosity, has the highest relative dielectric coefficient, coupling factor, and piezoelectric coefficient. EC-65 has a medium mechanical quality factor, medium relative dielectric coefficient, medium coupling factor and medium piezoelectric coefficient. This demonstrates that the more compact and the least porous a piezoelectric ceramic is, the stronger the piezoelectric response. The manufacturer's data for EC-65, EC-69, and EC-76 is presented in table 2.2.

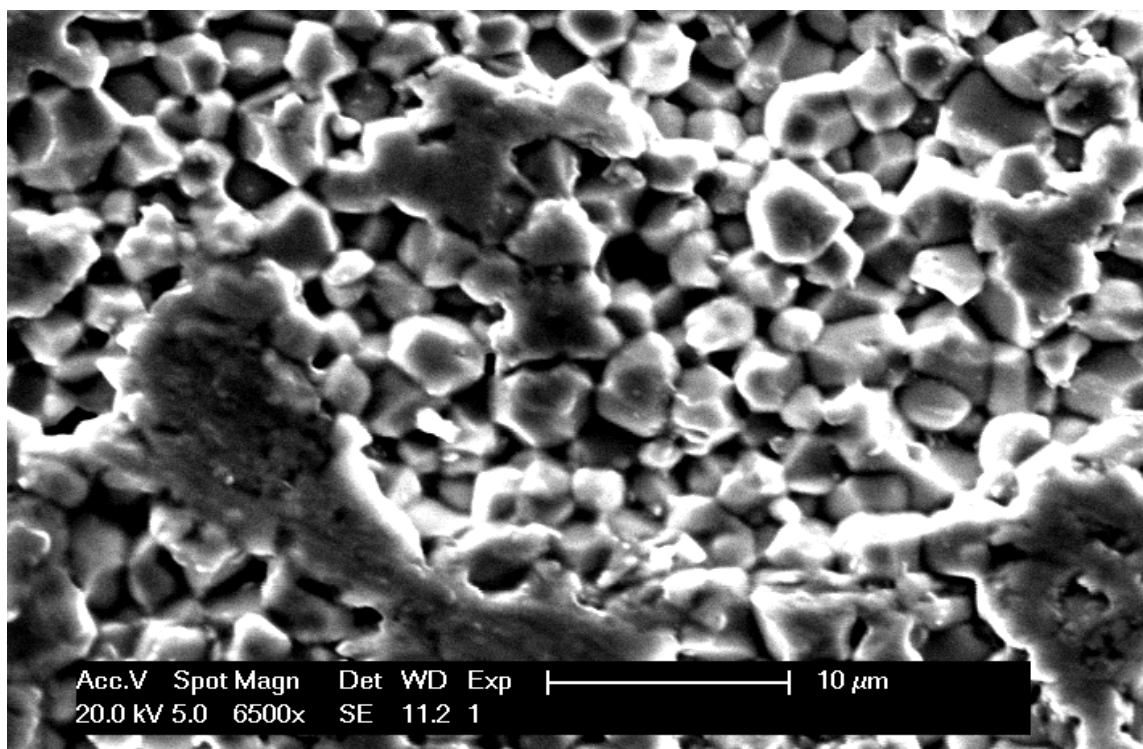


Figure 2.12. SEM picture of EC-65 at magnification 6500 \times .

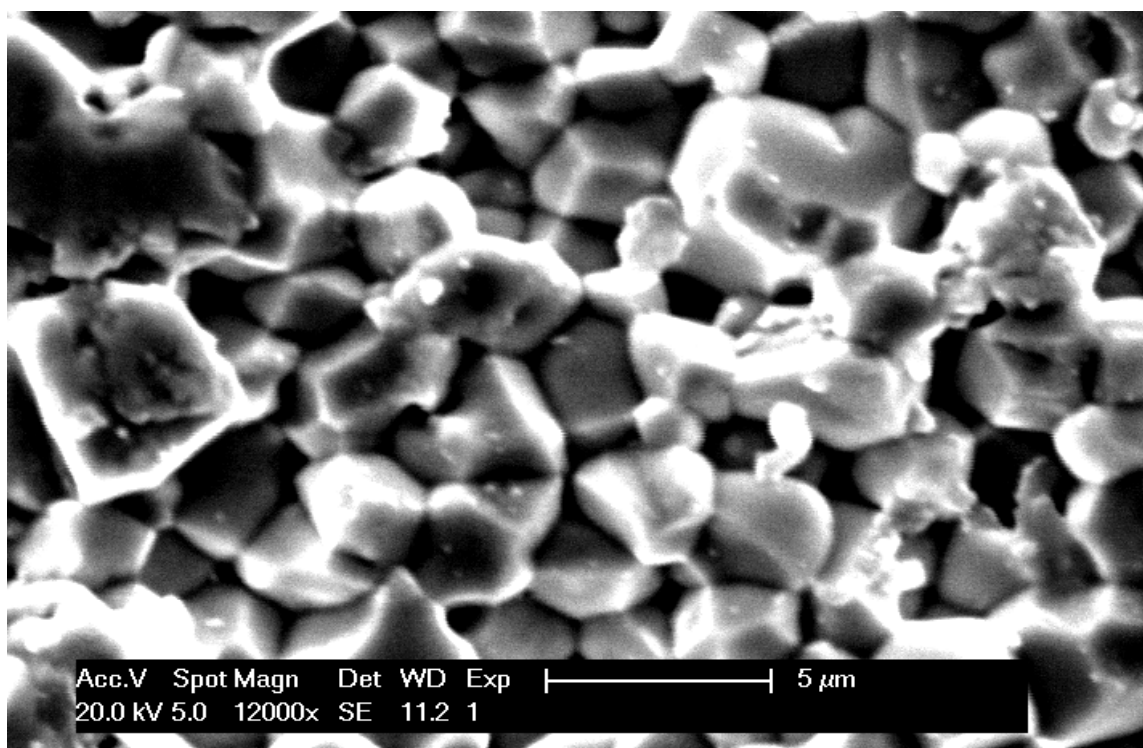


Figure 2.13. SEM picture of EC-65 at magnification 12000 \times .

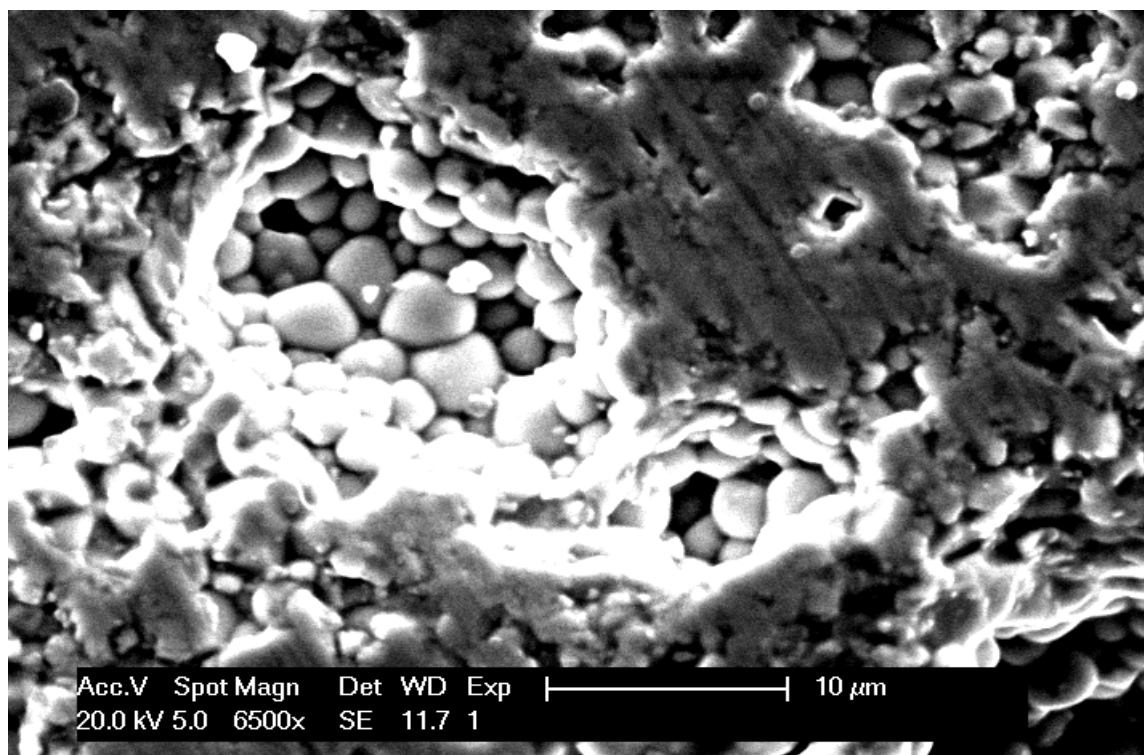


Figure 2.14. SEM picture of EC-69 at magnification 6500 \times .

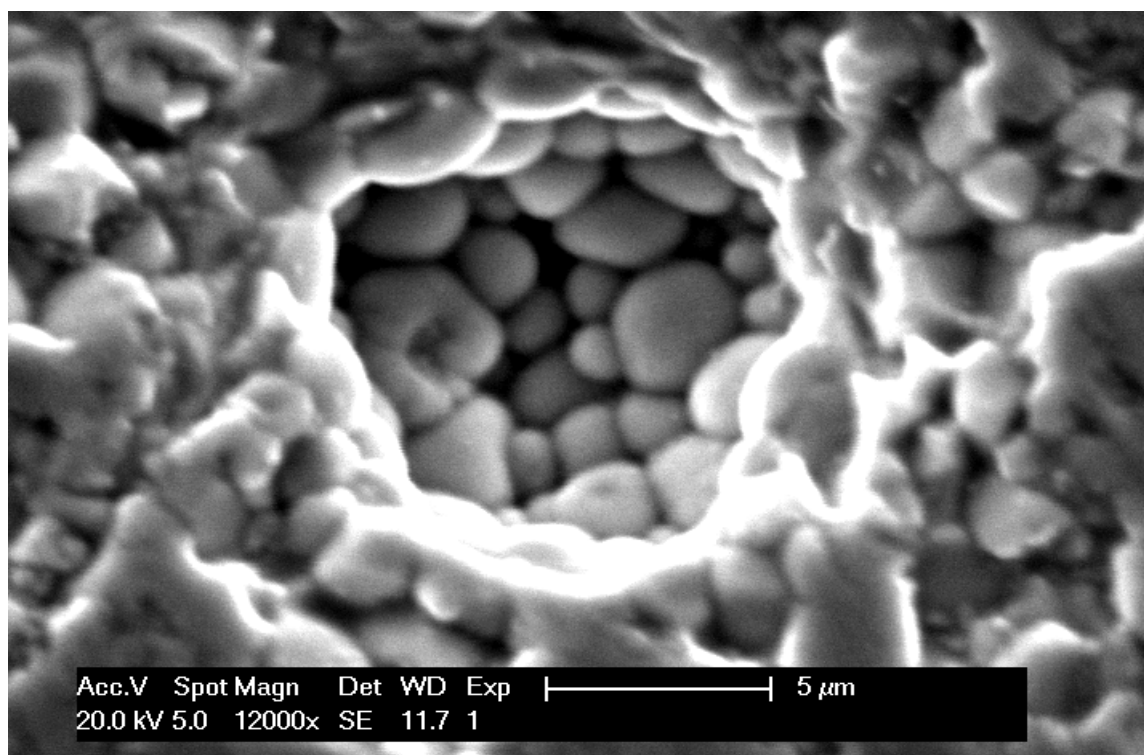


Figure 2.15. SEM picture of EC-69 at magnification 12000 \times .

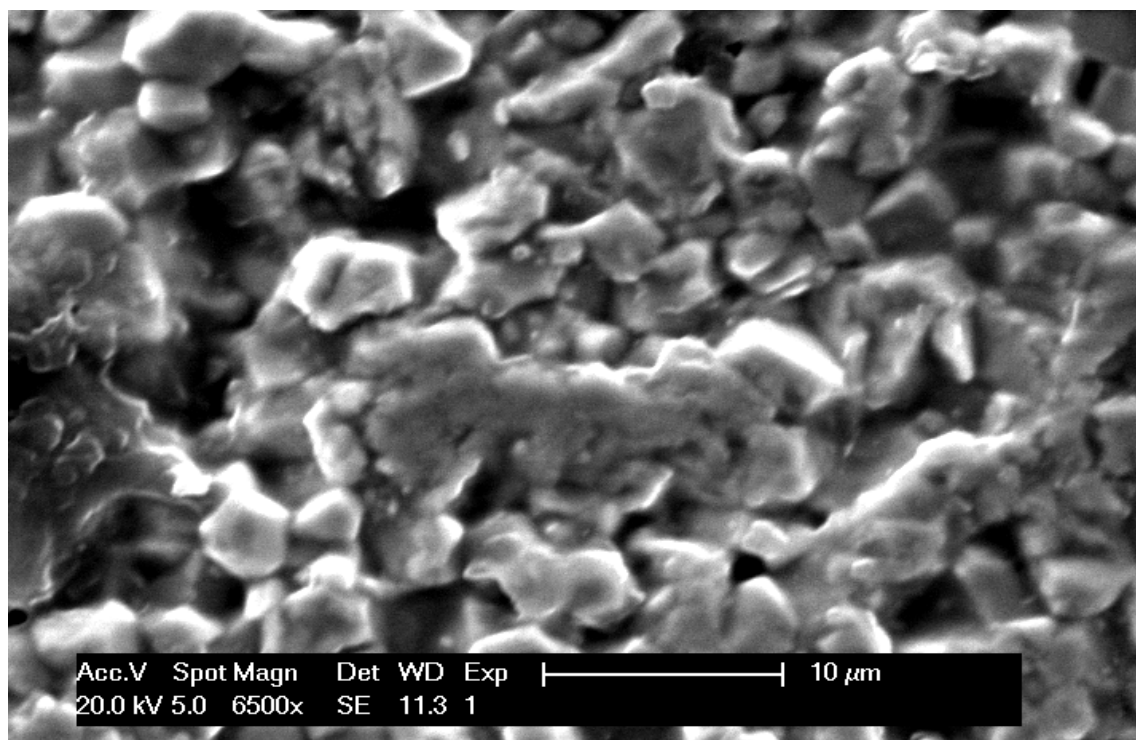


Figure 2.16. SEM picture of EC-76 at magnification 6500 \times .

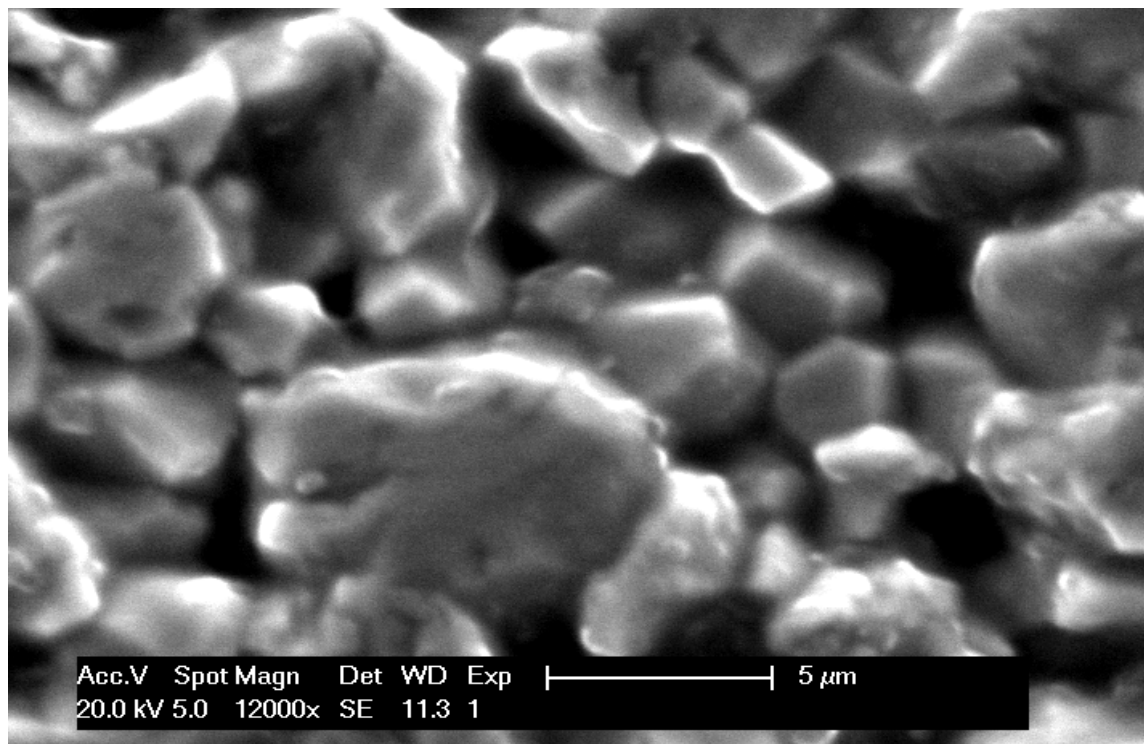


Figure 2.17. SEM picture of EC-76 at magnification 12000 \times .

Table 2.2. Physical properties of EC-65, EC-69, and EC-76 published by EDO Ceramic [54].
 Note: The values are nominal; actual samples may vary by $\pm 10\%$.

Property	EC-65 (soft)	EC-69 (hard)	EC-76 (soft)
Density ($\times 10^3$ Kg/m ³)	7.5	7.5	7.45
Young's Modulus ($\times 10^{10}$ N/m ²)	6.6	9.9	6.4
Mechanical Factor Q	100	960	65
Relative Dielectric Permittivity K_{33}^T	1725	1050	3450
Coupling Factor k_{33} (no units)	0.72	0.62	0.75
Piezoelectric Coefficient d_{33} ($\times 10^{-12}$ C/N)	380	220	583

2.9 Phase Diagrams

Chapter 2.7 described how the exact chemical composition of a ceramic has a major impact on its physical and electromechanical properties. The phase diagrams of different piezoelectric ceramics have been developed in order to understand the effect of composition on piezoelectricity, and also to identify the optimal chemical compositions for different applications. A well known phase diagram for PZT was developed by Jaffe in 1971 and is presented in Figure 2.18.

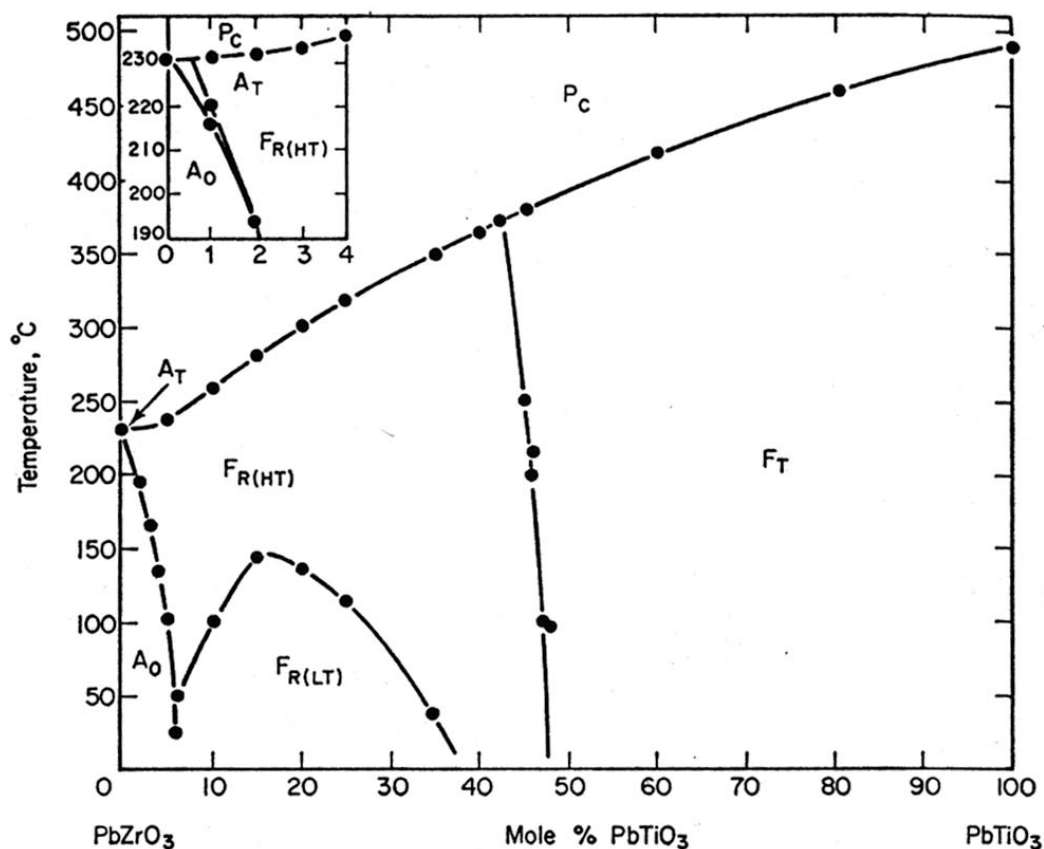


Figure 2.18. PZT phase diagram by Jaffe [55]. The regions in this diagram are: P_C=Paraelectric Cubic (P_C); F_T=Ferroelectric Tetragonal; F_{R(HT)}=Ferroelectric Rhombohedral High Temperature; F_{R(LT)}=Ferroelectric Rhombohedral Low Temperature; A_O=Antiferroelectric Orthorombic; and A_T=Antiferroelectric Tetragonal.

Figure 2.18 illustrates that PZT has a paraelectric cubic structure at high temperatures, which is consistent with the theory outlined in Chapter 2.3. Below T_c , the structure is either tetragonal or rhombohedral, depending on the exact PZT composition. PbZrO₃ alone is antiferroelectric, so it is not surprising to observe antiferroelectric phases at low concentrations of PbTiO₃.

A special region called the “Morphotropic Phase Boundary” (MPB) [56] has been found to exist between the tetragonal phase and the orthorhombic phase at a ratio of approximately $Zr/Ti \sim 52/48$. The dielectric permittivity, piezoelectric coefficients and electromechanical coupling coefficients are very high for compositions closest to the MPB. Prior to 1999, the MPB was believed to separate the ferroelectric tetragonal and rhombohedral phases with the coexistence of these two phases in that region. This explained the excellent piezoelectric response because the spontaneous polarization within each domain could be switched to one of the 14 possible orientations consisting of eight [111] directions for the rhombohedral phase and six [100] directions for the tetragonal phase.

In the last decade, several new monoclinic phases have been discovered in the MPB region including: Cm [57] [58] [59], Cc [60] [61], and Pm [62] [63]. Recent experiments have not only confirmed the presence of the monoclinic phases, but have also shown that they are responsible for the maximum electromechanical response [64]. A unique feature of the structure of the monoclinic crystal system is that the polarization vectors can lie anywhere in a symmetry plane, in contrast to the tetragonal and rhombohedral system where the polarization vectors can lie only along the crystallographic directions [001] and [111]. The polarization vectors of the monoclinic phase can therefore adjust themselves easily to the external electric field direction and lead to a larger electromechanical response [56]. These new findings also suggest that the rhombohedral phases discovered by Jaffe were in fact not rhombohedral, but rather monoclinic, as illustrated in Figure 2.19.

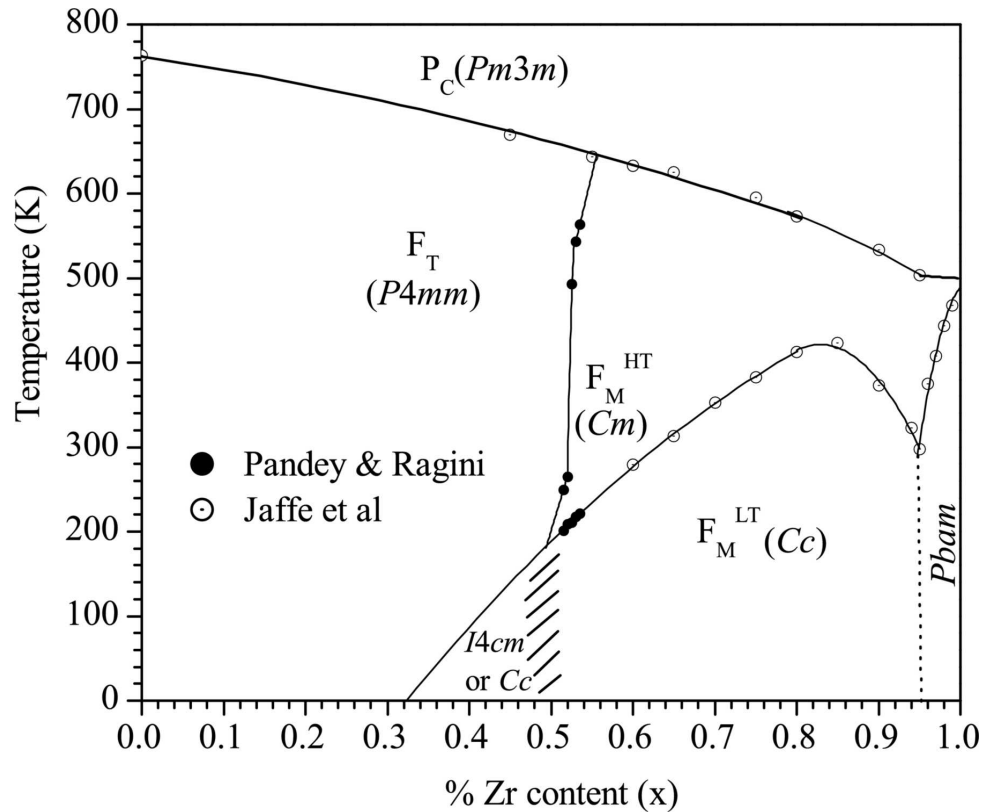


Figure 2.19. New PZT phase diagram by Pandey & Ragini, 2008 [56]. The different regions in the diagram are identified as:

$Pm3m$ → space group #221 → point group Oh → crystal system cubic → paraelectric;
 $P4mm$ → space group #99 → point group $C4v$ → crystal system tetragonal → ferroelectric;
 Cm → space group #8 → point group Cs → crystal system monoclinic → ferroelectric;
 Cc → space group #9 → point group Cs → crystal system monoclinic → ferroelectric;
 $I4cm$ → space group #108 → point group $C4v$ → crystal system tetragonal → ferroelectric;
 $Pbam$ → space group #55 → point group $D2h$ → crystal system orthorhombic → antiferroelectric.

Two important differences can be observed between Figure 2.18 and 2.19. First, Figure 2.19 offers phase information below 0°C, which is very valuable because many piezoelectric materials need to operate under this temperature. Second, Figure 2.19 uses the space groups instead of the crystal systems. Space groups are sub-categories of symmetry point groups and are therefore much more relevant than crystal systems for defining piezoelectricity, as detailed in Chapter 2.2.

Haertling established the phase diagram of PLZT in 1987, and his results are presented in Figure 2.20. Similar to the PZT phase diagram established by Jaffe, Haertling found that PLZT had an antiferroelectric phase at low concentration of PbTiO_3 , which is expected since PbZrO_3 alone is antiferroelectric. Also, Haertling found that PLZT had a tetragonal phase at high concentration of PbTiO_3 and a rhombohedral phase at low concentrations of PbTiO_3 , just like PZT, except that the phases are highly dependent on the concentration of lanthanum. Unfortunately, Haertling's PLZT phase diagram suffers from the same deficiencies as Jaffe's PZT phase diagram, especially in the "slim ferroelectric region" (SFE), which is not well understood. A new phase diagram based on space groups or point groups would provide valuable insight on the properties of PLZT.

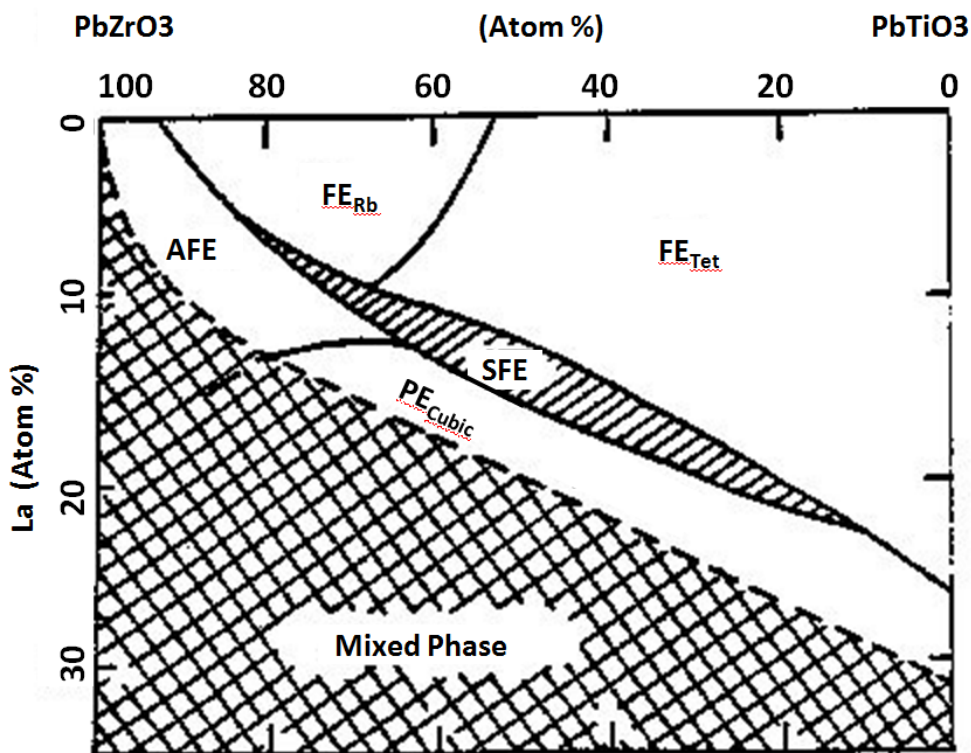


Figure 2.20. Haertling's phase diagram for PLZT. The regions in this diagram are: FE_{Rb} =Ferroelectric Rhombohedral; FE_{Tet} =Ferroelectric Tetragonal; PE_{Cubic} =Paraelectric Cubic; SFE=Slim Ferroelectric; and AFE=Antiferroelectric [65].

2.10 X-ray Diffraction

2.10.1 Theory

X-ray diffraction (XRD) is the main method used to obtain the crystal structure, lattice parameters, and phase diagrams of piezoelectric materials. When an X-ray beam is incident upon a sample, some X-rays are transmitted through the sample, and some X-rays are scattered by the atoms in the material. Interference peaks are created from the scattered X-rays, and those peaks have a specific width, position, and intensity. It is possible to predict the position of the peaks using Bragg's law:

$$n\lambda = 2d\sin\theta \quad (2.3)$$

where n is an integer, λ is the wavelength of incident wave, d is the spacing between the planes in the atomic lattice, and θ is the angle between the incident ray and the scattering planes. The spacing d can be calculated directly from the Miller indices (h, k, l), the values of the unit cell axes (a, b, c), and the unit cell angles (α, β, γ), as presented in Table 2.3:

Table 2.3. Interlattice spacing as a function of Miller indices and unit cell parameters [66].

Orthorhombic	Tetragonal	Cubic
$\frac{1}{d_{hkl}^2} = \frac{h^2}{a^2} + \frac{k^2}{b^2} + \frac{l^2}{c^2}$	$\frac{1}{d_{hkl}^2} = \left[h^2 + k^2 + l^2 \left(\frac{a}{c} \right)^2 \right] \frac{1}{a^2}$	$\frac{1}{d_{hkl}^2} = (h^2 + k^2 + l^2) \frac{1}{a^2}$
Monoclinic		Hexagonal
$\frac{1}{d_{hkl}^2} = \frac{h^2}{a^2 \sin^2 \gamma} + \frac{k^2}{b^2 \sin^2 \gamma} - \frac{2hk \cos \gamma}{ab \sin^2 \gamma} + \frac{l^2}{c^2}$		$\frac{1}{d_{hkl}^2} = \left[\frac{4}{3} (h^2 + k^2 + hk) + l^2 \left(\frac{a}{c} \right)^2 \right] \frac{1}{a^2}$
Triclinic		
$\frac{1}{d_{hkl}^2} = \left[\begin{array}{c} \left \begin{array}{ccc} \frac{h}{a} & \cos \gamma \cos \beta & \\ \frac{k}{b} & 1 & \cos \alpha \\ \frac{l}{c} & \cos \alpha & 1 \end{array} \right + \frac{k}{b} \left \begin{array}{cc} 1 & \frac{h}{a} \cos \alpha \\ \cos \gamma & \frac{k}{b} \cos \alpha \end{array} \right + \frac{l}{c} \left \begin{array}{cc} 1 & \cos \gamma \frac{h}{a} \\ \cos \gamma & 1 \frac{k}{b} \end{array} \right \right] \cdot \left \begin{array}{ccc} 1 & \cos \gamma \cos \beta & \\ \cos \gamma & 1 & \cos \alpha \\ \cos \beta \cos \alpha & 1 & 1 \end{array} \right ^{-1}$		
Trigonal (rhombohedral)		
$\frac{1}{d_{hkl}^2} = \frac{[(h^2 + k^2 + l^2) \sin^2 \alpha + 2(hk + kl + lh) (\cos^2 \alpha - \cos \alpha)]}{A^2 (1 + 2 \cos^3 \alpha - 3 \cos^2 \alpha)}$		

Combining Equation 2.3 and Table 2.3, it is possible to determine the crystal system based on the position of the peaks observed. A more advanced technique, called the Rietveld analysis, can be used to determine the exact space group and point group of a material, but this technique requires advanced computer software that was not available for this research, and so only the crystal structure was studied.

2.10.2 Results and Discussion

XRD peaks were obtained for PLZT 9.5 at room temperature and are presented in Figure 2.21. The data was obtained using a Scintag X1 diffractometer, scanning from $\theta = 15^\circ$ to 90° at a rate of 1.00 deg/min, with a copper source of wavelength $K_{\alpha 1} = 1.540562 \text{ \AA}$. In Figure 2.21, the top section represents the experimental XRD peaks obtained for PLZT, the middle section represents the theoretical peaks for a cubic crystal structure, and the lower section represents the theoretical peaks for a tetragonal crystal structure. Careful examination reveals that both the cubic and the tetragonal phase coexist at room temperature for this specific composition of PLZT. The peaks observed at 22° and 31° could come from the cubic or the tetragonal phase, or both. However, the peak observed at 38° must come from the cubic phase, and the peak observed at 55° must come from the tetragonal phase. The coexistence of the cubic and the tetragonal phase at room temperature agrees with the PLZT phase diagram from Haertling. According to the phase diagram, PLZT 9.5 falls between the tetragonal, rhombohedral, and slim ferroelectric regions. Therefore, it is not surprising to observe the coexistence of the tetragonal and cubic phase at room temperature. The rhombohedral phase, however, was not observed.

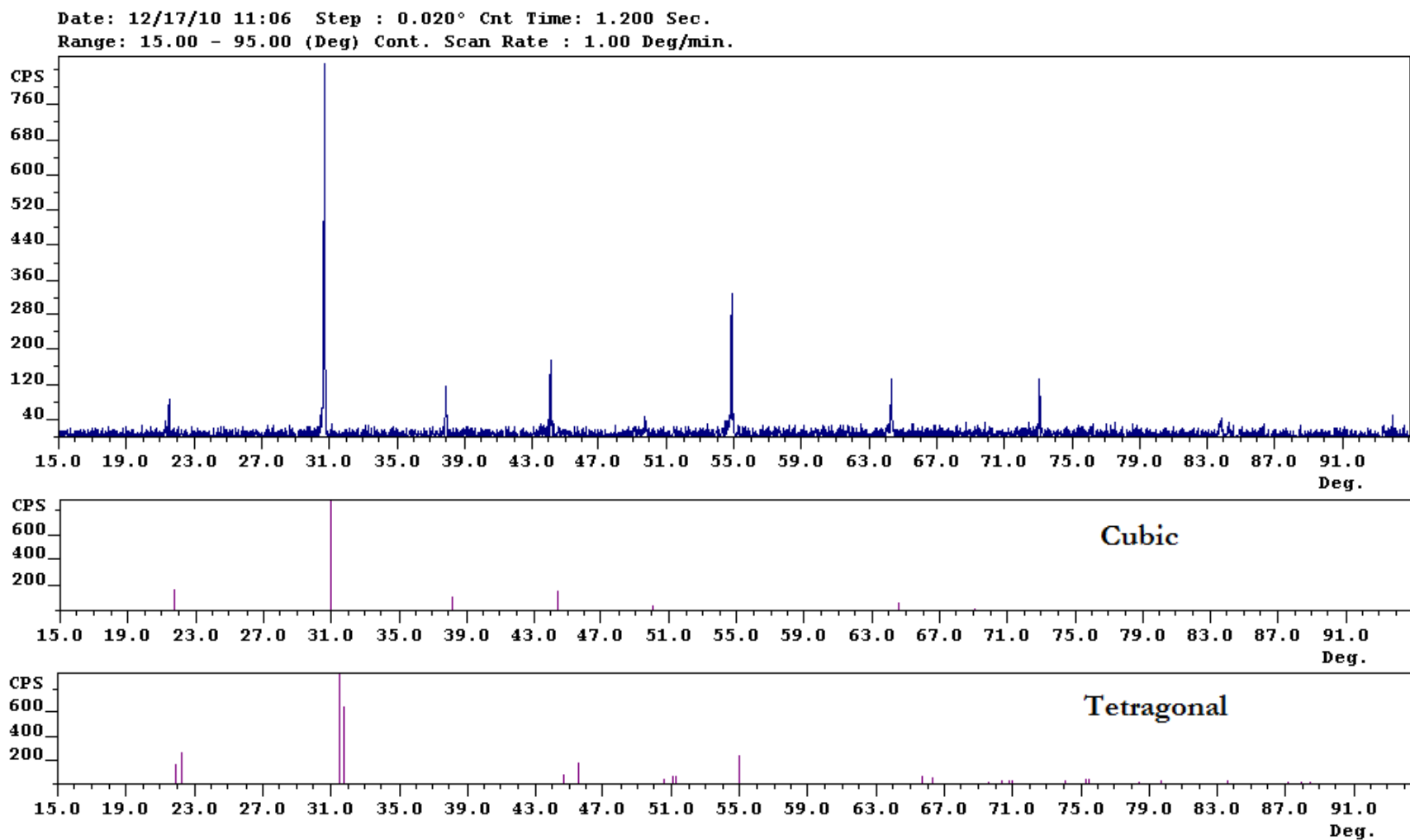


Figure 2.21. X-ray diffraction peaks for PLZT 9.5 at room temperature (20°C) with a range of $2\theta = 15^\circ$ to 90° . Note that there is an uncertainty of 1° on the peaks due to sample configuration.

Another computer software called “Scintag Lattice Refinement Program” was used to confirm the crystal symmetry. A screenshot of Scintag is given in Figure 2.22. Scintag can automatically match the XRD peaks with the Miller indexes for a certain crystal system and find the corresponding lattice parameters. If the parameters obtained have an uncertainty greater than 1% (ie. $ESD A / A > 0.01$), then it is considered that the crystal system does not match. For the PLZT sample analyzed, Scintag produced a match for both the cubic and tetragonal crystal system, which is consistent with the results presented in Figure 2.21. Figure 2.22 provides the cell parameters for the cubic structure of PLZT at room temperature: $a = b = c = 4.094172 \text{ \AA}$ and $\alpha = \beta = \gamma = 90^\circ$, as well as the Miller indices associated with each XRD peak. OBS represents the experimental position of the peaks observed, CALC represents the theoretical position of the peaks, and DELTA represents the difference in degrees between the experimental results and the theoretical peaks.

```

*****
SCINTAG/USA LATTICE REFINEMENT PROGRAM
3.00-WINNT
*****

CELL PARAMETERS:
-----
      A = 4.094172      B = 4.094172      C = 4.094172
      ESD A = .001834   ESD B = .001834   ESD C = .001834

      ALPHA = 90.000    BETA = 90.000    GAMMA = 90.000
      ESD ALPHA = .000  ESD BETA = .000  ESD GAMMA = .000

      VOLUME = 68.63

CRYSTAL SYMMETRY SYSTEM:
-----

CUBIC

      H K L      2-THETA (DEG)      D - SPACINGS      INT(CPS)
              OBS-----CALC----DELTA      OBS-----CALC----DELTA
1  0  0  21.5818  21.6886  -.1068  4.11419  4.09417  .02001  79
1  1  0  30.7768  30.8612  -.0845  2.90277  2.89502  .00775  875
1  1  1  37.9683  38.0365  -.0683  2.36786  2.36377  .00409  120
2  0  0  44.1687  44.2071  -.0384  2.04878  2.04709  .00169  199
2  1  0  49.7448  49.7570  -.0123  1.83139  1.83097  .00042  47
2  1  1  54.8856  54.8838  .0018  1.67139  1.67144  -.00005  362
2  2  0  64.3419  64.3007  .0412  1.44668  1.44751  -.00083  135
3  1  0  73.1026  73.0186  .0840  1.29341  1.29469  -.00128  136

END OF LATTICE REFINEMENT

```

Figure 2.22. “Scintag Lattice Refinement Program” for PLZT 9.5 for a cubic crystal system.

Further research needs to be completed by XRD on piezoelectric materials. The results obtained by Pandey & Ragini [56] for PZT raise interesting questions, and Haertling’s PLZT phase diagram may need to be revised in the rhombohedral and Slim Ferroelectric regions. The Rietveld analysis is the recommended method of research because it gives not only the crystal system, but also the symmetry point group and the space group. This could provide valuable information on the optimal chemical composition of materials and dopants to be used, as well as give insight towards the development of new piezoelectric materials.

CHAPTER 3 : FERROELECTRIC PROPERTIES OF PIEZOELECTRIC MATERIALS

Chapter 3 starts with a discussion on dielectrics, ferroelectricity, and ferroelectric hysteresis. Then, the experimental procedure is outlined and the experimental setup used to obtain the polarization curves is presented. Finally, the polarization curves of EC-65, PLZT 9.5, BM-941, BM-600, PMN-PT, and BM-150 are presented and analyzed.

3.1 Theory

In the previous chapter, it was explained how the macroscopic structure, including the domains and domain wall motion, leads to non-linearities. The non-linear response is difficult to predict, but it has practical advantages in multiple applications. Ferroelectricity is a direct result of those non-linearities, and it is defined as a property of certain dielectric materials to possess a spontaneous electric polarization that can be reversed by the application of an external electric field [67]. Thus, by definition, all ferroelectric materials are piezoelectric and pyroelectric, but not all piezoelectrics are ferroelectrics. The relationship between piezoelectricity, pyroelectricity, and ferroelectricity is illustrated in Figure 3.1.

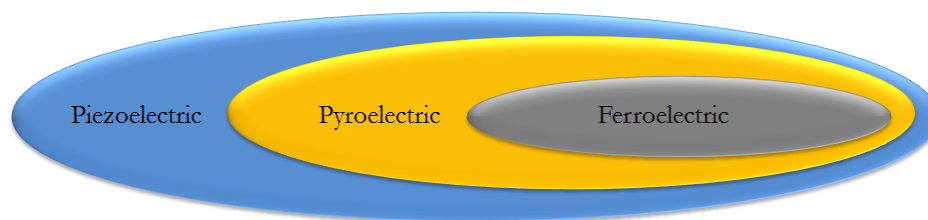


Figure 3.1. The relationship between piezoelectric, pyroelectric, and ferroelectric materials.

The polarization curves of common dielectric, paraelectric, and ferroelectric materials are depicted in Figure 3.2. Dielectric materials exhibit linear polarization as a function of the applied electric field; paraelectric materials exhibit non-linear polarization; and ferroelectric materials exhibit non-linear spontaneous polarization in the absence of an electric field [68].

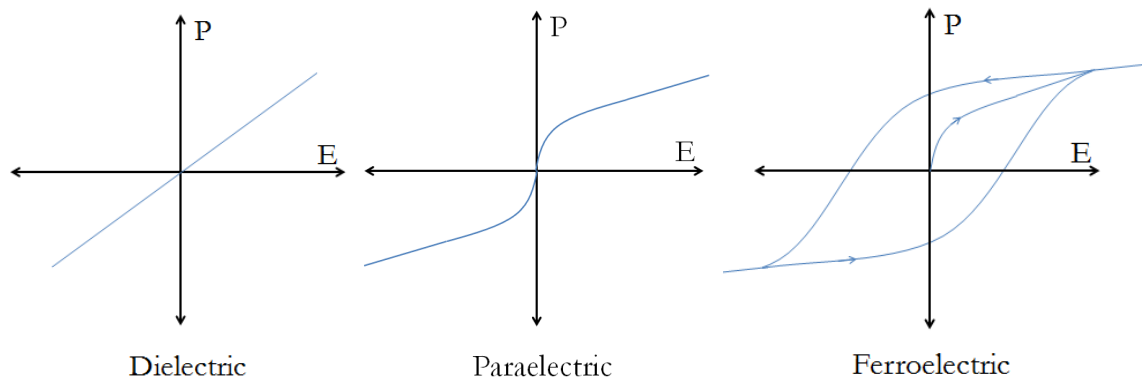


Figure 3.2. The hysteresis loop of a dielectric, a paraelectric, and a ferroelectric material.

In ferroelectric materials, the domain wall motion lags behind the electric field, a phenomenon known as hysteresis. A detailed hysteresis curve is depicted in Figure 3.3. If the material is unpoled, no net polarization can be observed, and thus the hysteresis curve begins at point #1, the origin. When an electric field is applied, the polarization increases non-linearly until the saturation state, point #2, where all the dipoles and the domains are aligned. Upon removing the electric field, polarization slowly decreases until point #3, where a remnant polarization exists as a result of domain orientation. The material is now poled and exhibits a net polarization even in the absence of an electric field. If a negative electric field is applied, the polarization continues to decrease until it becomes zero at point #4. This point represents the coercive field necessary to remove the spontaneous polarization. Upon the application of a greater negative electric field, the polarization will continue to decrease

until point #5, the “negative” saturation state, where all the dipoles and domains point in the opposite direction than they were originally pointing. Upon completely removing the electric field, a “negative” remnant polarization exists at point #6, which can be removed by applying a positive electric field. This is the basis of a simple ferroelectric hysteresis curve.

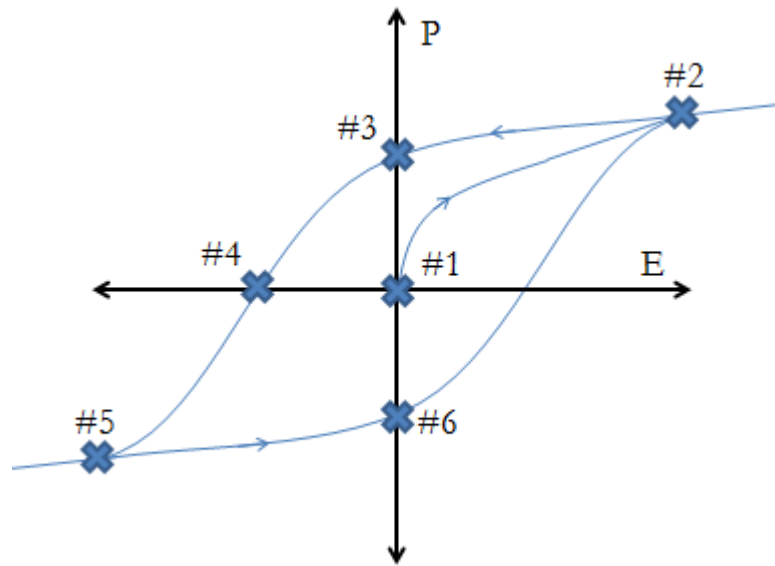


Figure 3.3. A typical hysteresis loop for a ferroelectric material.

3.2 Experimental procedure

Polarization P (C/m^2) is defined as:

$$P = \frac{\langle d \rangle}{V} \quad (3.1)$$

where $\langle d \rangle$ is the average electric dipole moment and V is the volume. The average electric dipole moment cannot be measured directly, so the electric displacement D (C/m^2) was measured instead of polarization, which can be defined as:

$$D = \frac{Q}{A} = \epsilon_0 E + P \quad (3.2)$$

where Q is the charge, A is the area, and E is the electric field. In order to determine the charge on the electrode, a capacitor was connected in series with the piezoelectric sample, which accumulated the same charge, as per Kirchhoff's circuit laws. The charge on the capacitor was calculated by measuring the voltage V across the capacitor and multiplying it by its capacitance C . This circuit is essentially a simplified Sawyer Tower circuit [69].

The circuit used to collect the data is depicted in Figure 3.4. The piezoelectric sample had to be submerged in Fisher high temperature bath oil in order to prevent short-circuits caused by the high voltages applied across the sample. The oil's freezing point was $-40^\circ C$ and its boiling point was $140^\circ C$, which limited the temperature range at which the polarization curves could be obtained. The samples were heated in the Fisher bath oil using an Omega CN2041 temperature controller and cooled using a Delta Design 9023 temperature chamber with a 9015 Controller. The voltage was generated by an Agilent 33220A function generator and amplified by a Trek 610D voltage amplifier with a gain of 1000 V/V and a current limiter of 2 mA to protect the circuit in case of a short-circuit. The voltages were measured with a National Instrument USB-6210 Data Acquisition (DAQ) board connected to a computer running LabVIEW Signal Express 2010.

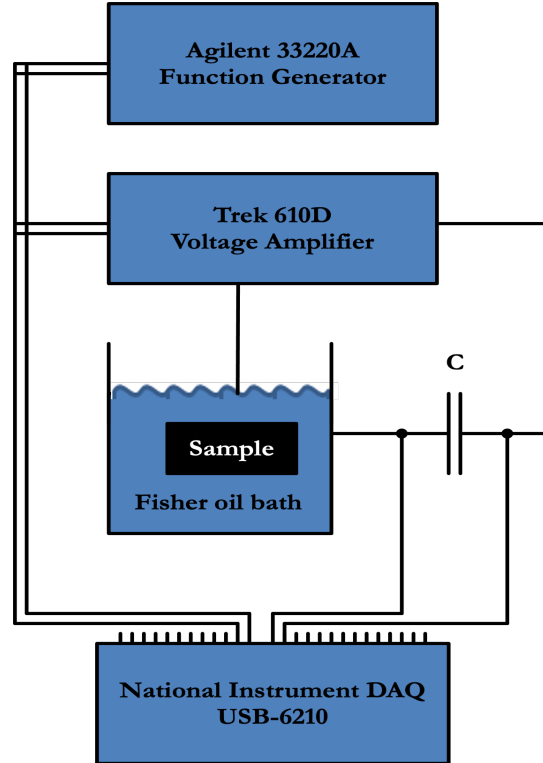


Figure 3.4. Experimental setup used to obtain the polarization curves.

Four specific parameters had to be selected carefully for each of the different polarization curves: the voltage applied, the frequency of the signal, the capacitance of the capacitor, and the sample itself.

First, the voltage applied needed to be sufficiently high to induce domain wall motion, but not so high to short-circuit the sample. If the voltage applied was too low, a linear polarization curve was obtained, which indicated that ferroelectricity did not occur and only dielectric polarization occurred. The applied voltage ranged from 500 V to 2500 V depending on the sample thickness and tendency to short-circuit.

Second, the frequency of the signal applied had to be within a specific range due to the experimental setup. If the frequency was too low, the voltage leaked through the setup and a flat version of the hysteresis curve was obtained. If the frequency was too high, the capacitor did not have the time to fully charge and the voltage measured across the capacitor became choppy, as shown in Figure 3.5 at 50 Hz. Also, since domain polarization occurs at much higher frequencies than that applied, polarization was not dependent on frequency in this experiment, as observed in Figure 3.5. The frequencies chosen to obtain the hysteresis curves ranged from 0.5 Hz to 5 Hz.

Third, the capacitance of the capacitor had to be chosen carefully. In general, the capacitance of the capacitor had to be much higher than the capacitance of the piezoelectric sample so that most of the voltage was applied across the sample and not the capacitor. However, if the capacitance was too high, the capacitor did not have the time to fully charge and, again, a choppy signal was measured. The capacitors chosen ranged from 0.5 μF to 40 μF .

Fourth, the piezoelectric samples had to be selected carefully. Ferroelectric ceramics age with time, and they tend to lose their poling and polarization properties. If the samples were too old or had never been poled, the ferroelectric effect was not observed and a linear polarization curve was obtained. Finally, if a sample had been short-circuited once, it was much more prone to short-circuiting again, so high voltages could not be applied on the sample anymore.

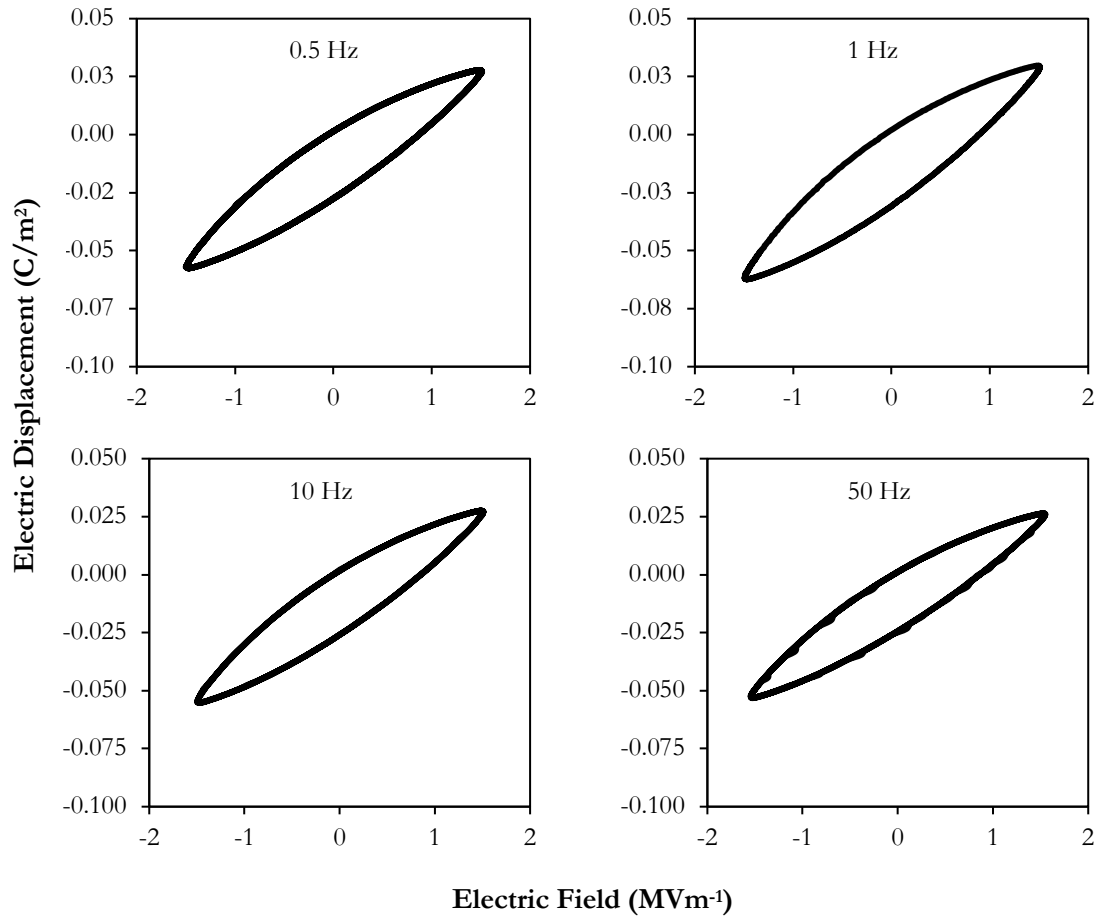


Figure 3.5. Polarization curves of EC-65 as a function of frequency.

3.3 Results and Discussion

3.3.1 EC-65

The polarization curves of EC-65 were obtained from 20°C to 120°C and are shown in Figure 3.6. EC-65 is a soft PZT ceramic manufactured by EDO Ceramic. The sample analyzed was a thin disk with a radius $r = (14.99 \pm 0.01)$ mm, a thickness $t = (1.01 \pm 0.01)$ mm, and a density $d = (7560 \pm 10)$ kg/m³. Figure 3.6 reveals that in general, as the temperature of this soft PZT ceramic increases, the polarization and the hysteresis increase as a direct result of the extra energy available for domain wall motion.

It can also be seen that the loop grows asymmetrically and that polarization increases only in the negative direction, which either suggests the presence of impurities in the material or domains that are stuck in one particular orientation and prevent polarization in the other direction. Two tests were made in order to verify that this phenomenon was not caused by the experimental setup. First, the piezoelectric disk was turned around and the polarization curve was re-obtained. The new curve was asymmetrical again, and only the positive polarization increase, as expected. Second, the sample was replaced by high-quality PLZT and PMN-PT samples, which produced perfectly symmetrical curves, as demonstrated in Sections 3.1.2 and 3.2.4, ruling out experimental bias.

A maximum polarization of 0.17 C/m² was obtained at 120°C, which is relatively high for a mixed-powder bulk ceramic. PLZT and PMN-PT crystals reached values up to 0.33 C/m², but other lead metaniobate bulk ceramics only reached values up to 0.07 C/m². Finally, it can be seen in Figure 3.6 that the saturation state of EC-65 was not reached. The voltage required to reach the saturation state short-circuited the sample even in the oil bath, possibly due to impurities or contaminants in the oil.

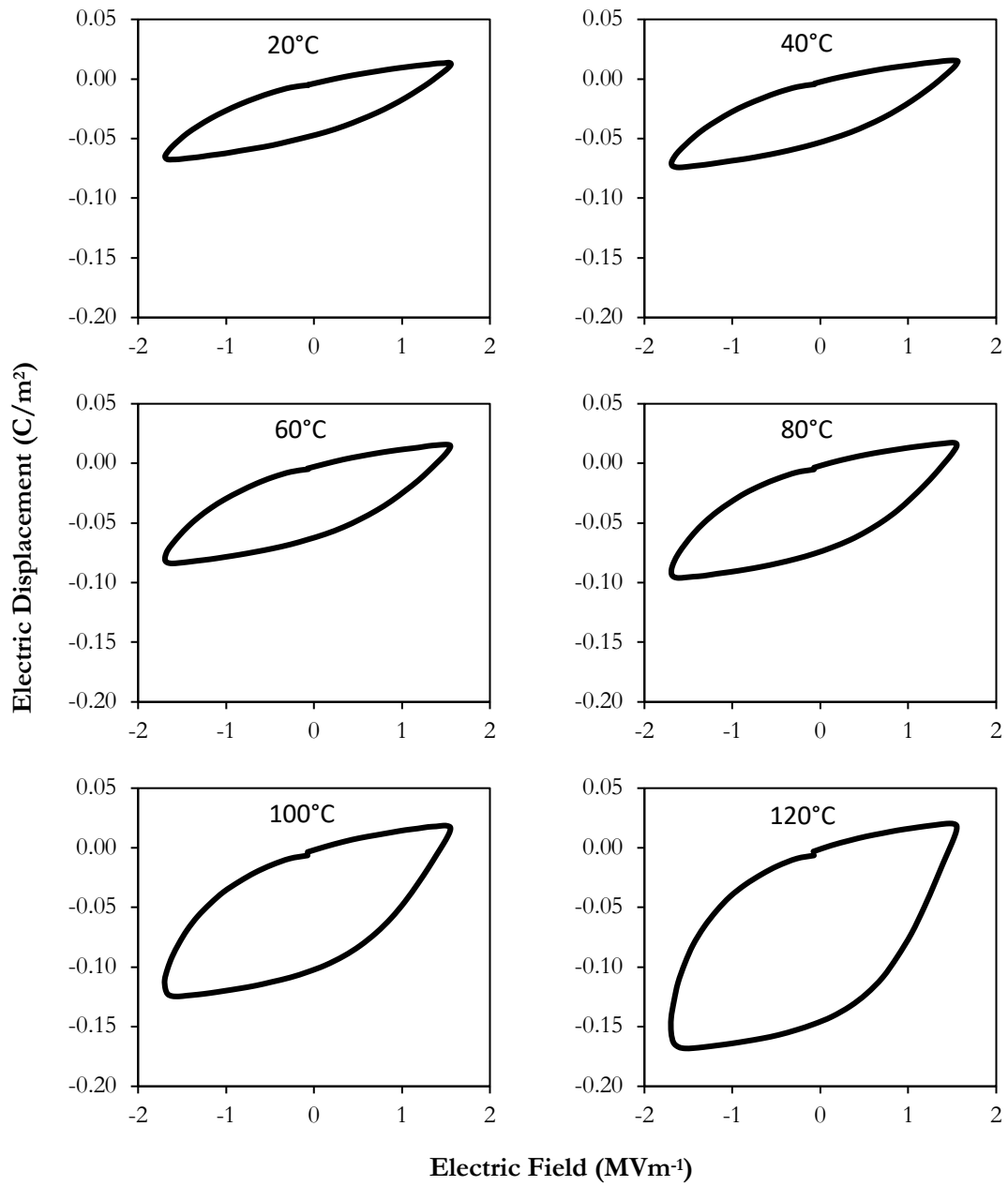


Figure 3.6. Polarization curves of EC-65 from 20°C to 120°C.

3.3.2 PLZT 9.5

The polarization curves of PLZT 9.5 were obtained by cooling the sample from room temperature down to -40°C , as illustrated in Figure 3.7. This translucent ferroelectric ceramic was manufactured by Motorola CTS Electronic Components. The sample analyzed was a thin plate with dimensions $a = (9.89 \pm 0.01)$ mm, $b = (10.22 \pm 0.01)$ mm, $t = (0.64 \pm 0.01)$ mm and a density $d = (7780 \pm 10)$ kg/m³. Figure 3.7 demonstrates that as the temperature decreased, hysteresis increased, which is opposite to what happened in the PZT sample. This demonstrates, once again, that a small change in a material's composition can have a dramatic impact on its piezoelectric and ferroelectric properties. The increased hysteresis at lower temperatures for PLZT is caused by the phase change around 10°C from a relaxor ferroelectric phase to a pure ferroelectric phase [70].

In Figure 3.7, from 20°C to 10°C , the spontaneous polarization is zero, but hysteresis is still present. This phenomenon is typical of antiferroelectric materials and results in “pinched” hysteresis loops. This observation is consistent with Haertling's phase diagram, presented in Chapter 2, where PLZT 9.5 is situated around the antiferroelectric region at room temperature. However, the exact structure of the relaxor ferroelectric phase is complex and may include more than one type of crystal systems. The structure of PLZT has been studied by many authors [71] [72] [73], but it is still not fully understood. In 2009, this sample had been heated from 20°C to 130°C using a similar setup, and it was observed that the hysteresis almost completely disappeared around 80°C [74]. This corresponds to another phase change in PLZT from a relaxor ferroelectric phase to a non-ferroelectric phase.

Finally, the maximum electric displacement observed in PLZT 9.5 was 0.33 C/m^2 , which is amongst the highest for ferroelectric ceramics, and the polarization curve is very symmetrical, which indicates that the sample was very pure.

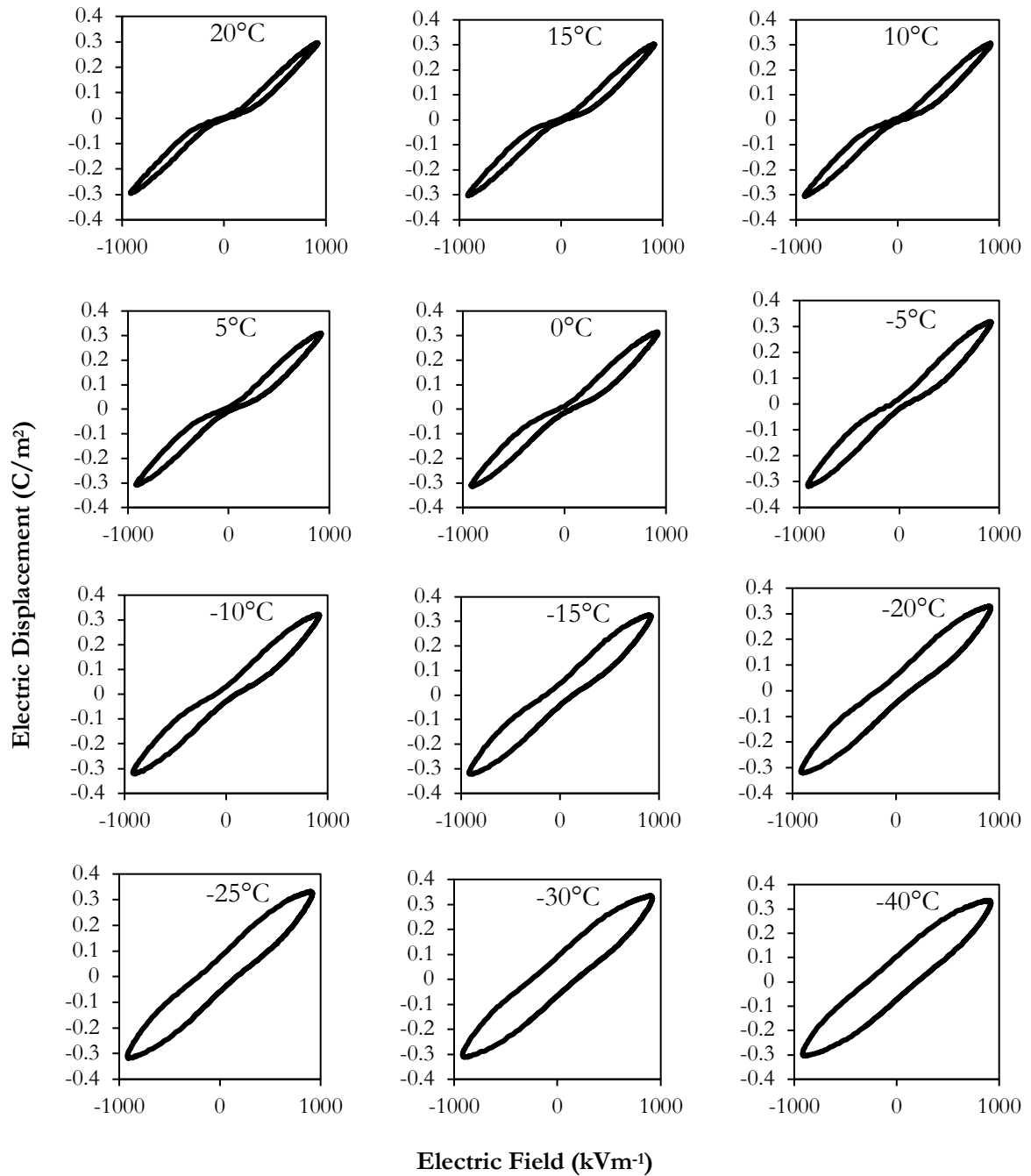


Figure 3.7. Polarization curves of PLZT 9.5 from 20°C to -40°C.

3.3.3 BM-941

The polarization curves of BM-941 were obtained from 30°C to 90°C and are shown in Figure 3.8. BM-941 is a modified lead metaniobate bulk ferroelectric ceramic manufactured by Sensor Technology Limited. The sample analyzed was a disk with a radius $r = (10.46 \pm 0.01)$ mm, a thickness $t = (2.56 \pm 0.01)$ mm, and a density $d = (5710 \pm 10)$ kg/m³. Figure 3.8 reveals that in general, as the temperature of this lead metaniobate bulk ceramic increases, the polarization and the hysteresis increase as a direct result of the extra energy available for domain wall motion.

It can also be seen that the loop grows asymmetrically and that polarization increases only in the negative direction, just like in EC-65. Once again, the presence of impurities in the material or a domain preferential orientation are suspected. The same two tests were performed in order to confirm that the asymmetry was not caused by the experimental setup.

A maximum polarization of 0.07 C/m² was obtained at 90°C, which is lower than the maximum polarization of 0.17 C/m² obtained for EC-65. However, the density of BM-941 is 33% lower than the density of EC-65, and if the density of BM-941 were increased, a higher polarization is expected. Finally, it can also be seen in Figure 3.8 that the saturation state of BM-941 was not reached, because the voltage required to reach the saturation state short-circuited the sample, even in oil.

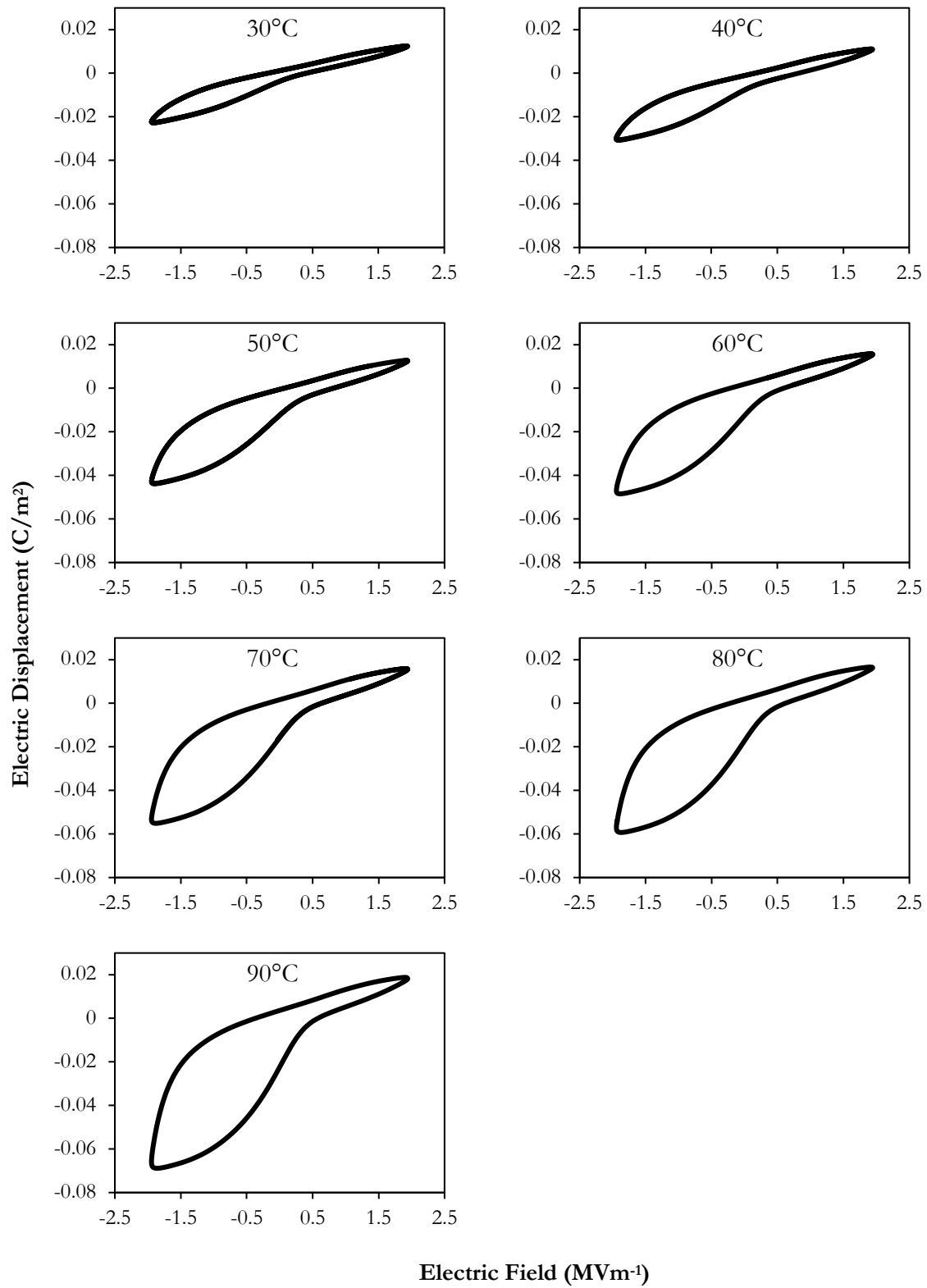


Figure 3.8. Polarization curves of BM-941 from 30°C to 90°C.

3.3.4 BM-600

The polarization curve of BM-600 was obtained at room temperature and is shown in Figure 3.9. BM-600 is a modified lead-magnesium-niobate bulk ferroelectric ceramic manufactured by Sensor Technology Limited. The sample analyzed was a thin disk with a radius $r = (5.03 \pm 0.01)$ mm, a thickness $t = (0.99 \pm 0.01)$ mm, and a density $d = (7820 \pm 10)$ kg/m³.

The thin loop observed in Figure 3.9 is characteristic of electrostrictive materials, which agrees with the manufacturer's claim that this material is electrostrictive. Materials with thin polarization loops are very useful in applications requiring little or no hysteresis, for example when no remnant polarization or no time response lag is desired.

A maximum polarization of 0.24 C/m² was obtained at 20°C, which is higher than the maximum polarization of EC-65 and BM-941, but lower than the electrostrictive PLZT 9.5. The density of BM-600 is 37% higher than the density of BM-941, which helps boost its maximum polarization, amongst other factors. Note that the maximum electric field applied on the sample was only 1000 kV/m, which was sufficient to reach the saturation state of BM-600. The application of higher electric fields did not increase its maximum polarization. Finally, the polarization curve in Figure 3.9 is perfectly symmetrical, which means that the domains in this sample had no preferential domain wall motion.

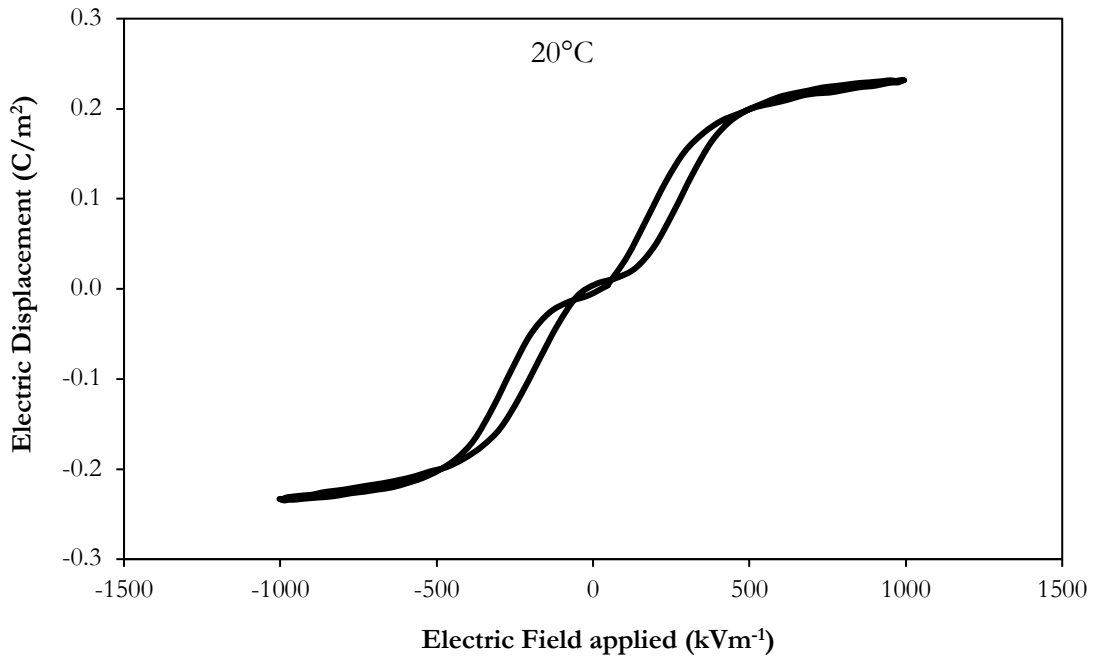


Figure 3.9. The polarization curve of BM-600 at 20°C.

3.3.5 PMN-PT

The polarization curve of PMN-PT was obtained at room temperature and is shown in Figure 3.10. PMN-PT is a lead-magnesium-niobate/lead-titanate single crystal manufactured by TRS Technologies. The sample analyzed was a thin plate with dimensions $a = (5.00 \pm 0.01)$ mm, $b = (5.00 \pm 0.01)$ mm, $t = (1.00 \pm 0.01)$ mm and a density $d = (8120 \pm 10)$ kg/m³.

The rectangular loop obtained in Figure 3.10 is consistent with the single crystal nature of PMN-PT, because single crystals only have one domain, which is either pointing up or down, resulting in a rectangular loop. The hysteresis loop, however, is not perfectly rectangular. Mnyukh [75] states that “rectangular sigmoid [hysteresis loops] are for crystals of multiple [domains]”, whereas pure single crystals have perfectly rectangular hysteresis loops. This suggests that the single crystal manufactured by TRS Technologies might contain

more than one domain, which is possible since pure single crystals of that size are very hard to grow.

Finally, a maximum polarization of 0.30 C/m^2 was obtained at 20°C , which is amongst the highest polarization observed in this thesis, as expected from a single crystal. An electric field of 650 kV/m^{-1} was necessary to reach the saturation state of PMN-PT, and the polarization curve is perfectly symmetrical, which is evidence to support the high purity of this sample.

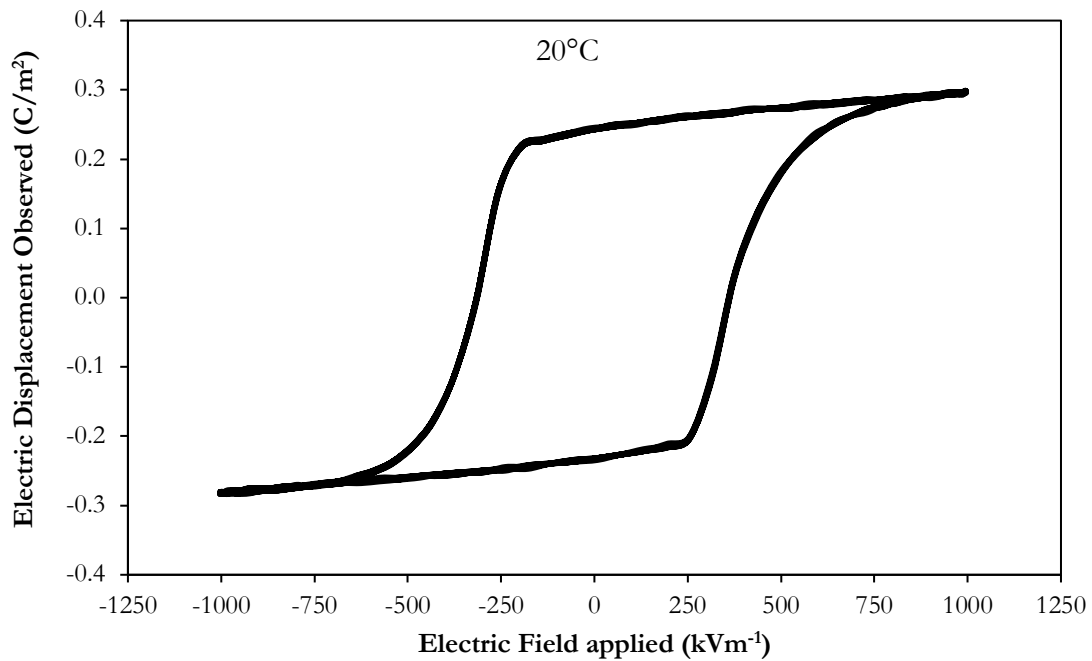


Figure 3.10. The polarization curve of PMN-PT at 20°C .

3.3.6 BM-150

The polarization curve of BM-150 was obtained at room temperature and is shown in Figure 3.11. BM-150 is a lead-free piezoelectric ceramic with unknown composition manufactured by Sensor Technology Limited. The sample analyzed was a thin disk with a radius $r = (5.03 \pm 0.01)$ mm and a thickness $t = (0.99 \pm 0.01)$ mm.

The hysteresis loop is not perfectly symmetrical, although it is more symmetrical than BM-941. It appears that the saturation state in the negative polarization was almost reached, which explains why the maximum polarization is slightly less in the negative direction.

A maximum polarization of 0.11 C/m^2 was obtained at 20°C , which is higher than the maximum polarization of BM-941, but lower than EC-65, PLZT 9.5, BM-600 and PMN-PT. The maximum electric field that could be applied on the sample was 750 kV/m , because higher voltages short-circuited the sample. The maximum polarization for BM-150 is not expected to be much higher, however, since the saturation state was almost reached in the negative direction at 750 kV/m .

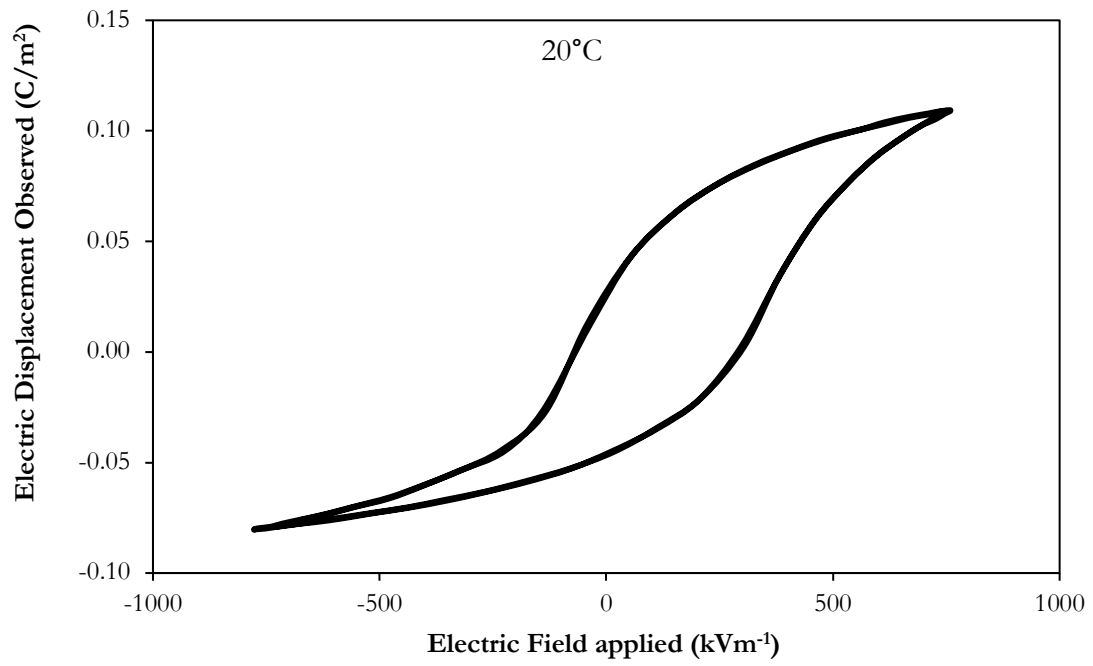


Figure 3.11. The polarization curve of BM-150 at 20°C.

CHAPTER 4 : DIELECTRIC PROPERTIES OF PIEZOELECTRIC MATERIALS

Chapter 4 focuses on the dielectric properties of piezoelectric materials. The first section describes how impedance can be used to determine the relative permittivity and the dielectric loss tangent of piezoelectric materials. Then, the experimental procedure and the impedance analyzer and are presented. Finally, the relative permittivity and the dielectric loss tangent of EC-69, PLZT 9.0, PLZT 9.5, and BM-941 are presented and analyzed.

4.1 Theory

Impedance is an important parameter used to characterize electronic circuits, components, and the materials used to make components. Impedance (Z) is generally defined as the total opposition that a device offers to the flow of an alternating current (AC) at a given frequency and is represented as a complex quantity [76]. An impedance vector consists of a real part (resistance R) and an imaginary part (reactance X), which can be expressed as $Z = R + jX$. Impedance is commonly used to represent a resistance and a reactance in series, because it can be expressed simply as a complex sum. In parallel circuits, it is mathematically easier to work using the reciprocal of impedance, which is called admittance Y and is defined as $Y = G + jB$, where G represents conductance and B represents susceptance. The quality factor Q serves as a measure of reactance purity; in other words, how close it is to being a pure reactance with no resistance [77]. It is defined as the ratio of the energy stored in a component to the energy dissipated by the component. The

quality factor is a dimensionless unit and is expressed as $Q = X/R$. The reciprocal of Q is called loss tangent ($\tan\delta$) and is expressed as $\tan\delta = R/X$.

An impedance analyzer can measure the real and the imaginary parts of impedance and convert them into the following parameters: R , X , G , B , C , and L , where L is inductance and C is capacitance. The conversion from impedance into R , X , G , B , C , and L is complex, because no circuit components are purely resistive or reactive [78]. This means that all capacitors have unwanted resistance and inductance, and all inductors have unwanted resistance and capacitance. Piezoelectric ceramics exhibit both capacitive reactance and inductive reactance. The capacitive reactance is larger away from resonance frequencies, and the inductive reactance is greater close to resonance frequencies. An equivalent circuit that considers both the capacitive reactance and the inductive reactance for a piezoelectric ceramic is shown in Figure 4.1.

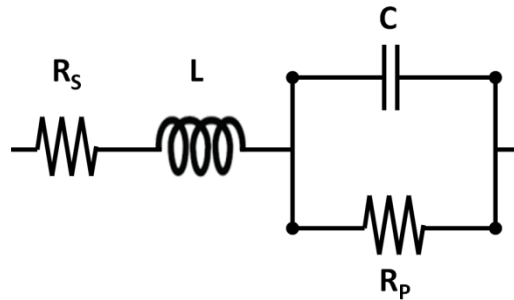


Figure 4.1. Equivalent circuit diagram for a piezoelectric ceramic. R_s is the series resistance and R_p is the parallel resistance.

The impedance for this circuit is expressed as [76]:

$$Z = R_s + \frac{R_p}{1 + \omega^2 R_p^2 C^2} + j \frac{\omega L - \omega R_p^2 C + \omega^3 R_p^2 L C^2}{1 + \omega^2 R_p^2 C^2} \quad (4.1)$$

where ω is the angular frequency. The resistance, which is the real part of impedance, is given by:

$$R = R_s + \frac{R_p}{1 + \omega^2 R_p^2 C^2} \quad (4.2)$$

and the reactance, which is the imaginary part of impedance, is given by:

$$X = \frac{\omega L - \omega R_p^2 C + \omega^3 R_p^2 L C^2}{1 + \omega^2 R_p^2 C^2} \quad (4.3)$$

From these equations, R, X, G, B, C, and L are calculated by the impedance analyzer. The full derivation of these equations can be found in the Agilent Technologies Impedance Handbook [76]. The relative permittivity can be found from the capacitance by using the relationship that describes the capacitance of a parallel-plate capacitor:

$$C = \frac{A \epsilon_r \epsilon_o}{d} \quad (4.4)$$

where A is the sample's area, ϵ_r is the relative permittivity, ϵ_o is the permittivity of free space, and d is the sample thickness [79]. The loss tangent can be found by dividing the resistance by the reactance:

$$\tan \delta = \frac{R}{X} = \frac{\epsilon_{real}}{\epsilon_{complex}} \quad (4.5)$$

where ϵ_{real} is the real part of the relative permittivity and $\epsilon_{complex}$ is the complex part of the relative permittivity.

4.2 Experimental Procedure

The impedance of four materials, EC-69, PLZT 9.0, PLZT 9.5, and BM-941, were measured as a function of temperature, and their relative permittivity and loss tangent were determined. The impedance was measured by using an Agilent 4294A Precision Impedance Analyzer. The temperature was controlled by a Delta Design 9023 temperature chamber with a 9015 Controller, cooled by liquid nitrogen and heated electrically. A Hewlett-Packard 16048A 1-meter Test Leads connected the four terminals of the impedance analyzer to the temperature chamber, as shown in Figure 4.2. The process was automated using a computer program called “Piezoelectric Resonance Analysis Program” (PRAP), by TASI Technical Software, version 2.2. PRAP can communicate with several instruments simultaneously through an IEEE 488 GPIB interface, such as the temperature chamber and the impedance analyzer. Once the experimental parameters were entered into PRAP, such as the desired temperature range, voltage, frequency, sample’s dimension and density, the software calculated the relative permittivity and loss tangent at various temperatures.

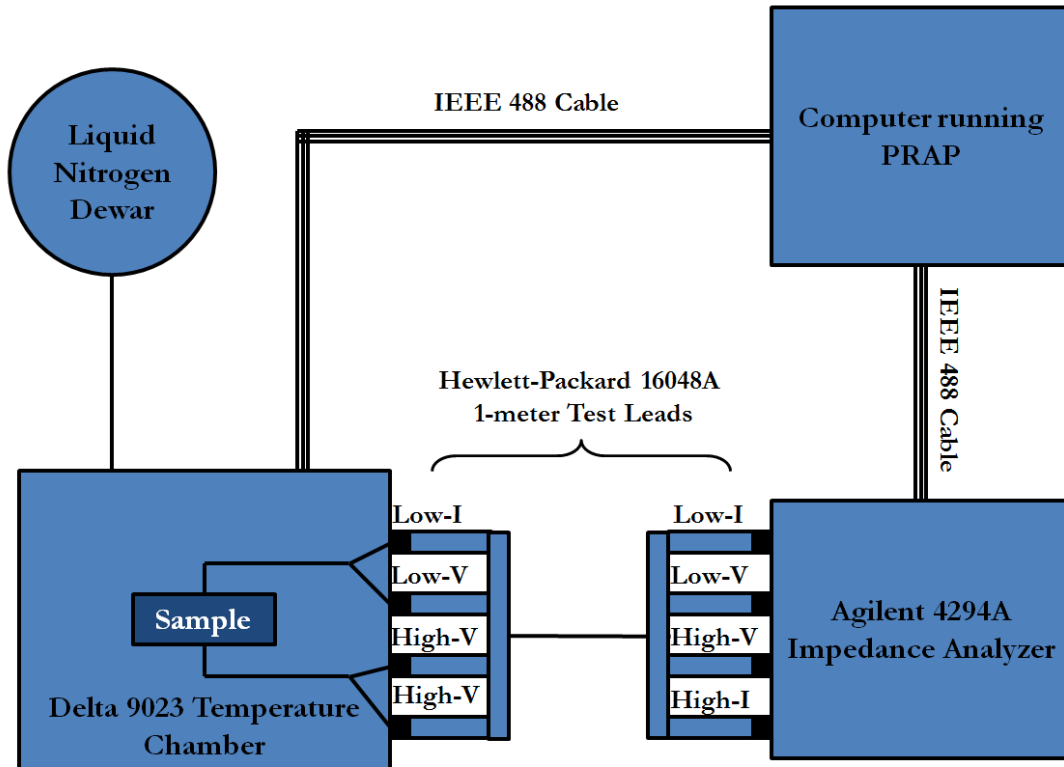


Figure 4.2. The experimental setup used to find the relative permittivity and the dielectric loss tangent as a function of temperature.

4.3 Results and Discussion

4.3.1 EC-69

The relative permittivity and dielectric loss tangent of EC-69 were obtained from -40°C to 140°C and are shown in Figures 4.3 and 4.4 respectively. The sample analyzed was a disk with a radius $r = (14.96 \pm 0.01)$ mm, a thickness $t = (1.01 \pm 0.01)$ mm, and a density $d = (7560 \pm 10)$ kg/m³. Figure 4.3 reveals that as the temperature increases, the relative permittivity generally increases due to the unfreezing of domains. Between -40°C and 20°C , the relative permittivity at 300 kHz decreases because this frequency is close to a resonance frequency, which also explains why the relative permittivity at 300 kHz is higher than at

100 kHz and 500 kHz. The exact chemical composition of EC-69 has not been revealed by EDO Ceramics; however, the ratio of Zr/Ti is estimated to be 53/47 [80]. This composition falls along the MPB on the PZT phase diagram [81], so no phase change was expected to occur in this temperature range. The results obtained support this idea since no broad peaks were observed in the relative permittivity or in the dielectric loss tangent between -40°C to 140°C . In fact, the only phase change that should occur in this sample is at $T_c = 300^{\circ}\text{C}$, where the crystal structure becomes cubic, and also possibly a phase change to monoclinic below -100°C [54]. According to the manufacturer, this material was designed to provide unmatched performance for high power acoustic projectors or deep water applications where low losses are required [54]. Thus, the dielectric loss tangent curves in Figure 4.4 suggest that the operational range for EC-69 is between -20°C and 120°C because this material experiences high losses at lower and higher temperatures. Finally, hysteresis is observed in EC-69 as shown in Figure 4.3. The material was first cooled from 20°C (#1) down to -40°C (#2), then heated to 20°C (#3), then to 140°C (#4), and finally cooled to 20°C (#5). Since the sample was cooled first, no hysteresis is observed from point #1 to point #3. However, hysteresis appears from point #3 to point #5. This observation agrees with the polarization curves obtained for EC-69 in Chapter 3 and are consistent with previous publications [82].

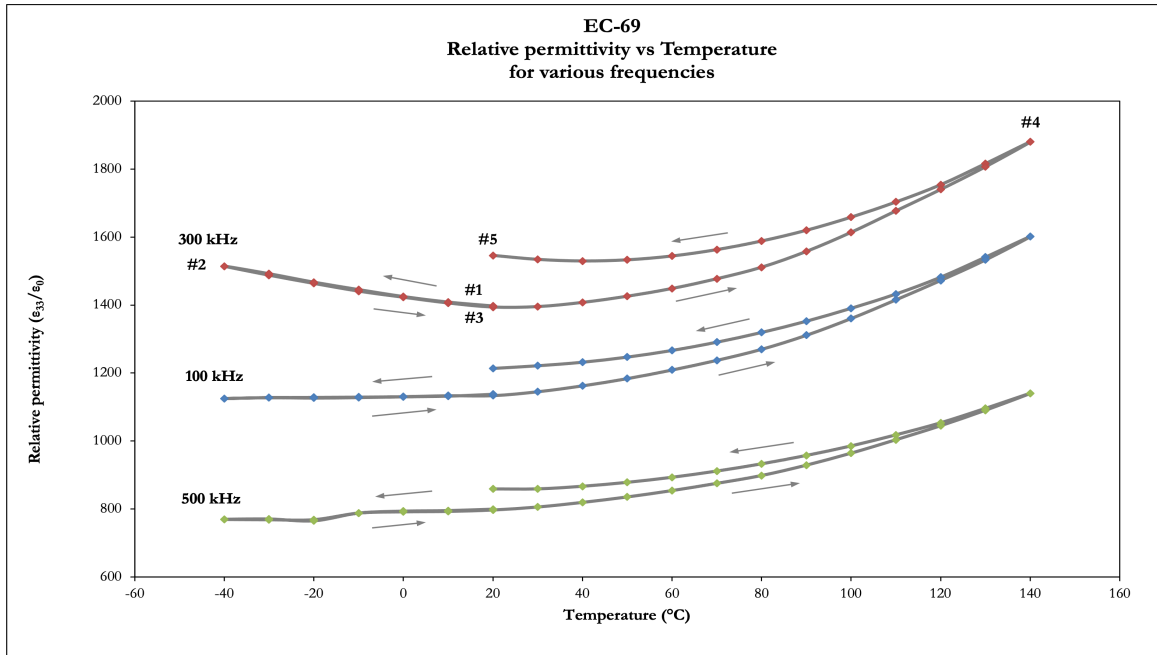


Figure 4.3. The relative permittivity of EC-69 as a function of temperature at various probing frequencies.

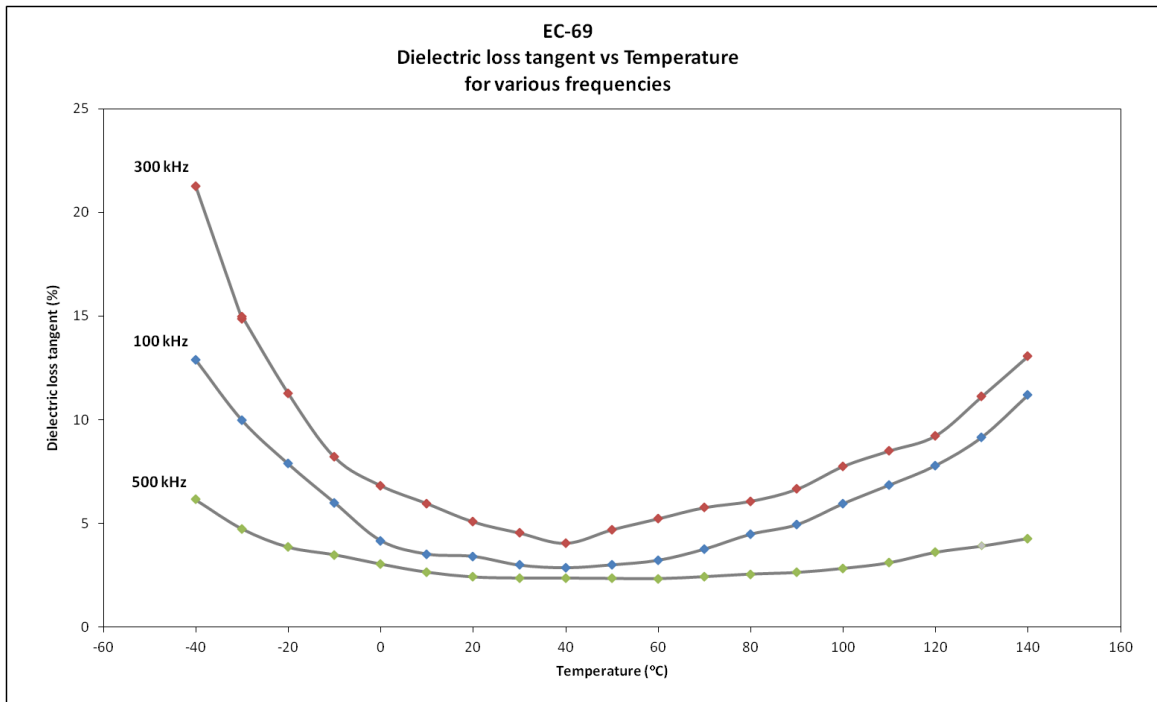


Figure 4.4. The dielectric loss tangent of EC-69 as a function of temperature at various probing frequencies.

4.3.2 PLZT 9.0 and PLZT 9.5

The relative permittivity and dielectric loss tangent of PLZT 9.0 and 9.5 were obtained from -40°C to 140°C and are shown in Figures 4.5 to 4.9. The PLZT 9.0 sample was a thin plate with dimensions $a = (10.32 \pm 0.01)$ mm, $b = (10.11 \pm 0.01)$ mm, $t = (0.54 \pm 0.01)$ mm and a density $d = (7720 \pm 10)$ kg/m³. The PLZT 9.5 sample was a thin plate with dimensions $a = (9.85 \pm 0.01)$ mm, $b = (10.18 \pm 0.01)$ mm, $t = (0.64 \pm 0.01)$ mm and a density $d = (7780 \pm 10)$ kg/m³. As seen in Figures 4.5 and 4.7, the relative permittivity generally increases as a function of temperature due to the unfreezing of domains. Around 80°C , the relative permittivity stops to increase and starts to decrease due to a phase change from a relaxor ferroelectric phase to a paraelectric phase. Another broad peak can be observed around 10°C , which suggests that there exists a second order phase change at this temperature. Evidence for these two phase changes can also be seen in the dielectric loss tangent in Figures 4.6 and 4.8. At room temperature, PLZT 9.0 and 9.5 are situated at the cross-section of the tetragonal, rhombohedral, and slim ferroelectric regions on the PLZT phase diagram [65], so the phase changes that occur at 10°C and 80°C cannot be identified easily. Finally, Figure 4.9 reveals that PLZT 9.5 generally has a higher relative permittivity than PLZT 9.0 and its T_c is lower than for PLZT 9.0, which is consistent with Haertling [83] and Sabat's [84] observations that higher lanthanum content reduces T_c .

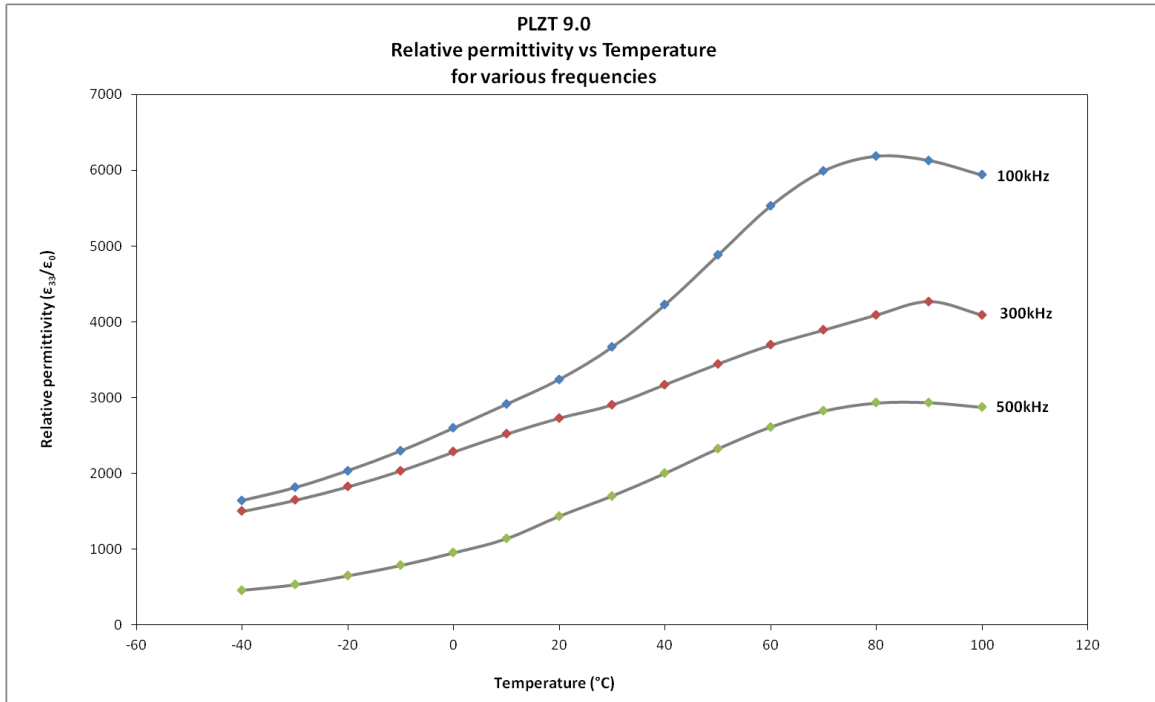


Figure 4.5. The relative permittivity of PLZT 9.0 as a function of temperature at various probing frequencies.

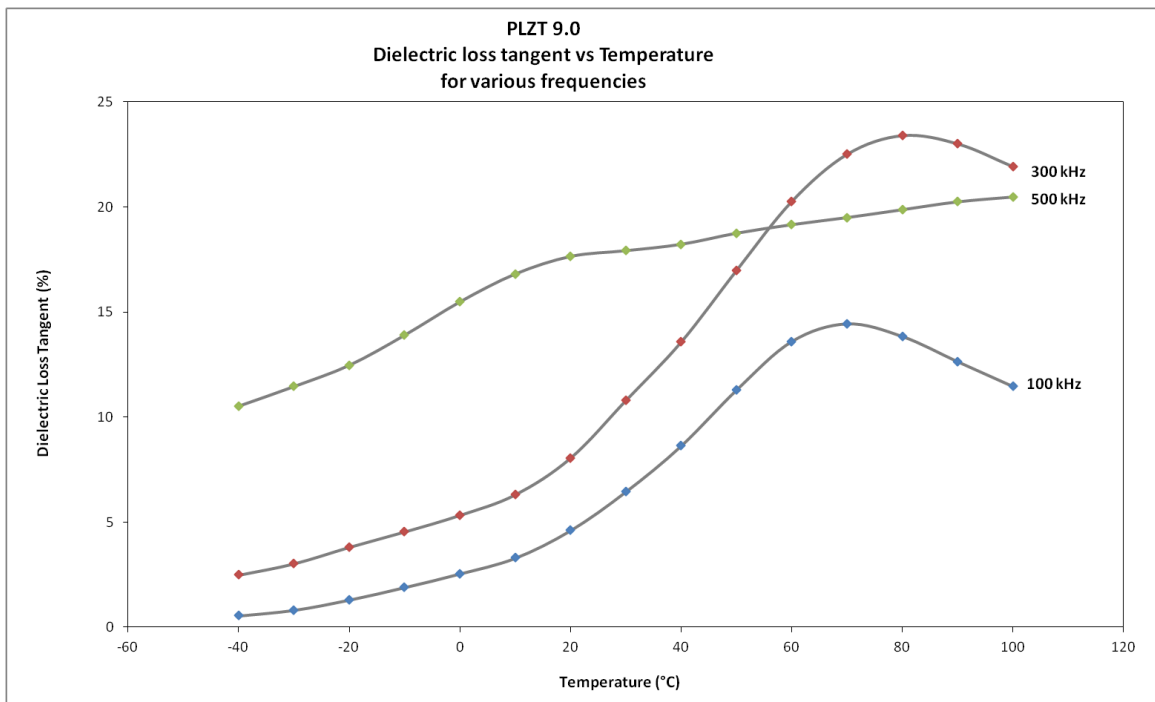


Figure 4.6. The dielectric loss tangent of PLZT 9.0 as a function of temperature at various probing frequencies.

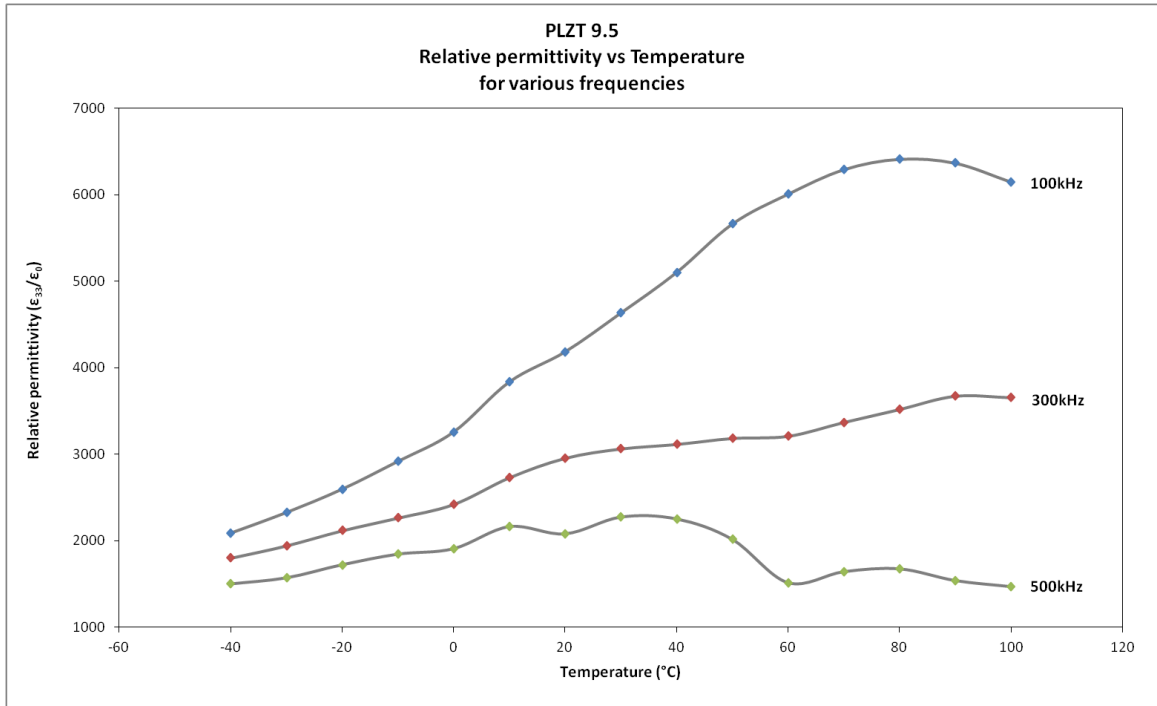


Figure 4.7. The relative permittivity of PLZT 9.5 as a function of temperature at various probing frequencies.

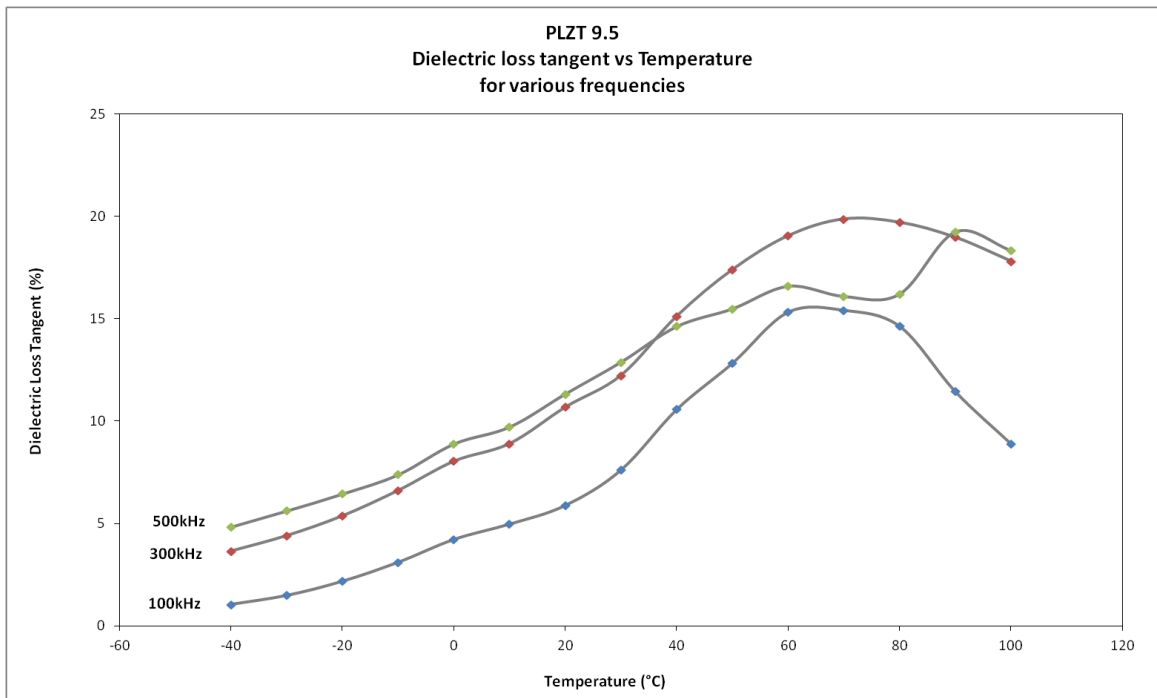


Figure 4.8 The dielectric loss tangent of PLZT 9.5 as a function of temperature at various probing frequencies.

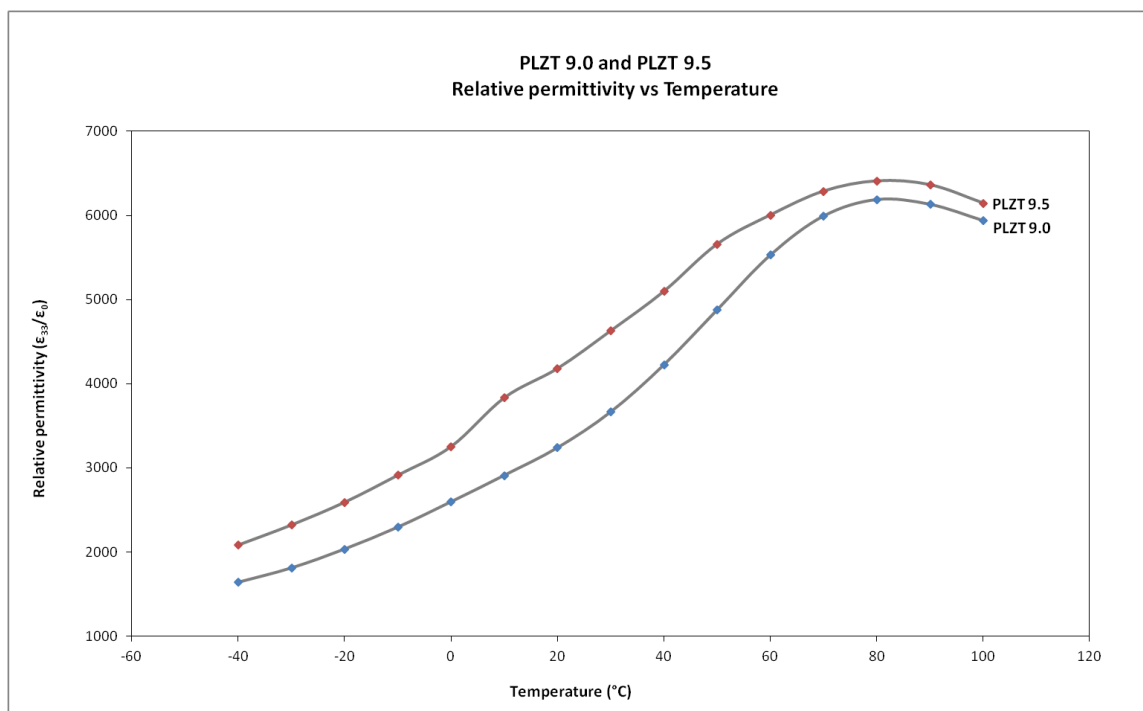


Figure 4.9. The relative permittivity of PLZT 9.0 compared to PLZT 9.5 as a function of temperature at 100 kHz.

4.3.3 BM-941

The relative permittivity and dielectric loss tangent of BM-941 were obtained from -150°C to 200°C and are shown in Figures 4.10 and 4.11 respectively. The sample analyzed was a disk with a radius $r = (10.46 \pm 0.01)$ mm, a thickness $t = (2.58 \pm 0.01)$ mm, and a density $d = (5710 \pm 10)$ kg/m³. In general, as the temperature increases, the relative permittivity increases due to the unfreezing of domains. At 10°C in Figure 4.10, a peak can be observed in the relative permittivity, which suggests a phase change. The position of the peak is dependent on frequency, which means that BM-941 exhibits relaxor-like behaviour. Another broad peak, which is less obvious than the first one, can be observed around 130°C , both in the relative permittivity and the dielectric loss tangent, which suggests that there might be a potential second order phase change at this temperature. The phase diagram for

BM-941 has not been established yet, so the results obtained cannot be compared to a phase diagram. It is known, however, that T_c for BM-941 is 280°C [85], so heating the sample above this temperature would result in a sharp drop in the relative permittivity. In Figure 4.11, the dielectric loss tangent of BM-941 does not increase at low or high temperatures, as opposed to EC-69, which means that BM-941 can be used over a wider range of temperatures than EC-69. Also, BM-941 exhibits a large peak in its dielectric loss tangent around room temperature, which translates into an unusually low mechanical quality factor. The effect of a low mechanical Q is to broaden the resonance and anti-resonance peaks in the electrical impedance spectra [86], which is useful for applications requiring low frequency dependence, such as broadband transducers and immersed non-destructive evaluation.

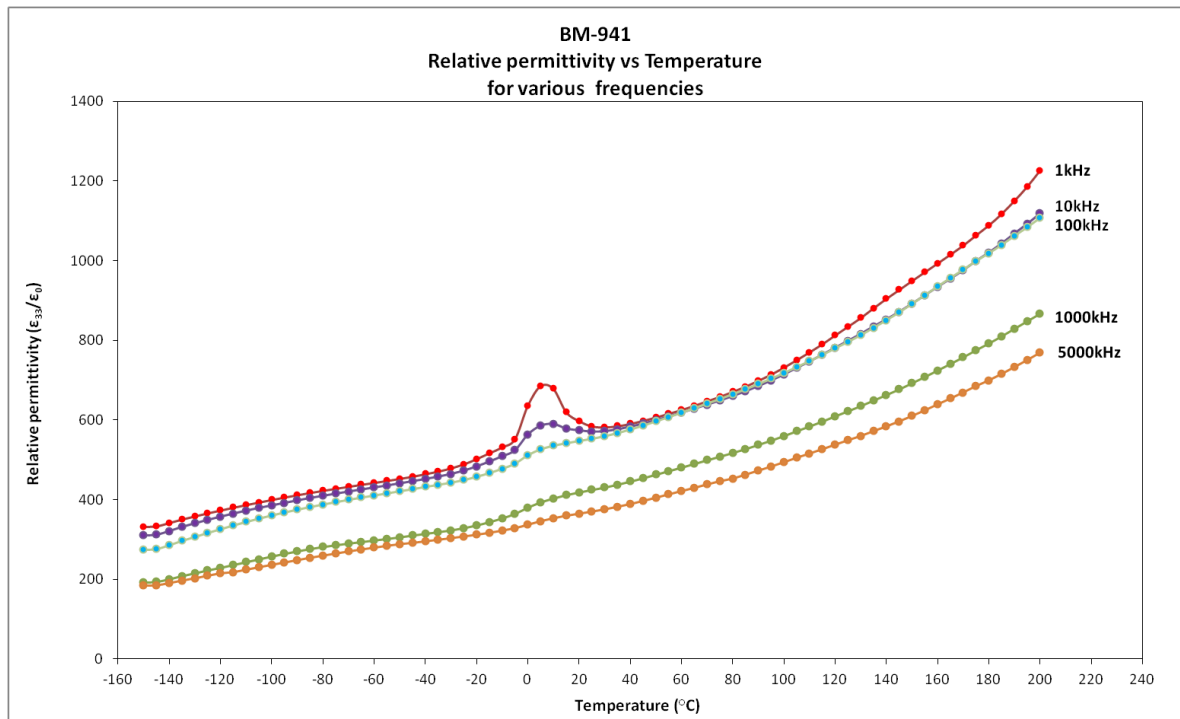


Figure 4.10. The relative permittivity of BM-941 as a function of temperature at various probing frequencies.

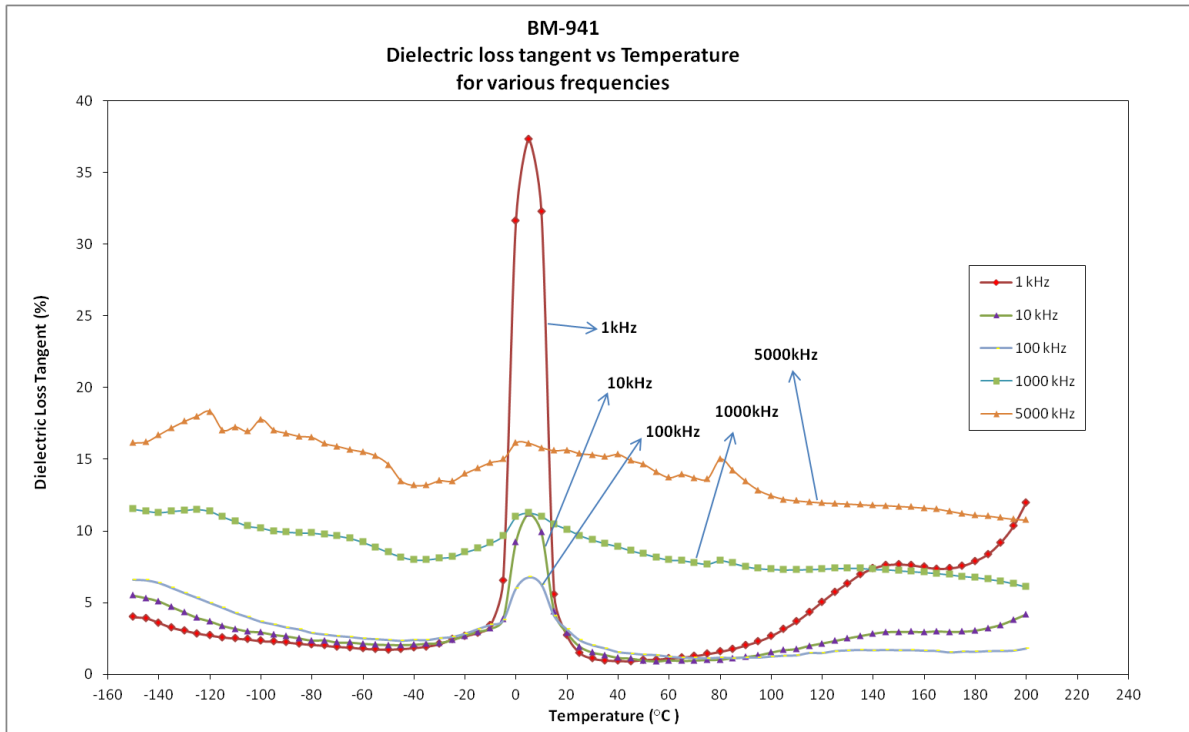


Figure 4.11. The dielectric loss tangent of BM-941 as a function of temperature at various probing frequencies.

CHAPTER 5 : ELECTROMECHANICAL PROPERTIES OF PIEZOELECTRIC MATERIALS

Chapter 5 starts with a discussion on piezoelectric equations derived from the Gibbs adiabatic function, leading to the numerical definition of piezoelectricity and electrostriction. The experimental procedure is then outlined and the inner workings of the laser Doppler vibrometer, used to measure the longitudinal strain in this thesis, are explained. Finally, the AC strain amplitude of BM-941 and PLZT 9.0 is presented as a function of the AC electric field for different frequencies, with and without a DC bias.

5.1 Theory

In Chapter 2, simplified linear piezoelectric equations were derived based on Mason's work, and strain was found to be a linear function. In reality, strain is a non-linear tensor of infinite rank where the first-order rank represents piezoelectricity and the second-order rank represents electrostriction [87]. While piezoelectricity can only occur in certain types of crystals, electrostriction can occur in any dielectric material.

The strain tensor S_{ij} can be derived from the isothermal adiabatic Gibbs function G using the following relationship [88] [84]:

$$S_{ij} = - \left(\frac{\partial G}{\partial T_{ij}} \right)_E \quad (5.1)$$

where T_{ij} is the stress tensor and E represents the electric field, and $i, j=1..3$. For a stress free unclamped system, equation 5.1 can be normalized with respect to the thermodynamic potential and written explicitly up to the fourth rank as follows:

$$S_{ij} = \sum_1^3 d_{ijk} E_k + \sum_1^3 \gamma_{ijkl} E_k E_l + \sum_1^3 \psi_{ijklm} E_k E_l E_m + \sum_1^3 \chi_{ijklmn} E_k E_l E_m E_n + \dots \quad (5.2)$$

where d_{ijk} is the piezoelectric coefficient, γ_{ijkl} is the electrostriction coefficient, and ψ_{ijklm} and χ_{ijklmn} are third and fourth rank coefficients of the electric field to strain tensor, and $i, j, k, l, m, n = 1..3$. If the electric field is only applied in the 3-direction, equation 5.2 reduces in matrix form to:

$$S_3 = d_{33} E_3 + \gamma_{333} E_3^2 + \psi_{3333} E_3^3 + \chi_{33333} E_3^4 + \dots \quad (5.3)$$

This equation can be used to predict the strain response in the 3-direction as a function of the electric field. Equation 5.3 shows that the piezoelectric response due to an electric field is linear and the electrostrictive response is quadratic. If a sinusoidal electric field with a DC bias component is applied to an irreversible electrostrictive material [88] [84], then equation 5.3 becomes:

$$\begin{aligned} S_3 = & d_{33}(E_{DC} + E_0 \cos(\omega t)) + \gamma_{333}(E_{DC} + E_0 \cos(\omega t))^2 \\ & + \psi_{3333}(E_{DC} + E_0 \cos(\omega t))^3 + \chi_{33333}(E_{DC} + E_0 \cos(\omega t))^4 + \dots \end{aligned} \quad (5.4)$$

Expanding equation 5.4 gives:

$$S_3 = [\dots] + [\dots] \cos(\omega t) + [\dots] \cos(2\omega t) + [\dots] \cos(3\omega t) + [\dots] \cos(4\omega t) + \dots \quad (5.5)$$

Equation 5.5 reveals that the strain response has a first, second, third, fourth, etc... harmonics, as illustrated in Figure 5.1. Figure 5.1 shows an example of a typical Fourier transform of the displacement magnitude of PLZT 9.0 for different harmonics given by VIBSOFT 4.5, the laser Doppler vibrometer software.

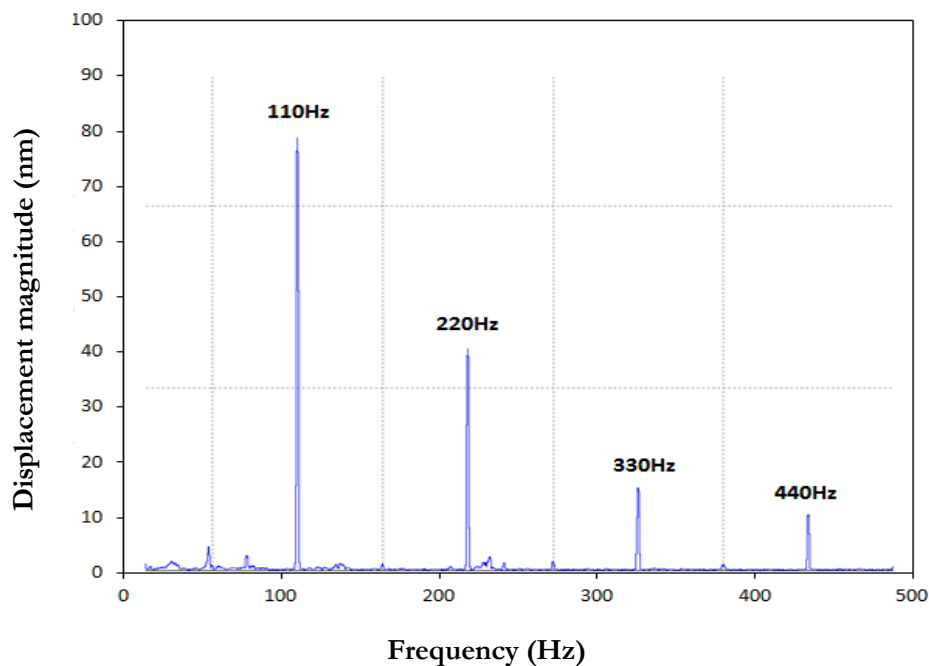


Figure 5.1. A typical Fourier transform of the displacement magnitude obtained by VIBSOFT 4.5 at 110 Hz for PLZT 9.0 at $278 \text{ kV}_{\text{AC}}\text{m}^{-1}$ and $500 \text{ kV}_{\text{DC}}\text{m}^{-1}$.

5.2 Experimental setup

The setup used to obtain strain measurements for PLZT 9.0 and BM-941 is presented in Figure 5.2. The longitudinal strain measurements were made using a state-of-the-art single-point Laser Doppler Vibrometer (LDV) manufactured by Polytec, including an OFV-505 sensor head, an OFV-5000 controller, and the VIBSOFT 4.5 software package.

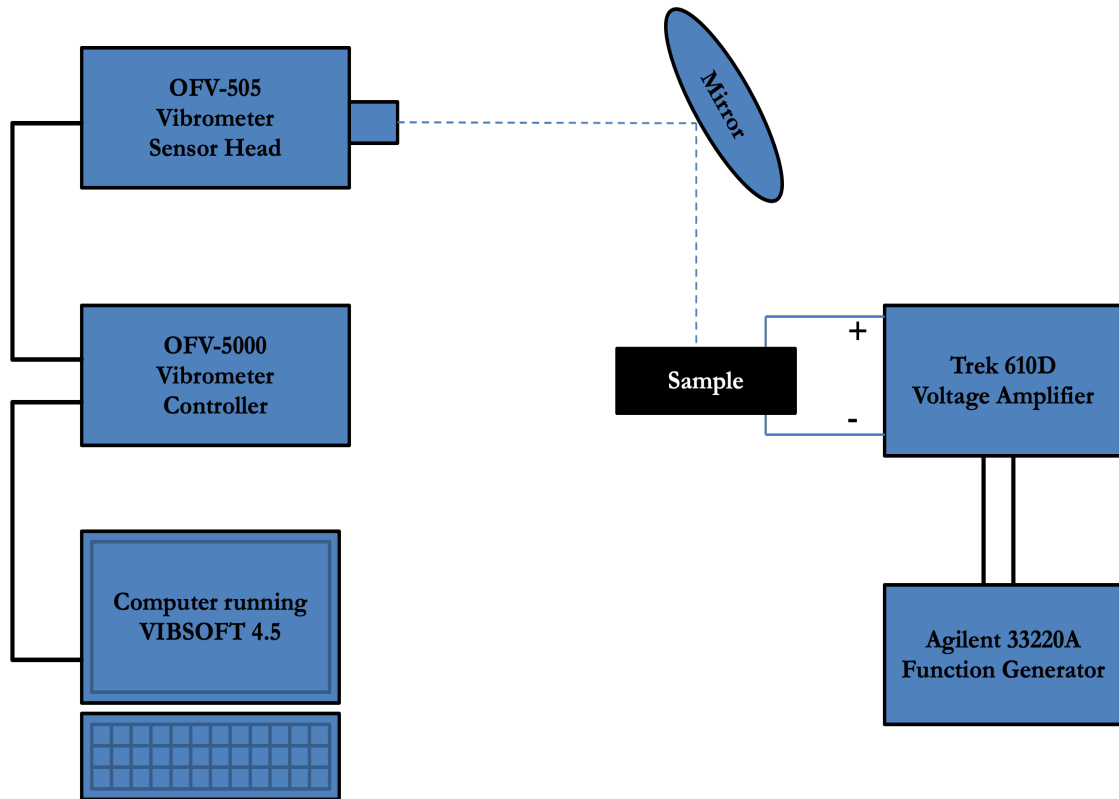


Figure 5.2. Experimental setup used to obtain the AC strain amplitude as a function of the AC and DC electric fields.

The LDV works on the basis of optical interference, requiring two coherent light beams, each with their respective light intensities I_1 and I_2 , to overlap. The resulting intensity I_{tot} is not just the sum of the single intensities, but is modulated according to the formula:

$$I_{tot} = I_1 + I_2 + 2\sqrt{I_1 I_2} \cos\left(\frac{2\pi\Delta l}{\lambda}\right) \quad (5.6)$$

where Δl is the path length difference between the two beams and λ is the wavelength of the laser [89] [90]. If the path difference is an integer multiple of the wavelength, the overall intensity is maximum, and, if the path length difference is one half of the wavelength, the overall intensity is zero.

Figure 5.3 shows how interferometry is used in the Polytec LDV. A beam of helium neon laser is split by a first beamsplitter into a reference beam and a measurement beam.

After passing through a second beamsplitter, the measurement beam is focused onto the sample. Light scatters back from the sample in all directions, but some portion of the light is reflected back towards the second beamsplitter. The measurement beam is then deflected towards the third beam splitter, where it is merged with the reference beam and directed onto the detector.

The path length of the reference beam is constant, but the path length of the measurement beam varies with time as a result of the sample's movement. The modulation frequency of the interference pattern corresponds to the Doppler frequency shift f_d introduced by the vibrating sample, which is directly proportional to the velocity v of the sample, according to the formula:

$$f_d = 2 \frac{v}{\lambda} \quad (5.7)$$

The interferometer can determine the velocity of the moving surface, but it cannot determine if the surface is moving towards the detector or away from the detector. For this purpose, a Bragg cell, which is an acousto-optic modulator, is placed in the reference beam in order to introduce a Bragg frequency shift f_b of 40 MHz. By comparison, the frequency of the original HeNe laser beam is 4.75×10^{14} Hz. This 40 MHz shift generates a modulation frequency on the interference pattern when the object is at rest. Therefore, if the object moves towards the interferometer, the modulation frequency will be below 40 MHz, and if it moves away from the vibrometer, the modulation frequency will be higher than 40 MHz. Thus, this method makes it possible not only to detect the amplitude of movement, but also to determine the direction of movement.

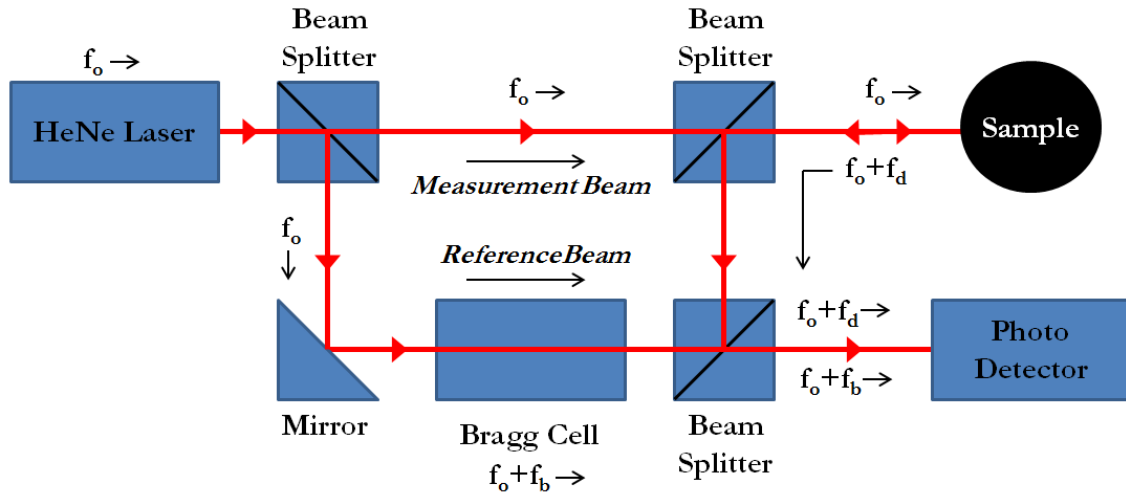


Figure 5.3. A schematic representation of the Polytec assembly [90].

In this experiment, the AC voltage and the DC bias were supplied by the same Agilent 33220A Function Generator and Trek 610D voltage amplifier as used in Chapter 3. Single DC strain measurements could not be obtained, because the sample must vibrate in order to generate a modulated signal which can be decoded. However, both single AC and combined AC and DC measurements were obtained successfully using the velocity decoder available within the VIBSOFT software. The displacement was determined by integrating the velocity signal as a function of time, and a Fourier analysis of the displacement signal converted the signal into the frequency domain.

5.3 Results and Discussion

5.3.1 PLZT 9.0

First, the mechanical resonance of the PLZT 9.0 sample and its fixture was investigated in order to determine what frequencies should be avoided when measuring strain. Strain measurements were not taken at peak frequencies in order to minimize the effect of mechanical resonance on the measurements. The PLZT 9.0 sample was a thin plate with dimensions $a = (10.32 \pm 0.01)$ mm, $b = (10.11 \pm 0.01)$ mm, $t = (0.54 \pm 0.01)$ mm, and density $d = (7720 \pm 10)$ kg/m³. The resonance peaks of the second harmonic were obtained from 100 Hz to 600 Hz at $300 \text{ kV}_{\text{ACm}^{-1}}$ and $0 \text{ kV}_{\text{DCm}^{-1}}$, and the results are shown in Figure 5.4. The first harmonic was found to be negligible in PLZT 9.0 when no DC bias was introduced, which agrees with the results from Chapter 3 where PLZT 9.0 was found to have minimal hysteresis at room temperature. Figure 5.4 shows that the sample and its fixture had resonance peaks at 110 Hz, 220 Hz, 330 Hz, and a large resonance peak at 440 Hz. Therefore, strain measurements were not taken at those frequencies.

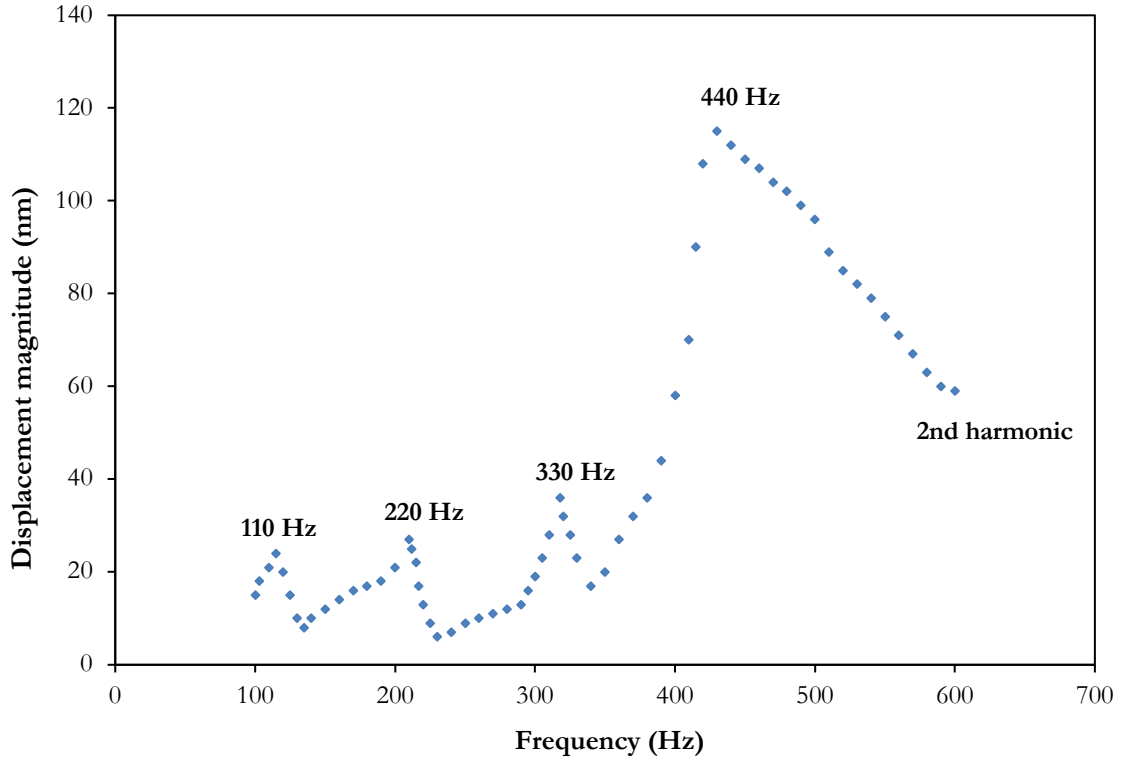


Figure 5.4. Mechanical resonance peaks for the second harmonic of the PLZT 9.0 sample and fixture at $300 \text{ kV}_{\text{AC}}\text{m}^{-1}$ and $0 \text{ kV}_{\text{DC}}\text{m}^{-1}$.

Next, the AC strain amplitude of PLZT 9.0 was obtained as a function of the AC electric field amplitude, with no DC bias, at 150 Hz, 250 Hz, 300 Hz, and 350 Hz at the first and second harmonic frequencies. AC fields of less than $200 \text{ kV}_{\text{AC}}\text{m}^{-1}$ did not produce significant strain, and AC fields were limited to $600 \text{ kV}_{\text{AC}}\text{m}^{-1}$ due to the maximum 2 mA current available from the Trek amplifier to drive the sample. This also explains the plateaux in the AC strain amplitude at 300 Hz and 350 Hz. Figure 5.5 shows that the strain response of PLZT 9.0 predominantly comes from the second harmonic, which is consistent with the fact that PLZT 9.0 is known to be electrostrictive at room temperature [84] [91]. It can also be seen that the strain amplitude reaches a maximum of $0.24 \times 10^{-3} \text{ mm}^{-1}$ at 300 Hz, which was the highest strain amplitude obtained in PLZT 9.0 without the application of a DC bias.

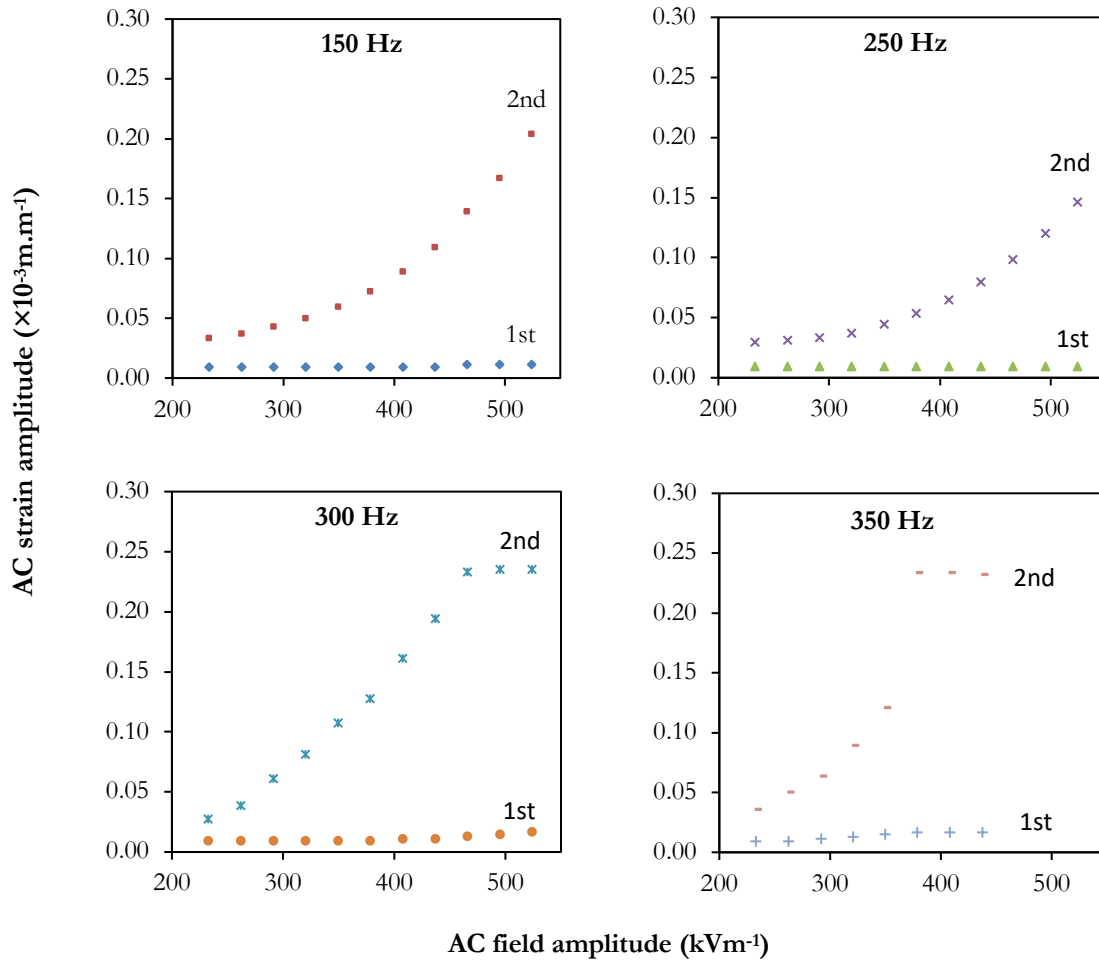


Figure 5.5. The AC strain amplitude of PLZT 9.0 as a function of the AC electric field amplitude, with no DC bias for different frequencies at the 1st and 2nd harmonic frequencies.

Next, the AC strain amplitude of PLZT 9.0 was obtained as a function of the DC bias electric field with a 278 kVm^{-1} peak-to-peak AC electric field for different frequencies at the first and second harmonic frequencies. Figure 5.6 reveals that the first harmonic piezoelectric strain is dominant and increases with the DC bias field until a maximum is reached. The strain peaks at approximately $1400 \text{ kV}_{\text{DC}}\text{m}^{-1}$ at all frequencies measured, and then seems to start decreasing. This general behavior of relaxor ferroelectrics has been reported by several authors [84] [92]. The increase in strain with increased DC bias is attributed to the increase in the dielectric permittivity with increasing DC bias field, which is

the result of a phase transition from the relaxor to the ferroelectric phase according to Bobnar *et al* [91]. This behavior also corroborates the results obtained in chapter 3.3.2 and 4.3.2 where a transition from the relaxor to the ferroelectric phase was observed around room temperature. Furthermore, in chapter 4, it was suggested that a higher number of available polarization states was responsible for the higher dielectric response in PLZT 9.0. Above a certain point, however, the number of available polarization states starts decreasing, which explains why the AC strain amplitude starts decreasing above a certain field, around $1400 \text{ kV}_{\text{DC}}\text{m}^{-1}$ for this sample.

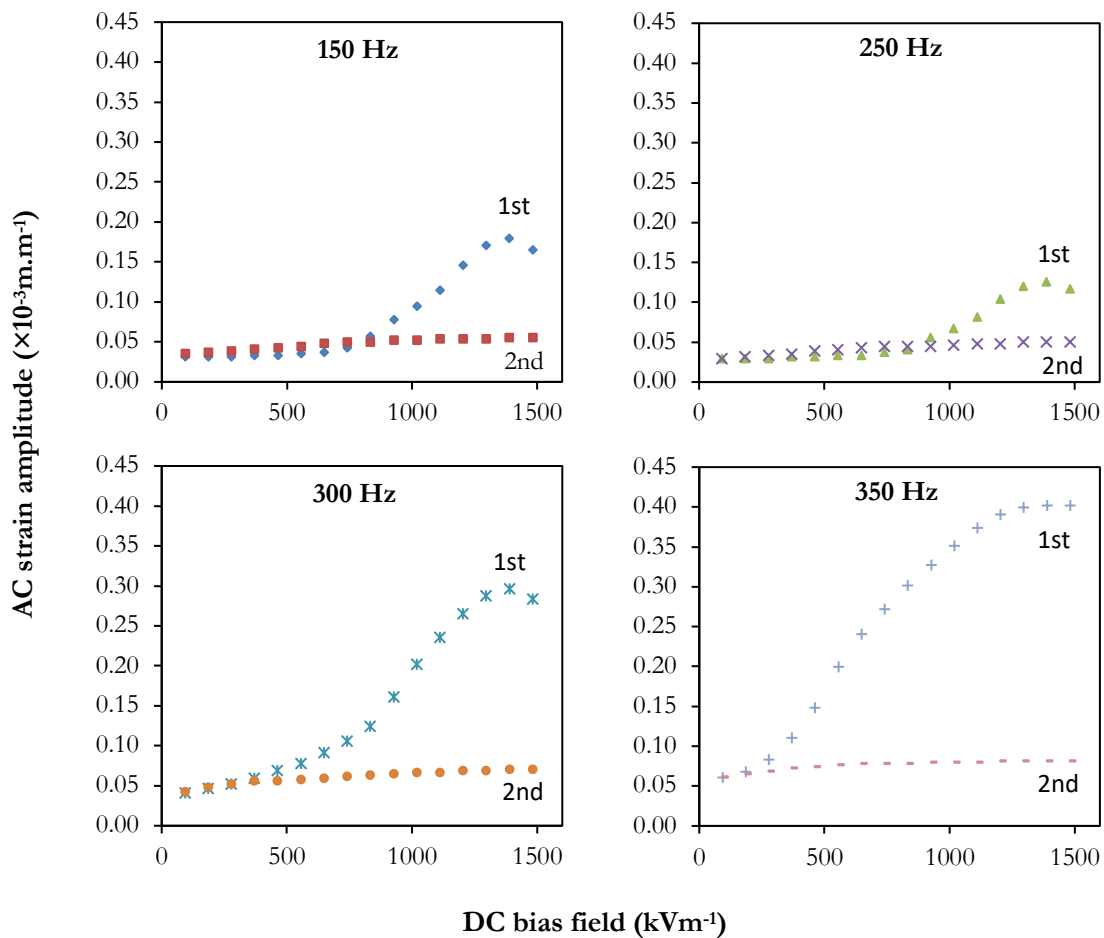


Figure 5.6. The AC strain amplitude of PLZT 9.0 as a function of the DC bias electric field, with a $278 \text{ kV}\text{m}^{-1}$ peak-to-peak AC electric field for different frequencies at the 1st and 2nd harmonic frequencies.

Next, the AC strain amplitude of PLZT 9.0 was measured at 150 Hz at the first harmonic frequency as a function of the DC bias electric field at various AC fields. The DC electric field cycled from 0 kVm^{-1} up to 1000 kVm^{-1} , down to 0 kVm^{-1} , then -1000 kVm^{-1} , and then back up to 0 kVm^{-1} , and the AC field varied between 185 kVm^{-1} and 648 kVm^{-1} . This cycle was repeated multiple times since previous research indicated that the strain response could increase with each cycle [84], but for this sample every cycle produced exactly the same results, which indicates that the domains in the sample were already stable and de-pinned.

Figure 5.7 also reveals that no hysteresis was induced by the DC electric field. This result is consistent with the polarization curves obtained in Chapter 3 where no hysteresis was present at room temperature. The application of a DC field, similar to the energy provided by heat, is believed to induce a phase change in PLZT from a relaxor to a more stable ferroelectric phase. It would be interesting to repeat this experiment at -20°C , where hysteresis is present in PLZT, and observe if the application of a strong DC field reduces the hysteresis, therefore confirming a phase change from a relaxor to a ferroelectric phase under the application of the DC field.

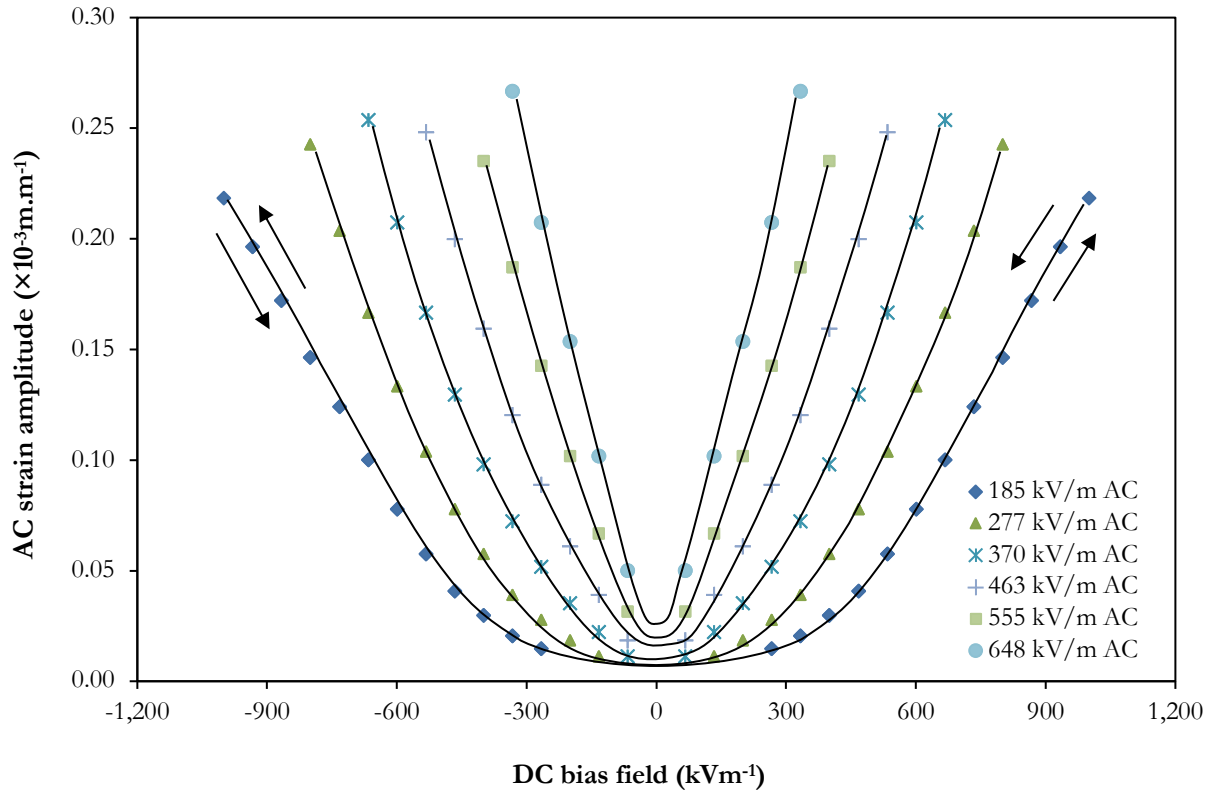


Figure 5.7. The AC strain amplitude of PLZT 9.0 at 150 Hz at the first harmonic frequency as a function of the DC bias electric field at various AC fields. The DC field cycled from 0 kVm^{-1} to 1000 kVm^{-1} , down to 0 kVm^{-1} , then -1000 kVm^{-1} , and then back up to 0 kVm^{-1} .

5.3.2 BM-941

The mechanical resonance peaks of the BM-941 sample and structure were obtained in order to determine what frequencies should be avoided when measuring strain. The displacement magnitude was measured from 100 Hz to 500 Hz with a constant AC field of 500 kVm^{-1} at the first harmonic frequency, which was predominant in BM-941, and the results are shown in Figure 5.8. The sample analyzed was a disk with a radius $r = (10.46 \pm 0.01) \text{ mm}$, a thickness $t = (2.58 \pm 0.01) \text{ mm}$, and a density $d = (5710 \pm 10) \text{ kg/m}^3$. As seen in Figure 5.8, the structure had resonance peaks at 140 Hz, 205 Hz, 280 Hz, and 420 Hz.

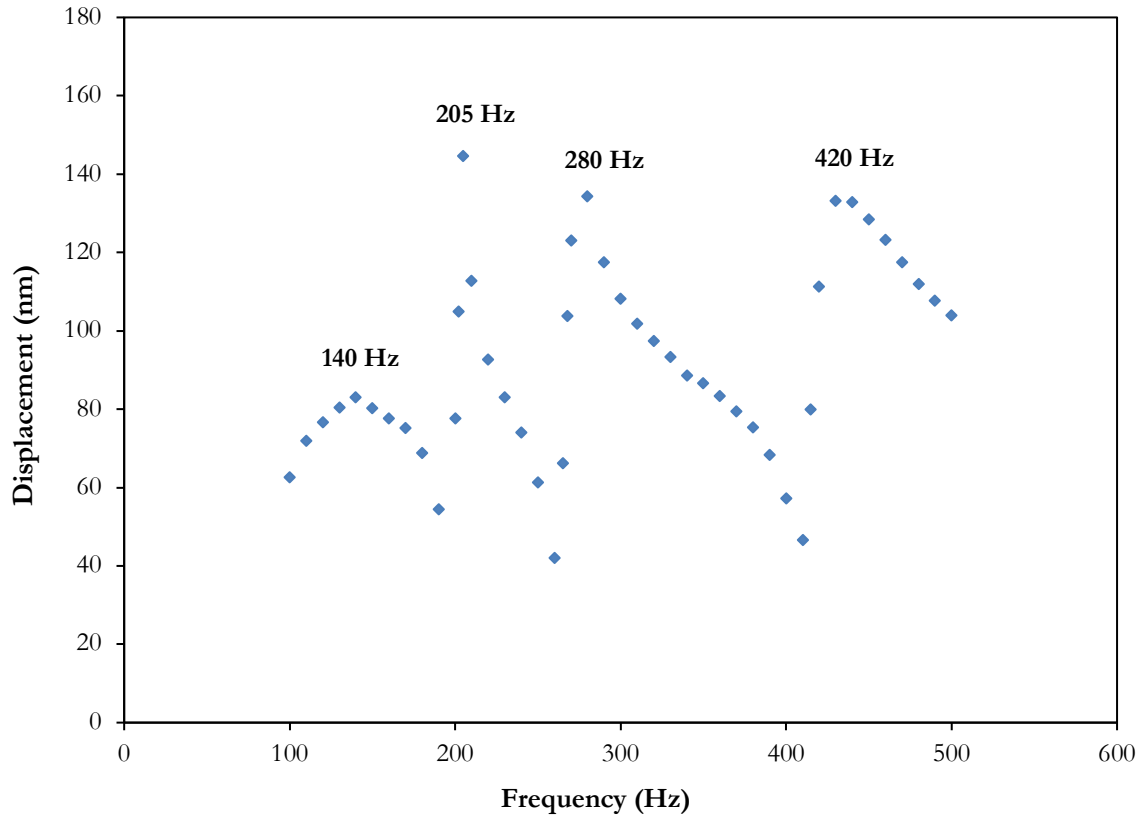


Figure 5.8. Mechanical resonance peaks for the first harmonic of the BM-941 sample and structure at $500 \text{ kV}_{\text{AC}}\text{m}^{-1}$ and $0 \text{ kV}_{\text{DC}}\text{m}^{-1}$.

Next, the AC strain amplitude of BM-941 was obtained as a function of the AC electric field amplitude, with no DC bias at 110 Hz, 250 Hz, 350 Hz, and 450 Hz at the first harmonic frequency. The response at the second harmonic frequency was negligible, which means that BM-941 is not electrostrictive. AC fields of less than $200 \text{ kV}\text{m}^{-1}$ did not produce significant strain, and AC fields over $1000 \text{ kV}\text{m}^{-1}$ short-circuited the sample. The highest AC strain amplitude reached in BM-941 was $0.13 \times 10^{-3} \text{ m}\cdot\text{m}^{-1}$, which is significantly lower than maximum AC strain amplitude reached in PLZT 9.0. It is believed that higher strain amplitudes could be reached if the sample were protected against short-circuiting. Using equation 5.4 and the average slope of the AC strain amplitude in Figure 5.9, the d_{33} for BM-

941 was found to be $(0.97 \pm 0.03) \times 10^{-10} \text{m.V}^{-1}$. The value reported by the manufacturer, Sensor Technology Limited, is $1.65 \times 10^{-10} \text{m.V}^{-1}$ [93]. Sensor Technology Limited used a Berlincourt d_{33} meter to obtain d_{33} , and the frequency of measurements explains the difference between the two values.

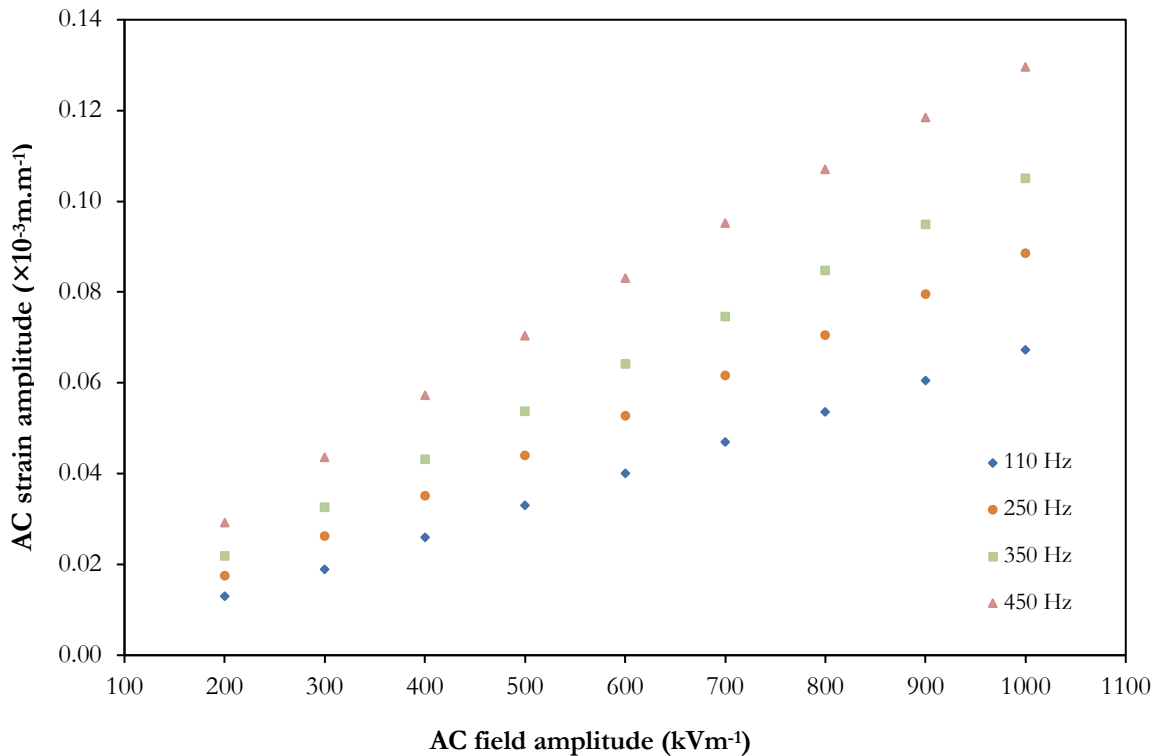


Figure 5.9. The AC strain amplitude of BM-941 as a function of the AC electric field amplitude, with no DC bias for different frequencies at the first harmonic frequency.

Next, the effects of DC bias electric fields on BM-941 were investigated. The AC strain amplitude of the first harmonic frequency was plotted for various frequencies as a function of the DC bias electric field at $700 \text{ kV}_{AC} \text{m}^{-1}$ from $-620 \text{ kV}_{DC} \text{m}^{-1}$ to $+620 \text{ kV}_{DC} \text{m}^{-1}$. Figure 5.10 clearly shows that DC bias electric fields have no effects on the AC strain amplitude of BM-941 at room temperature. It would be interesting to be able to find a way to design this experiment at 130°C and 280°C where phase changes are believed to occur in

BM-941, and hence confirm that DC bias electric fields can indeed induce phase changes in piezoelectric materials.

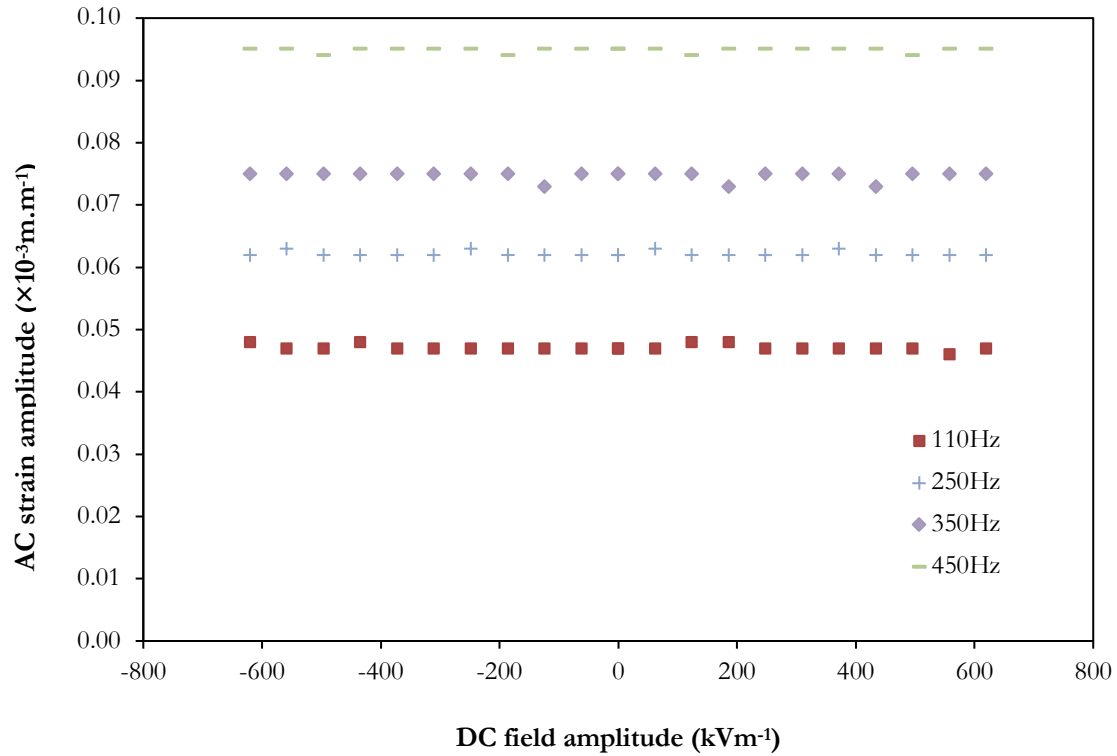


Figure 5.10. The AC strain amplitude of BM-941 at the first harmonic frequency for various frequencies as a function of the DC bias electric field at $700 \text{ kV}_{\text{AC}} \text{m}^{-1}$.

CHAPTER 6 : CONCLUSION

6.1 Conclusion

The goal of this thesis was to improve the understanding of piezoelectric materials in order to facilitate the development of new materials and help optimize current piezoelectric applications. Due to the wide range of applications of piezoelectric materials, they are used over a broad range of frequencies, temperatures, pressures and voltages. Such diverse environmental conditions result in a non-linear piezoelectric response, and the presence of impurities, dopants, and defects add to the complexity of predicting how a material performs once it is manufactured. The theory behind piezoelectricity is complex, and this thesis aimed to reduce the gap between the theory and experimental observations.

At first, the structural properties of piezoelectric materials were explored. SEM pictures of EC-65, EC-69, and EC-76 revealed the effect of grain size and material density on the piezoelectric response. Domains and their effect on the intrinsic and extrinsic piezoelectric effect was explained. Doping was also studied for soft and hard PZT, and it was found to lower permittivity in hard PZT and increase the piezoelectric coefficients in soft PZT, supporting the results from Chapter 3 and Chapter 4. The phase diagrams of PZT and PLZT were re-visited, and it was suggested that they both be re-written in terms of point groups, as opposed to crystal systems, since point groups and symmetry, not crystal systems, dictate the piezoelectric response. Finally, the X-ray diffraction spectrum of PLZT 9.5 was obtained, and it was found that both the cubic and the tetragonal phase were present at room temperature, which explains the high ferroelectric and piezoelectric response

present in PLZT. The Rietveld X-ray analysis is recommended for further research, since it gives not only the crystal system, but also the symmetry point group of the material. The phase diagram of BM-941 could further be built using the Rietveld analysis, and it would complement the results obtained in Chapter 3, 4, and 5 of this thesis.

Next, the ferroelectric properties of EC-65, PLZT 9.5, BM-941, BM-600, BM-150, and PMN-PT were studied. Polarization curves were obtained for all these materials for electric fields ranging from 0 to $\pm 2 \text{ MVm}^{-1}$ and temperatures ranging from -40°C to 120°C . Single crystal PMN-PT and relaxor ferroelectric PLZT 9.5 were found to have the highest polarization response with maximum electric displacements of 0.30 C/m^2 and 0.33 C/m^2 respectively. The maximum electric displacement observed in lead-free BM-150 was 0.11 C/m^2 , which is relatively high for a lead-free ceramic. The polarization curves of EC-65, BM-941, and BM-150 were slightly asymmetric, which suggests the presence of impurities in the samples or preferential domain wall motion. The polarization curve obtained for BM-600 is typical of electrostrictive materials, which supports the manufacturer's claim that the material is electrostrictive. The temperature dependence of polarization and hysteresis in PLZT 9.5 revealed a phase change from a relaxor to a ferroelectric phase between 10°C and 20°C , which agrees with the results obtained in Chapter 4 and 5. Finally, the polarization curves obtained for BM-941 did not reveal any phase change between 30°C and 90°C , which makes it a good candidate for applications operating in this temperature range.

Next, the dielectric properties of piezoelectric materials were studied. Impedance was used to determine the relative permittivity and the dielectric loss tangent of EC-69, PLZT 9.0, PLZT 9.5, and BM-941 as a function of temperature for different frequencies. The

relative permittivity and dielectric loss tangent of EC-69 were obtained from -40°C to 140°C , and it was determined that no phase change occurred in this temperature range since no broad peaks were observed in the relative permittivity nor in the dielectric loss tangent. It was also discovered that this material experienced higher losses at temperatures below -20°C and above 120°C , which limits its operational range. Hysteresis was observed in the dielectric curves for EC-69, which agrees with the polarization curves obtained for EC-69 in Chapter 3. Next, the relative permittivity and dielectric loss tangent of PLZT 9.0 and 9.5 were obtained from -40°C to 140°C , and it was determined that a phase change from a relaxor ferroelectric phase to a paraelectric phase occurred in both PLZT 9.0 and PLZT 9.5 around 80°C . Evidence for another phase change around 10°C was also discovered. The frequency dependent relaxor-like behavior of PLZT 9.0 and PLZT 9.5 was also observed. Next, the relative permittivity and dielectric loss tangent of BM-941 were obtained from -150°C to 200°C . Evidence of a phase change around 10°C was discovered, and relaxor-like behavior was confirmed in BM-941. Minor evidence of a phase change was also observed around 130°C , but X-ray diffraction and the Rietveld analysis should be performed on BM-941 to confirm this second phase change. BM-941 was also found to have an unusually low quality factor, which makes it a good candidate for applications requiring low frequency dependency, such as broadband transducers and immersed non-destructive evaluation.

Finally, the electromechanical properties of piezoelectric and electrostrictive materials were studied. The AC strain amplitude of BM-941 and PLZT 9.0 were presented as a function of the AC electric field for different frequencies, with and without a DC bias, at room temperature. The first harmonic was found to be negligible in PLZT 9.0 when no DC bias was introduced, which supports the results from Chapter 3 where PLZT 9.5 was found

to have minimal hysteresis at room temperature. Without a DC bias, the strain amplitude of PLZT 9.0 predominantly comes from the second harmonic, confirming the electrostrictive nature of PLZT 9.0. With a DC bias, the first harmonic piezoelectric strain is dominant. Relaxor-like behavior was confirmed, and further evidence of a phase transition from the relaxor to the ferroelectric phase around room temperature was obtained. In BM-941, the first harmonic was found to be predominant when no DC bias was introduced, which means that the strain response from BM-941 is piezoelectric and not electrostrictive. Finally, it was discovered that DC bias had no effects on the AC strain amplitude of BM-941 at room temperature, but it was suggested that this experiment be repeated at 130°C and 280°C where phase changes are believed to occur in BM-941.

Overall, the measurements obtained build upon the current knowledge of piezoelectric materials, support results obtained by other researchers, and also present new results that can be used to develop new materials and optimize current applications.

RERERENCES

- [1] D. Harper, "Piezoelectric," [Online]. Available: <http://www.etymonline.com/index.php?term=piezoelectric>. [Accessed 12 December 2011].
- [2] W. Haywang, K. Lubitz and W. Wersing, *Piezoelectricity: Evolution and future of a technology*, New York: Springer, 2008.
- [3] A. Mandelis, "Perspective: Photopyroelectric effects and pyroelectric measurements," *Review of Scientific Instruments*, vol. 82, no. 12, 2011.
- [4] W. Commons, "Natural Piezoelectric Materials," [Online]. Available: http://commons.wikimedia.org/wiki/Main_Page. [Accessed 20 01 2012].
- [5] S. B. Lang, "Pyroelectricity: A 2300-year history," *Ferroelectrics*, vol. 7, no. 1, pp. 231-234, 1974.
- [6] J. Curie and P. Curie, "Développement par pression de l'électricité polaire dans les cristaux hémihédres à faces inclinées," *Compte Rendu des Annales de la chimie*, no. 91, pp. 294-295, 1880.
- [7] G. Lippmann, "Principe de la conservation de l'électricité, ou second principe de la conservation de l'électricité," *Annales de chimie et de physique*, vol. 24, p. 145, 1881.
- [8] W. Voigt, *Lehrbuch der Kristallphysik*, Leipzig: Teubner, 1910.
- [9] P. Langevin, "Procédés et appareils d'émission et de réception des ondes élastiques sous-marines à l'aide des propriétés piézoélectriques du quartz". Paris Patent 505703, 17 Septembre 1918.
- [10] A. Manbachi and R. Cobbold, "Development and application of piezoelectric materials for ultrasound generation and detection," *Ultrasound*, no. November, pp. 1-10, 2011.
- [11] W. Mason, "Piezoelectricity, its history and applications," *Journal of the Acoustical Society of America*, no. 70, pp. 1561-1566, 1981.
- [12] L. Cross and R. Newnham, "High-Technology Ceramics- Past, Present, and Future. History of Ferroelectrics," *Ceramics and Civilization*, vol. 3, pp. 289-305, 1987.
- [13] "History of Piezoelectricity," Piezo Systems Inc., [Online]. Available: <http://piezo.com/tech4history.html>. [Accessed 13 December 2011].
- [14] D. Berlincourt, "Piezoelectric ceramics: Characteristics and applications," *Journal of the Acoustical Society of America*, vol. 70, no. 6, pp. 1586-1595, 1981.
- [15] G. Shirane, E. Sawaguchi and Y. Takagi, "Dielectric Properties of Lead Zirconate," *Phys. Rev.*, vol. 84, no. 3, pp. 476-481, 1951.

- [16] B. Jaffe, R. Roth and S. Marzullo, "Piezoelectric Properties of Lead Zirconate-Lead Titanate Solid-Solution Ceramics," *Journal of Applied Physics*, vol. 25, pp. 809-810, 1954.
- [17] B. Jaffe, R. Roth and S. Marzullo, "Properties of Piezoelectric Ceramics in the Solid Solution Series Lead-Titanate Lead-Zirconate Lead-Oxide Tin-Oxide Lead-Titanate and Lead-Hafnate," *J. Res. Natl. Bur. Stand.*, vol. 55, pp. 239-243, 1955.
- [18] R. Cobbold, *Foundations of biomedical ultrasound*, Toronto: Oxford University Press, 2007.
- [19] G. Smolensky and A. Agranovskaja, *Sov. Phys. Tech.*, vol. 3, p. 1380, 1958.
- [20] L. E. Cross, "Relaxor Ferroelectrics," *Springer Series in Materials Science*, vol. 114, no. 1, pp. 131-155, 2008.
- [21] APC International Ltd., "Piezoelectric Constants," [Online]. Available: <http://www.americanpiezo.com/knowledge-center/piezo-theory/piezoelectric-constants.html>. [Accessed 06 January 2012].
- [22] J. Kuwata, K. Uchino and S. Nomura, *Ferroelectrics*, vol. 37, p. 579, 1981.
- [23] J. Kuwata, K. Uchino and S. Nomura, *Japan Journal of Applied Physics*, vol. 21, p. 1298, 1982.
- [24] A. Singh and B. Kumar, "Development of piezoelectric and relaxor ceramics for sensor materials," in *First Asian Himalayas International Conference, 3-5 Nov 2009*, <http://ieeexplore.ieee.org/stamp/stamp.jsp?tp=&arnumber=5340271&isnumber=5340254>, 2009.
- [25] E. Fukada, "Recent Developments of Polar Piezoelectric Polymers," *IEEE Transactions on Dielectrics and Electrical Insulation*, vol. 13, no. 5, pp. 1110-1119, October 2006.
- [26] E. Fukada, "History and Recent Progress in Piezoelectric Polymers," *IEEE transactions on ultrasonics, ferroelectrics, and frequency control*, vol. 47, no. 6, pp. 1277-1290, Nov 2000.
- [27] Society of Plastics Engineers, "Polyvinylidene Fluoride (PVDF)," 2011. [Online]. Available: <http://www.4spe.org/plastics-encyclopedia/polyvinylidene-fluoride-pvdf>. [Accessed 08 02 2012].
- [28] SI Images Inc, "Manufacturing Piezoelectric Materials," Staten Island, New York, 2007. [Online]. Available: <http://www.imagesco.com/articles/piezo/piezo03.html>. [Accessed 27 January 2012].
- [29] K. Omote, H. Ohigashi and K. Koga, "Temperature dependence of elastic, dielectric, and piezoelectric properties of "single crystalline" films of vinylidene fluoride trifluoroethylene copolymer," *Journal of Applied Physics*, vol. 86, no. 6, pp. 2760-2769, 1997.
- [30] YTC America Inc, "Lead-free Piezoelectric Ceramics," [Online]. Available:

http://www.ytca.com/lead_free_piezoelectric_ceramics.

- [31] E. Parliament, "Directive 2002/95/EC of the European Parliament on the restriction of the use of certain hazardous substances in electrical and electronic equipment," *Official Journal of the European Union*, vol. 37, pp. 19-23, 2003.
- [32] P. Goodman, "Review of Directive 2002/95/EC (RoHS) Categories 8 and 9 - Final Report," ERA Technology, Brussels, 2006.
- [33] R. López-Juárez, F. González and M.-E. Villafuerte-Castrejón, "Lead-Free Ferroelectric Ceramics with Perovskite Structure," in *Ferroelectrics – Material Aspects*, InTech, August 2001, pp. 305-330.
- [34] T. Takenaka, H. Nagata and Y. Hiruma, "Current Developments and Prospective of Lead-free Piezoelectric Ceramics," *Jpn. J. Appl. Phys.*, vol. 47, pp. 3787-3801, 2008.
- [35] E. Parliament, "Directive 2011/65/EU of the European Parliament on the restriction of the use of certain hazardous substances in electrical and electronic equipment," *Official Journal of the European Union*, vol. 174, pp. 88-110, 2011.
- [36] I. Turner, "Piezoelectric Materials and Applications," 2010. [Online]. Available: <http://www.whystudymaterials.ac.uk/casestudies/piezo.asp>. [Accessed 15 January 2012].
- [37] The American Ceramics Society, "Ceramics in Sports," 2012. [Online]. Available: <http://ceramics.org/learn-about-ceramics/ceramics-in-sports>. [Accessed 01 Feb 2012].
- [38] K. M. Jeric, An experimental evaluation of the application of smart damping materials for reducing structural noise and vibrations, Master of Science: Mechanical Engineering, 1999.
- [39] S. Li, S.-J. Sun, D.-C. Liu, S.-P. Lin, D.-P. Juang, C.-H. Wang and G.-S. Ger, "Vibration suppressed bicycle structure". United States Patent 10/962,485, 17 Jan 2006.
- [40] N. Hagood and J. Horodezky, "Method and Apparatus for Active Control of Golf Club Impact". United States Patent US 2010/0292024 A1, 27 Jul 2011.
- [41] W. Mason, "First and second order equations for piezoelectric crystals expressed in tensor form," *Bell Sys. Tech. Journal*, no. 26, 1947.
- [42] The American Society of Mineralogists, "MSA Crystal Structure Database," 2001. [Online]. Available: <http://www.minsocam.org/>. [Accessed 14 February 2012].
- [43] M. Ugorek, "Patterned solid state growth of barium titanate crystals," in *Doctoral Thesis / Dissertation*, The Pennsylvania State University - Greater Allegheny, 2009, p. 154.
- [44] W. Cady, "Piezoelectricity", New York: McGraw-Hill, 1946.

- [45] W. Lee, "BaTiO₃ Temperature-stable dielectric capacitor," Department of Engineering Materials, University of Sheffield, 02 Sept 2002. [Online]. Available: Department of Engineering Materials, University of Sheffield.
- [46] S. Li, W. Cao and L. Cross, "The extrinsic nature of nonlinear behavior observed in lead zirconate titanate ferroelectric ceramic," *J. Appl. Phys.*, vol. 69, pp. 7219-7224, 1991.
- [47] T. Masys, "Non-linear Properties of Piezoelectric Materials," in *M.Sc. Thesis*, Royal Military College of Canada, 2001.
- [48] S. Trolier-McKinstry, N. B. Gharb and D. Damjanovic, "Piezoelectric nonlinearity due to motion of 180° domain walls in ferroelectric materials at subcoercive fields: A dynamic poling model," *Applied Physics Letters: DIELECTRICS AND FERROELECTRICITY*, vol. 88, no. 20, 2006.
- [49] H. Guo, A. A. Bokov and Z.-G. Ye, "Piezoelectric response around ferroelectric domain walls in crystals with engineered domain configuration," *Haiyan Guo, Alexei A. Bokov, and Zuo-Guang Ye*, vol. 81, no. 024114, pp. 1-5, 2010.
- [50] J. E. Garcia, J. D. S. Guerra, E. B. Araujo and R. Perez, "Domain wall contribution to dielectric and piezoelectric responses in 0.65Pb(Mg_{1/3}Nb_{2/3})–0.35PbTiO₃ ferroelectric ceramics," *J. Phys. D: Appl. Phys.*, vol. 42, 2009.
- [51] A. Safari, R. Panda and V. Janas, "Ferroelectric Ceramics: Processing, properties and Applications," Department of Ceramics Science and Engineering, Rutgers University, Piscataway, NJ, USA.
- [52] T. Weston, A. Webster and V. McNamara, *Journal of American Ceramics Society*, vol. 52, p. 253, 1969.
- [53] Y. Xu, "Ferroelectric materials and their applications," Amsterdam, North-Holland, 1991, pp. 134-140.
- [54] EDO Ceramics, "EDO Ceramics EC-69 Lead Zirconium Titanate Piezoelectric," 2003. [Online]. Available: <http://www.matweb.com/search/datasheet.aspx?matguid=9da231ebc59346e7a404adf64b3883a0>. [Accessed 18 03 2012].
- [55] B. Jaffe, W. Cook and H. Jaffe, *Piezoelectric Ceramics*, London and New York: Academic Press, 1971.
- [56] "Stability of ferroic phases in the highly piezoelectric Pb(Zr_xTi_{1-x})O₃ ceramics," *Foundations of Crystallagraphy*, vol. 64, pp. 192-203, January 2008.
- [57] B. Noheda, D. E. Cox, G. Shirane, J. A. Gonzalo, L. E. Cross and S.-E. Park, *Appl. Phys. Lett.*, no. 74, pp. 2059-2061, 1999.

- [58] B. Noheda, J. A. Gonzalo, L. E. Cross, R. Guo, S.-E. Park, D. E. Cox and G. Shirane, *Phys. Rev. B.*, no. 61, pp. 8687-8695, 2000.
- [59] B. Noheda, D. E. Cox, G. Shirane, R. Guo, B. Jones and L. E. Cross, *Phys. Rev. B.*, no. 63, p. 014103, 2000.
- [60] D. M. Hatch, H. T. Stokes, R. Ranjan, M. S. K. Ragini, D. Pandey and B. J. Kennedy, *Phys. Rev. B.*, no. 65, p. 212101, 2002.
- [61] R. Ranjan, A. K. Singh, Ragini and D. Pandey, *Phys. Rev. B.*, no. 71, p. 092101, 2005.
- [62] A. K. Singh and D. Pandey, *Phys. Rev. B.*, no. 67, p. 064102, 2003.
- [63] J. M. Kiat, Y. Uesu, B. Dkhil, M. Matsuda, C. Malibert and G. Calvarin, *Phys. Rev. B.*, no. 65, p. 064106, 2002.
- [64] H. Fu and R. E. Cohen, *Nature (London)*, no. 403, pp. 281-283, 2000.
- [65] G. Haertling, "PLZT Electro-optics Materials and Applications - A Review," *Ferroelectrics*, vol. 75, pp. 25-55, 1987.
- [66] Serrano, "CSIS Crystallography," 2012. [Online]. Available: http://www.xtal.iqfr.csic.es/Cristalografia/archivos_04/espaciado-en.jpg. [Accessed 26 January 2012].
- [67] W. Känzig, "Ferroelectrics and Antiferroelectrics," in *Solid State Physics*, Academic Press, 1957, p. 5.
- [68] D. Damjanovic, "Hysteresis in Piezoelectric," in *The Science of Hysteresis*, Lausanne, Switzerland, Swiss Federal Institute of Technology, 2006, pp. 337-287.
- [69] C. Sawyer and C. Tower, "Rochelle Salt as a Dielectric," *Physical Review*, vol. 35, p. 269, 1930.
- [70] V. Bobnar, Z. Kutnjak, R. Pirc and A. Levstik, "Electric Field Temperature Phase Diagram of the Relaxor Ferroelectric Lanthanum-modified Lead Zirconate Titanate," *Physics Review*, vol. 60, pp. 6420-6427, 1999.
- [71] M. Cerqueira, R. Nasar, E. Leite, E. Longo and J. Varela, "Synthesis and characterization of PLZT (9/65/35) by the Pechini method and partial oxalate," *Materials Letter*, no. 35, pp. 166-171, 1997.
- [72] V. Bobnar, Z. Kutnjak, R. Pirc and A. Levstik, "Electric-field–temperature phase diagram of the relaxor ferroelectric lanthanum-modified lead zirconate titanate," *Physical Review B*, vol. 9, no. 60, pp. 6420-6427, 1999.

- [73] S. Trivijitkasem and K. Koyvanich, "Characterization of Lead Lanthanum Zirconate Titanate (PLZT) Ceramics Sintered at Various Temperatures," *Journal of Natural Sciences*, no. 41, pp. 192-197, 2007.
- [74] M. Bernier-Brideau, "Characterization of ferroelectric ceramics," Undergraduate Thesis, Royal Military College of Canada, Kingston, 2009.
- [75] Y. Mnyukh, "Hysteresis and nucleation in condensed matter," in *Fundamentals of Solid-State Phase Transitions 2nd Ed.*, Farmington, USA, DirectScientific Press, 2010.
- [76] Technologies Agilent, "Agilent Impedance Measurement Handbook, 4th Edition," 2009.
- [77] I. Rosu, "Impedance Matching," Bucharest University, [Online]. Available: http://www.qsl.net/va3iul/Impedance_Matching/Impedance_Matching.pdf. [Accessed 03 May 2012].
- [78] Hyperphysics, "Impedance," 2010. [Online]. Available: <http://hyperphysics.phy-astr.gsu.edu/hbase/electric/imped.html>. [Accessed May 04 2012].
- [79] "All About Circuits," 2012. [Online]. Available: http://www.allaboutcircuits.com/vol_2/chpt_4/2.html. [Accessed 04 May 2012].
- [80] D. Viehland, F. Tito, E. McLaughlin, H. Robinson, R. Janus, L. Ewart and J. Powers, "Enhancement of electromechanical coupling coefficient and acoustic power density in conventional "Hard" $\text{Pb}(\text{Zr}_{1-x}\text{Ti}_x)\text{O}_3$ ceramics by application of uniaxial stress," *Journal of Applied Physics*, vol. 90, no. 3, p. 1496–1500, 2001.
- [81] B. Jaffe, W. Cook and H. Jaffe, *Piezoelectric Ceramics*, London and New York: Academic Press, 1971.
- [82] R. Sabat, W. Ren, G. Yang and B. Mukherjee, "Temperature dependence of the complete material coefficients matrix of soft and hard doped PZT ceramics," *Journal of Applied Physics*, vol. 101, no. 4, 2007.
- [83] G. Haertling, "Improved Hot-Pressed Electrooptic Ceramics in the $(\text{Pb},\text{La})(\text{Zr},\text{Ti})\text{O}_3$ System," *Journal of the American Ceramic Society*, vol. 54, pp. 303-309, 1971.
- [84] R. Sabat, P. Rochon and B. Mukherjee, "Quasistatic Dielectric and Strain Characterization of Transparent Relaxor Ferroelectric Lead Lanthanum Zirconate Titanate (PLZT) Ceramics," *Journal of Applied Physics*, vol. 104, no. 5, 2008.
- [85] S. T. Limited, *SensorTech Product Catalogue*, Collingwood, ON, 2009.
- [86] S. Nemana, M. Bernier-Brideau and R. Sabat, *Improved Coupling Coefficients in Lead Metaniobate Ceramics*, Sensor Technology Limited, 2012.

- [87] W. Wersing, W. Heywang, H. Beige and H. Thomann, "The Role of Ferroelectricity for Piezoelectric Materials," in *Piezoelectricity - Evolution and Future of a Technology*, Berlin, Heidelberg, Springer Series in Materials Science, 2008, pp. 37-88.
- [88] D. Damjanovic, "Ferroelectric, dielectric and piezoelectric properties of ferroelectric thin films and ceramics," *Rep. Prog. Phys.*, vol. 61, p. 1267–1324, 1998.
- [89] Polytec, Polytec Vibsoft Manual, Hauptsitz, Germany: <http://www.polytec.com>, 2008.
- [90] Polytech, Polytec Hardware Manual, Hauptsitz, Germany: <http://www.polytec.com>, 2008.
- [91] V. Bobnar, Z. Kutnjak, R. pirc and A. Levstik, "Electric-Field-temperature phase diagram of the relaxor ferroelectric lanthanum-modified lead zirconate titanate," *Phys. Rev. B*, vol. 60, pp. 6420-27, 1999.
- [92] A. J. Masys, W. Ren, G. Yang and B. K. Mukerherjee, "Piezoelectric strain in lead zirconate titanate ceramics as a function of electric field, frequency, and dc bias," *Journal of Applied Physics*, vol. 94, pp. 1155-1162, 2003.
- [93] Sensor Technology Limited, "BM941 - Lead Metaniobate," 2011. [Online]. Available: [http://www.sensortech.ca/userfiles/file/BM941\(1\).pdf](http://www.sensortech.ca/userfiles/file/BM941(1).pdf). [Accessed 01 March 2014].
- [94] U. o. Exeter, "Crystal Symmetry," [Online]. Available: <http://newton.ex.ac.uk/research/qsystems/people/goss/symmetry/Solids.html>. [Accessed 26 January 2012].
- [95] T. A. Galleries, "Crystal systems," [Online]. Available: <http://www.galleries.com/minerals/symmetry/symmetry.htm>. [Accessed 25 January 2012].
- [96] Serrano, "CSIS Crystallography," 2012. [Online]. Available: <http://www.xtal.iqfr.csic.es/Cristalografia/index-en.html>. [Accessed 26 January 2012].

CURRICULUM VITAE

CURRICULUM VITAE

Maxime Bernier-Brideau

Contact Information :

950 Notre-Dame West, Montreal, QC, H3C 0K3
maxime.bernier.brideau@gmail.com

Post Secondary Education

- 2010-2014 Masters of Science in Physics, Royal Military College of Canada, Kingston, ON
- 2007-2010 Bachelors of Science Honours in Space Sciences and Physics, Royal Military College of Canada, Kingston, ON
- 2005-2007 Diplôme d'études collégiales in Pure and Applied Sciences, CEGEP Champlain St-Lawrence, Québec, QC

Military Experience

- 2007 Basic Military Officer Qualification Phase I, Saint-Jean-sur-Richelieu, QC
- 2008 Basic Military Officer Qualification Phase II, Saint-Jean-sur-Richelieu, QC
- 2007-2010 Royal Military College of Canada, Kingston, ON
- 2010 Primary Flight Training, Portage-la-Prairie, MB
- 2012-2013 Basic Flight Training, Moose Jaw, SK

Other

- 2009 International Space University, NASA AMES Center, Mountain View, CA, United States of America
- 2011 International Space University, Graz Technical University, Graz, Austria
- 2014 International Space University, École de Technologie Supérieure and École des Hautes Études Commerciales, Montréal, Canada